# Master Thesis

## Experimental and Numerical Investigation of Blade-Tip Rotors on Vertical-Axis Wind Turbines

Ferran van Kan

| | |
|---|---|
| Supervisor | Dr. Carlos Simao Ferreira |
| Department | Aerodynamic and Wind Energy, Aerodynamics |
| Date of Delivery | February 20, 2023 |

Delft University of Technology

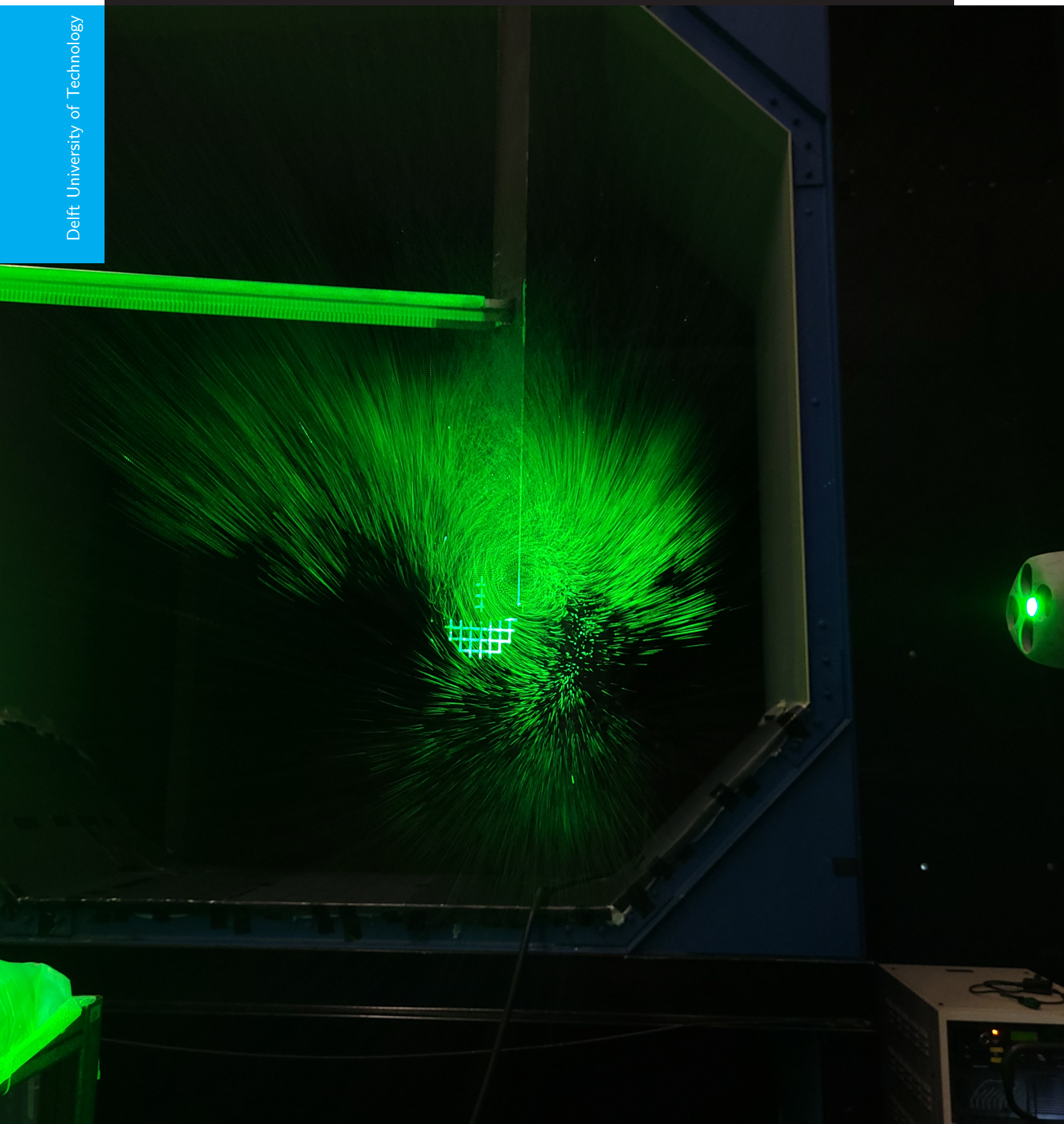

# ABSTRACT

A study is conducted on the effects of tip-mounted rotors on a conventional Darrieus H-VAWT; this study is complementary to the X-rotor concept proposal. This proposal features a novel offshore wind turbine concept that utilises blade-mounted tip rotors to extract energy from the flow. Following a literature study phase, an experimental campaign is devised that utilises various porous actuator mesh disks as an approximation of blade tip-mounted HAWT geometries. Additionally, the implementation of a blade element vortex model is also investigated.

Experimentation using an existing VAWT is conducted at the Open Jet Facility at TU Delft. The test is conducted at a freestream velocity of $V_\infty$ = 4.0 m/s at an average Reynolds number of Re=$7.5 \cdot 10^4$. Key outputs from the test are the normal forces on the primary (VAWT) rotor blades, the torque measured at the shaft of the primary rotor and the thrust force of the primary rotor. Through post-processing, it is also possible to determine the thrust of the tip-mounted actuator mesh disk and verify the outcome with empirical models. Moreover, large-scale volumetric flow field measurements are also conducted using a PTV system which comprises a coaxial volumetric velocimetry probe mounted to a robotic arm. The PTV system uses Helium Filled Soap Bubbles as tracers to measure the flow field.

Key results from the mesh disk study are consistent with initial assumptions; the thrust of the actuator disk is inversely proportional to the porosity. However, there are discrepancies observed between the different means of measuring the actuator disk thrust, this suggests that experimental inaccuracies are present. Effects of the actuator mesh disk on the blade performance showed a reduction of blade normal forces, an increase of the primary rotor thrust force as well as changes to the turbine thrust vector direction.

The measurements conducted using PTV highlight changes to the blade wakefield which has consequences for the BVI. Notable differences between the cases with and without actuator disks include the lack of the upwind shed vortex in the investigated region when the actuator mesh disk is present. In the case without the actuator mesh disk, the interaction with the downwind and upwind shed vortices is destructive, thus the vorticity in the wake dissipates more rapidly. Tests with the actuator mesh disk conducted at TSR=4.0 showed that the wake of the actuator disk is able to persist longer and thus interact with the second blade leading to BVI. The lack of the upwind shed vortex destructing the downwind vortex likely means that the wake dissipates more slowly. Moreover, the presence of reverse flow behind the actuator disk is identified as another contributor to the large velocity deficit observed in the wake.

The numerical vortex model that is proposed is an extension of the pre-existing CACTUS vortex model developed by Sandia National Laboratories. The changes to the CACTUS numerical model enable the implementation of tip rotor geometries to VAWTs. Initial testing shows behaviour that is within expectations, however, the results are limited by a coarse spatial grid; this highlights the necessity for optimisation of the numerical model in the future. The numerical vortex model demonstrates that it is possible to use this model for the investigation and optimisation of blade tip-mounted rotors.

# PREFACE

> "Do not be sidetracked. A good referee will have many ways to distract an expedition, many things to draw attention, but ignore them if at all possible." - Gary Gygax, Player's Handbook [1]

The words of Gygax are clearer to me now that I have well and truly learned this lesson. After a long and arduous journey, I too get the chance to finish my Master's studies. A project that was overwhelming at times yet the results of which leave me with a sense of pride and accomplishment. It was an honour to work on this collaborative project with Carlos Simao Ferreira, David Bensason and Adhyanth Giri Ajay. Without their input, the fruits of my labour would not be as fruitful as they are now.

I am grateful to have been allowed to work on such a novel concept in a specific field of aerodynamics that is very pertinent in today's climate. To conduct a large-scale wind tunnel test with so many facets was a bountiful experience from which I have learned a great deal. I would like to also extend thanks to both Andrea Sciacchitano and Constantin Jux for their aid and patience with the wind tunnel experiments.

To my family, I am thankful that they gave me the support to conduct my work when the going got tough and we were all stuck at home. To my girlfriend, Paula, I owe a great deal for all the encouragement and support during the most challenging times. A final thanks are extended to my friends with who I have forged incredible bonds during my studies. From the long days working in the Fellowship to staying up all night before project deadlines, together we have pushed each other, enriched our experiences and developed a great deal as people.

Ferran van Kan
Pijnacker, November 2022

# CONTENTS

# List of Figures

# LIST OF TABLES

# NOMENCLATURE

## List of Abbreviations

| | |
|---|---|
| BVI | Blade Vortex Interaction |
| CACTUS | Code for Axial and Cross-flow TUrbine Simulation |
| CFD | Computational Fluid Dynamics |
| CVV | Coaxial Volumetric Velocimetry |
| DHPC | Delft High-Performance Computing Centre |
| FOV | Field of View |
| FSU | Fluid Supply Unit |
| GF | Gauge Factor |
| HAWT | Horizontal-Axis Wind Turbine |
| HSFB | Helium Soap Filled Bubble |
| LPT | Lagrangian Particle Tracking |
| OJF | Open Jet Facility |
| OTF | Optical Transfer Function |
| PIV | Particle Imaging Velocimetry |
| PSD | Power Spectral Density |
| PTV | Particle Tracking Velocimetry |
| RPM | Revolutions Per Minute |
| SNL | Sandia National Laboratories |
| STB | Shake-The-Box |
| TSR | Tip-Speed Ratio |
| VAWT | Vertical-Axis Wind Turbine |

## List of Symbols

| | | |
|---|---|---|
| $\alpha$ | Angle of attack | [°] |
| $\alpha_b$ | Geometrical angle of attack | [°] |
| $\alpha_m$ | Modified angle of attack | [°] |
| $\bar{c}$ | Blade chord | [m] |
| $\beta$ | Blade pitch angle | [°] |
| $\beta$ | Porosity | [−] |
| $\epsilon$ | Convergence criteria | [−] |
| $\epsilon$ | Strain | [−] |
| $\Gamma$ | Circulation | [$m^2/s$] |
| $\Gamma_B$ | Circulation bound vortex | [$m^2/s$] |
| $\lambda$ | Tip-speed ratio | [−] |
| $\omega$ | Normalised vorticity | [−] |
| $\omega$ | Rotational velocity | [rad/s] |
| $\omega_x$ | Normalised vorticity about x | [−] |
| $\omega_{yz}$ | Normalised vorticity in yz plane | [−] |
| $\phi_T$ | Thrust direction | [°] |
| $\psi$ | Inflow angle | [°] |
| $\rho$ | Density | [$kg/m^3$] |
| $\rho_{strut}$ | Strut density | [$kg/m^3$] |
| $\sigma$ | Rotor solidity | [−] |
| $\sigma$ | Stress | [$N/m^2$] |
| $\theta$ | Azimuth angle | [°] |
| $a$ | Axial induction factor | [−] |
| $A_T$ | Rotor reference area | [$m^2$] |
| $A_{strut}$ | Strut cross sectional area | [$m^2$] |
| $B$ | Number of rotor blades | [−] |
| $C_{D,5}$ | Drag coefficient half chord | [−] |
| $C_D$ | Drag coefficient | [−] |
| $C_{L,5}$ | Lift coefficient half chord | [−] |
| $C_L$ | Lift coefficient | [−] |
| $C_N$ | Normal force coefficient | [−] |
| $C_P$ | Power coefficient | [−] |
| $C_Q$ | Torque coefficient | [−] |
| $C_{T,\alpha}$ | Thrust coefficient due to blade pitch | [−] |
| $C_{T_{tip}}$ | Tip rotor thrust coefficient | [−] |
| $C_T$ | Thrust coefficient | [−] |
| $C_X$ | X force coefficient | [−] |
| $C_Y$ | Y force coefficient | [−] |
| $D$ | Rotor diameter | [m] |
| $d$ | Load cell distance | [m] |
| $d_i$ | Disparity | [m] |
| $E$ | Elastic modulus | [$kg/m^3$] |

| | | |
|---|---|---|
| $E_{strut}$ | Strut elastic modulus | [kg/m$^3$] |
| $F_N$ | Force normal component | [N] |
| $F_T$ | Force tangential component | [N] |
| $F_x$ | Force x component | [N] |
| $F_y$ | Force y component | [N] |
| $F_{ax}$ | Axial force | [N] |
| $H$ | Turbine height | [m] |
| $k$ | Reduced frequency | [−] |
| $L$ | Length | [m] |
| $N$ | Number of samples | [−] |
| $N_{elem}$ | Number of blade elements | [−] |
| $N_{ti}$ | Number time steps | [−] |
| $Q$ | Torque | [Nm] |
| $Q_{AD}$ | Actuator disk induced torque | [Nm] |
| $Q_{clean}$ | Clean rotor torque | [Nm] |
| $R$ | Rotor radius | [m] |
| $Re$ | Reynolds number | [−] |
| $s$ | Spanwise direction | [m] |
| $S_{elem}$ | Blade element area | [m$^2$] |
| $T$ | Thrust | [N] |
| $t$ | Time | [s] |
| $V_\infty$ | Freestream velocity | [m/s] |
| $V_{eff}$ | Effective velocity | [m/s] |
| $V_{ex}$ | Excitation voltage | [V] |
| $V_{ind,N}$ | Induced velocity normal component | [m/s] |
| $V_{ind,T}$ | Induced velocity tangential component | [m/s] |
| $V_{ind}$ | Induced velocity | [m/s] |
| $V_{noise}$ | Noise voltage | [V] |
| $V_N$ | Normal velocity component | [m/s] |
| $V_{out}$ | Output voltage | [V] |
| $V_{rel}$ | Relative velocity | [m/s] |
| $V_{rot}$ | Rotational velocity component | [m/s] |
| $V_r$ | Strain voltage | [V] |
| $V_T$ | Tangential velocity component | [m/s] |
| $V_w$ | Wake velocity | [m/s] |

# 1

# INTRODUCTION

The modern state of the energy industry has been in the transition from being fossil fuel dependent to relying on sustainable (and or renewable) resources; this process has been accelerated in the face of an energy crisis. It is becoming increasingly imperative that society avoids large-scale damage, both on climate as well as social and economical values. It is within the previously established context that one must consider innovations in the energy industry to help future energy and resource infrastructures.

One such innovation exists in offshore wind energy where the increased potency of the wind resource at sea is an attractive prospect for energy production (Esteban et al. [12]). Additionally, offshore wind energy installations are less limited by social-political and environmental restrictions because they can be installed away from populated areas. At present, the majority of offshore wind turbines are installed in exclusive economic zones that extend 200 nmi from the coast and depths up to 40 m (Dupont et al. [13]). Modern platform technology limits the depth at which offshore wind turbines can be effectively constructed. However, floating semi-submersible platforms allow for greater energy yield due to their ability to claim wind energy further from shore.

The X-rotor concept is a collaborative proposal to the European Union to investigate the advantages of a novel vertical-axis wind turbine (VAWT) that utilises secondary horizontal-axis wind turbines (HAWT) mounted at the tips of the lower blades; an illustration of the X-rotor is shown in Figure 1.1. These tip-mounted rotors (HAWTs) extract power from the flow field which is augmented by the rotation of the primary rotor (VAWT). In this situation, the secondary rotor effectively functions as an airbrake, with its drag force (or thrust) in combination with the rotational speed producing work and thus energy. The advantage of extracting power from the secondary rotors is due to lower maintenance costs being associated with the smaller tip generators since their torque is lower when compared to large VAWT turbine generators (Jamieson and Leithead et al [2, 14]). Additionally, lighter generators are preferential when considering offshore floating platform stability.

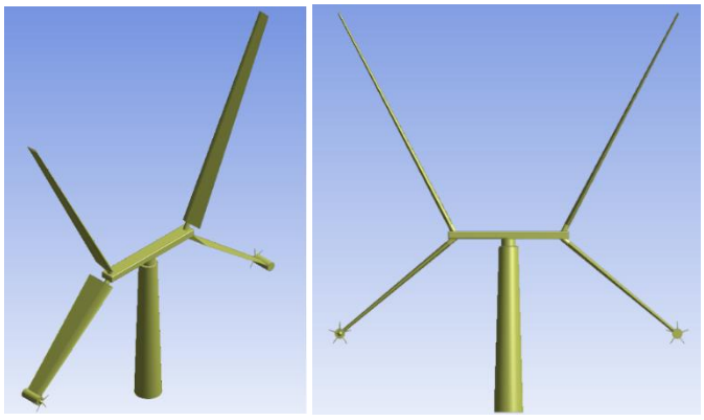

Figure 1.1: A graphical representation of the X-rotor VAWT with tip-rotors [2]

There is sufficient justification to warrant researching the potential of the X-rotor concept, particularly the effects of secondary tip rotors on VAWTs. This is the subject matter of this body of work where the secondary tip rotor concept will be investigated experimentally and numerically. The key objectives for the experimental work are aimed at quantifying the effects of secondary tip rotors on the performance of the primary rotor by measuring the thrust and blade loading. Additionally, the thrust performance of the secondary tip rotors

will be investigated using actuator disks to replicate the implementation of tip rotors.

Further investigations of the wake produced from a secondary tip rotor utilise the novel measurement technique of particle tracking velocimetry to yield volumetric data of the flow field. This data will be used to investigate the effect of the secondary tip rotor on the blade tip vortex in addition to the consequences of the blade vortex interactions.

In addition to the experimental simulation, a numerical vortex model will be proposed to estimate the effects of secondary tip rotors. This model will be based on CACTUS (Code for Axial and Cross-flow TUrbine Simulation) developed at Sandia National Laboratories (SNL) at the Department of Energy. The low-fidelity vortex model is a fast model capable of yielding vast amounts of aerodynamic data based on relatively simple geometries. The numerical model will be compared to the results of the experimental campaign to validate the results and demonstrate the capabilities of the algorithm.

This report will first present the state-of-art which underlines the founding theory upon which this thesis is based. Following this the experimental campaign will be discussed, this includes detailed explanations of the experimental setup and data post-processing. The experimental chapter is closed with a presentation of the results which includes the verification and validation of the data. The numerical simulation chapter is structured similarly where the foundation of the model and numerical parameters/geometries are introduced. Validation of the numerical model based on the experimental model will also be presented before the findings made using the tip rotors are discussed. Finally, the report will conclude all the results and provide suggestions for subsequent research topics.

# 2

# STATE-OF-ART

This chapter presents the state-of-art as it pertains to the subject matter of the thesis. Section 2.1 discusses the fundamental aerodynamics that governs the physics of Vertical-Axis Wind Turbines (VAWTs). Lastly, Section 2.2 and Section 2.3 will outline some experimental and numerical models that can be used to estimate the performance of VAWTs.

## 2.1. FUNDAMENTALS OF VAWT AERODYNAMICS

A number of the founding principles that govern the aerodynamics of VAWTs will be outlined in this section. A key aspect of VAWT aerodynamics that will be covered is the inherent flow unsteadiness and the implications this has for the aerodynamics and performance of VAWTs.

To begin, an overview of the flow velocities, angles and aerodynamic forces are presented for a lift-driven VAWT. The example shown in Figure 2.1 is that of a straight-bladed Darrieus-type VAWT [15]; this figure illustrates the mathematical expressions that are used to define the VAWT aerodynamics. The rotor area itself is defined by its radius (constant in the case of a straight-bladed VAWT), $R$, the blade chord length, $\bar{c}$ and the total number of blades, $B$. In three dimensions, the blade length is finite, thus the height of the turbine is also noted, $H$. The local flow velocity vector, $V_{rel}$ is defined by the free stream velocity $V_\infty$ and the rotational velocity component, $V_{rot}$. The latter is a result of the rotational velocity of the rotor, $\omega$, and the rotor radius. The velocity component induced onto the flow by the forces generated by the rotor blades is denoted by $V_{ind}$.

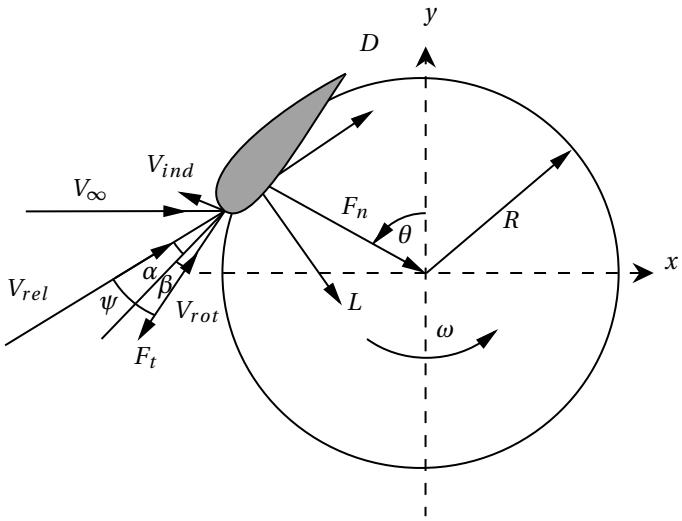


Figure 2.1: VAWT blade flow velocities, local flow and geometric angles and aerodynamic forces

Furthermore, $\theta$ defines the azimuth angle of the blade; this allows one to distinguish two regions within the rotor area namely the upwind half of the rotor between 0° and 180° with the downwind part encompassing the region between 180° and 360°. To that end, the azimuth angle describes the angle between the airfoil and the free stream flow direction. The angle of attack, $\alpha$, describes the angle between the airfoil centre line and the relative flow velocity vector. The blade pitch angle, $\beta$, describes the geometrical angle between the rotating path tangent line and the chord centre line. Lastly, the inflow angle $\psi$ becomes the angle between

the rotating path tangent line and the relative flow velocity vector (this is equivalent to the angle of attack for zero blade pitch).

As mentioned previously, the relative velocity is the summation of the free stream, rotational- and induced velocity components, this can be seen in Equation (2.1). This velocity dictates the local flow properties on the rotor blade.

$$\overrightarrow{V_{rel}} = \overrightarrow{V_{\infty}} + \overrightarrow{V_{rot}} + \overrightarrow{V_{ind}} \tag{2.1}$$

In a rotating reference frame, it is often convenient to decompose the velocity components into normal- and tangential components based on the rotational path of the blades. In this reference frame, the tangential velocity, $V_T$ is defined as positive in the counter-clockwise direction and $V_N$ is positive inwards. Using the rotating reference frame, the following expressions can be produced:

$$\begin{aligned} V_N &= V_{\infty} \cdot sin(\theta) + V_{ind,N} \\ V_T &= \omega R + V_{\infty} \cdot cos(\theta) + V_{ind,T} \end{aligned} \tag{2.2}$$

The flow characteristics of a VAWT are inherently unsteady, a large contribution to the unsteadiness is the variation in the local flow velocity. Islam et al [16] shows that the relative flow velocity varies with the azimuth angle, this results in the following expressions for the normal- and tangential velocity components:

$$\begin{aligned} V_{rel} &= \sqrt{V_N^2 + V_T^2} \\ V_{rel} &= \sqrt{\left(V_{\infty} \cdot sin(\theta) + V_{ind,N}\right)^2 + \left(\omega R + V_{\infty} \cdot cos(\theta) + V_{ind,T}\right)^2} \end{aligned} \tag{2.3}$$

Another useful expression is the tip-speed ratio (or TSR), this parameter is defined by the ratio between the freestream velocity and the rotational velocity at the blade. It is defined in Equation (2.4).

$$\lambda = \frac{\omega R}{V_{\infty}} \tag{2.4}$$

Due to the variations in the local flow vector, the local angle of attack also varies azimuthally. The angle of attack can be expressed in components of the normal- and tangential velocity components, this is expressed mathematically in Equation (2.5). The variable angle of attack in combination with variations in the relative velocity yields dynamic blade loading distribution.

$$\alpha = \arctan\left(\frac{V_N}{V_T}\right) - \beta \tag{2.5}$$

The variations in the blade aerodynamic forces are a result of variations in the local flow field conditions. Equation (2.6) and Equation (2.7) provide expressions for the aerodynamic forces of lift and drag, in addition to how they relate to the rotational coordinate system

$$\begin{aligned} L &= \frac{1}{2}\rho V_{rel}^2 C_L(\alpha) A_T \\ D &= \frac{1}{2}\rho V_{rel}^2 C_D(\alpha) A_T \end{aligned} \tag{2.6}$$

$$\begin{aligned} F_N &= L \cdot cos(\psi) + D \cdot sin(\psi) \\ F_T &= L \cdot sin(\psi) - D \cdot cos(\psi) \end{aligned} \tag{2.7}$$

When discussing a VAWT's performance, several parameters are investigated. These parameters are normalised w.r.t the flow conditions and the turbine geometry. First, the torque produced by the turbine as

a result of the tangential forces on the blades can be ascertained by determining the revolution-averaged tangential force.

$$\overline{F_{t,2D}} = \frac{1}{2\pi}\int_0^{2\pi} F_{t,2D}(\theta)d\theta \tag{2.8}$$

The total torque at the rotor ($Q$) is subsequently obtained using the following expression where $B$ is the number of blades.

$$\begin{aligned} Q &= B \cdot R \cdot \overline{F_T} \\ Q &= B \cdot R \cdot \frac{1}{2\pi}\int_0^{2\pi} F_T(\theta)d\theta \end{aligned} \tag{2.9}$$

Moreover, the power produced by the turbine is equivalent to the work conducted by the rotor blades multiplied by the rotational speed of the blades. Similarly, one can take the torque and multiply it by the rotational speed, which yields Equation (2.10) which describes the turbine power.

$$P = \frac{1}{2\pi}\int_0^{2\pi} B \cdot F_T(\theta) \cdot \omega \cdot R \cdot d\theta \tag{2.10}$$

Likewise, the thrust can also be obtained by integrating the normal and -tangential force distributions over one rotor revolution, this is evident in Equation (2.11).

$$T = B \cdot \frac{1}{2\pi}\int_0^{2\pi} \left(F_T(\theta) \cdot cos(\theta) - F_N(\theta) \cdot sin(\theta)\right) d\theta \tag{2.11}$$

In terms of normalisation, the torque, power and thrust coefficients are provided below. They are each normalised by the dynamic pressure $\frac{1}{2}\rho V_\infty^2$ in addition to some geometrical parameters. The geometrical parameters include $A_T$ which is the turbine area defined by the turbine height multiplied by the diameter and $R$ which is the radius of the rotor.

$$C_Q = \frac{Q}{\frac{1}{2}\rho V_\infty^2 A_T R} \tag{2.12}$$

$$C_P = \frac{P}{\frac{1}{2}\rho V_\infty^3 A_T} \tag{2.13}$$

$$C_T = \frac{T}{\frac{1}{2}\rho V_\infty^2 A_T} \tag{2.14}$$

### 2.1.1. Unsteady Aerodynamics

The variations in local flow velocity and inflow angle yield a varying force field due to changes in the bound vorticity of the rotor blade. The unsteadiness of the aerodynamics can be quantified using the reduced frequency ($k = \omega\bar{c}/2V_{rel}$), hereby unsteady conditions are observed when $k > 0.05$ [17]. Two fundamental unsteady phenomena will be outlined here.

#### Dynamic Stall

The process of dynamic stall is the result of a time-dependent change in the inflow angle that can exceed the stall angle of attack of the airfoil during a revolution. This subsequently leads to flow reversal in the boundary layer followed by flow separation at the leading edge. The leading edge separation yields a 'spilt'

vortex that convects downstream inducing lift and moving the centre of pressure aft. Once the leading edge vortex reaches the trailing edge of the airfoil, the flow becomes fully separated. Finally, when the angle of attack is reduced sufficiently as the blade rotates, the flow will reattach to the surface and the process repeats for the subsequent blade rotations. This unsteady process is prevalent for low tip-speed ratios ($\lambda < 4$). The effect of dynamic stall reduces the loads on the blades and thus reduces the performance of the turbine. [18]

### Blade Vortex Interaction

Another effect of the cyclic motion of the blades is the blade vortex interaction (BVI). This non-linear behaviour is the result of shed vorticity produced in the upwind direction being convected downstream where it impinges upon the blade(s) in the downwind part of the rotor. These interactions cause pressure fluctuations over the blades yielding changes to the lift and the drag [19]. Moreover, from a fluid-structure perspective, BVI can cause vibrations due to unsteady loads which reduces the fatigue life of the rotor [20].

The phenomena of BVI impairs rotor performance by reducing the blade loading and power production performance. Although BVI is not as severe as dynamic stall due to BVI typically only affecting 6.4% of the azimuthal range compared to the 22% affected by the dynamic stall. The previous statement is the result of predictions made by Bangga et al. [21] who conducted a numerical study of dynamic stall and BVI on a single-bladed VAWT through the use of CFD and XFOIL boundary layer codes.

Ferrer and Willden [20] also researched the BVI for VAWTs. The authors developed analytical tools for estimating the effects of the BVI on the blade forces which was subsequently validated using a Discontinuous Galerkin solver with sliding meshes. The analytical model is capable of estimating the interaction of the shed vortex using the convection of the vortex (axial induction, $a$) and the rotation of the blade (tip-speed ratio, $\lambda$). This model was applied for a single bladed-VAWT and a triple-bladed VAWT; the increase in the number of blades yielded increased BVI.

## 2.2. Experimental Models

The concept for the present work uses the work conducted by LeBlanc and Ferreira [6, 8–11] and the pitch-VAWT experimental model. Much work on the model has been dedicated to determining blade loading and turbine thrust vectors depending on blade pitch.

Blade loading can be determined by mounting strain gauges on the blade struts, this technique was utilised by LeBlanc and Ferreira [10]. The strain gauges are capable of measuring the axial deformation in the struts which is a result of the normal forces produced by the turbine blades. However, this does not provide a full description of the blade forces since the tangential loads are not measured. This has consequences for determining the thrust coefficient as a result of the blade forces. In their work, LeBlanc and Ferreira [10] found that for zero blade pitch angle, the omission of the tangential blade force leads to a $\approx 6\%$ overestimation of the thrust force magnitude and a $\approx 2.5^\circ$ difference (leeward) in the direction of the thrust vector.

Work from LeBlanc and Ferreira in [6] shows that it is possible to utilise a torque transducer to provide output for the torque applied by the turbine motor. Also, Bartl et al [22] and Howell et al [23] have demonstrated that it is possible the measure turbine torque at the rotor shaft, although employ different means to do so. An optical sensor at the shaft is used to calibrate the azimuth position of the turbine, then using a rotary encoder LeBlanc and Ferreira [6] to track the azimuth position of the rotor in time which allows assessing the acquired data in the context of the azimuth angle.

For measuring the forces acting on the turbine shaft, LeBlanc and Ferreira [8] use four load cells mounted at the turbine base. These load cells allow for determining the Cartesian forces $F_x$ and $F_y$ in addition to the (total) thrust vector.

### Flow Visualisation

Flow visualisation is a crucial desire in the aerodynamic industry. For the aerodynamics analysis of the flow field on VAWTs, it has been standard to utilise planar- and stereoscopic particle image velocimetry to measure the flow field. These techniques have also been applied at the Delft University of Technology as evidenced by the works of Tescione et al. [3] and Ferreira [24]. The experiment conducted by Tescione et al. applies both a planar and stereoscopic PIV to measure the flow field produced by a VAWT, the setups for these experiments are shown in Figure 2.2.

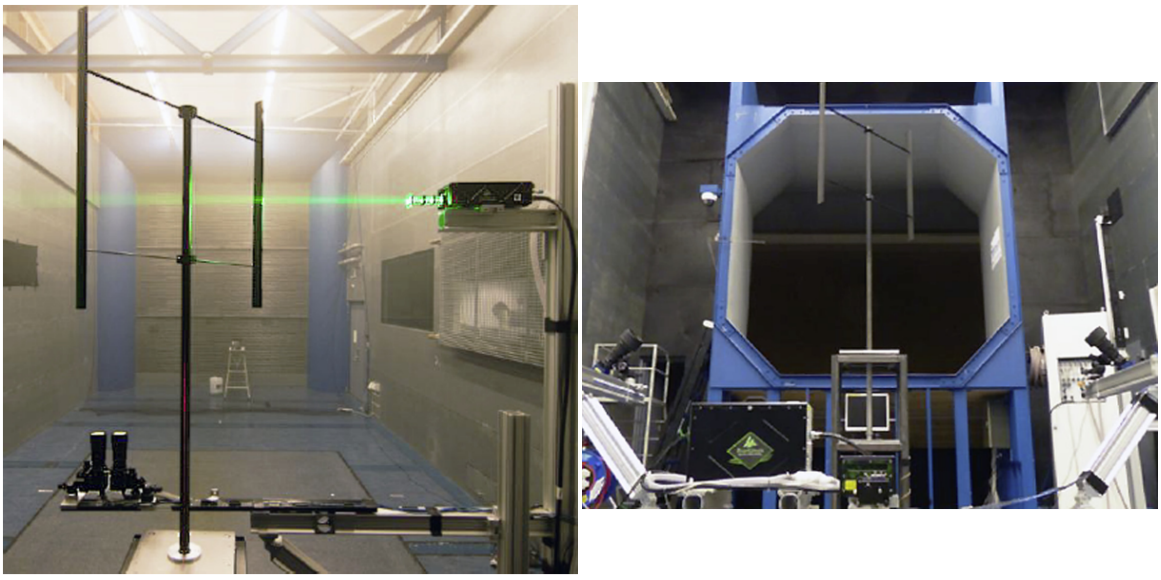

(a) Planar PIV setup

(b) Stereoscopic PIV setup

Figure 2.2: The setup of the PIV experiment from Tescione et al. [3]

The analysis of PIV data also requires some careful consideration regarding averaging the flow field data. A key interest for flow visualisation resides in the visualising of vortical structures shed either through tip

vortices or due to dynamic stall processes. Conventionally, when the flow field is steady it is acceptable to decompose instantaneous velocity fields into a time-averaged (mean) and fluctuating part. However, due to the unsteadiness of VAWT aerodynamics time averaging will remove key periodic elements of the aerodynamics. Therefore phase-lock averaging is applied as presented in the works of Wernert and Favier [25], here the authors provide a means to determine the sample size required to achieve phase-lock averaging with acceptable uncertainty. The number of samples required is determined by the convergence criteria.

$$1-\epsilon < \frac{\overline{V(t,N)_{est}}}{\overline{V(t,N_{max})_{est}}} < 1+\epsilon \tag{2.15}$$

In Equation (2.15), $V(t,N)_{est}$ is the estimated velocity in time based on the number of samples $N$ and $V(t,N_{max})_{est}$ is the estimated velocity based on the maximum number of samples $N_{max}$. If the number of samples, $N$, required to satisfy Equation (2.15) is much lower than $N_{max}$ then one can conclude that the total number of samples $N_{max}$ is sufficient. In PIV it has been shown that several hundred samples are required to determine the phase average value at a particular point, however, reasonable estimates for vortex strength can be achieved with a few dozen samples according to Ferreira [19]. This is also confirmed by Tescione et al. [3] who indicated that the convergence of the phase-locked average scales with $1/\sqrt{N}$ for which $N = 150$ is a sufficiently large sample size to ensure acceptable convergence. It is noted that there will be some highly local areas in the flow with high velocities (such as the blades) and large gradients (vortices) that do not converge since the timescales for these physics are too small, thus these areas can only be described qualitatively.

Other velocimetry techniques include volumetric particle tracking velocimetry as applied by Jux et al. in [26]. This is a relatively novel technique that combines volumetric velocimetry with robotic tracking which enables for repositioning of the camera system. This system can rapidly measure the flow field in a relatively large volume (several cubic metres) without being overly invasive on the local flow. The particle tracking is achieved using a helium bubble solution, the Lagrangian tracking algorithm known as Shake-the-Box is described by Schanz et al. [27] produces an ensemble average of the flow field that can be plotted in Cartesian coordinates to provide flow data on flow topologies such as vortices and stagnation points. An in-depth description of the particle tracking velocimetry (PTV) method is provided by Jux [28] in their thesis work.

## 2.3. Numerical Vortex Model

Numerical vortex models can be applied to a wide range of aerodynamic problems since they are based on the general potential flow theory. The method determines the induced velocity in the flow field or at the rotor through the influence of vorticity. The blades are defined by a spanwise distribution of vorticity that travels downstream originating from a bound vortex or lifting line. The magnitude of the vorticity is determined using airfoil data in addition to the flow velocity and angle of attack. The vortex model is solved temporally and thus is unsteady. The vortex models can be applied to 2D and 3D geometries. [29]

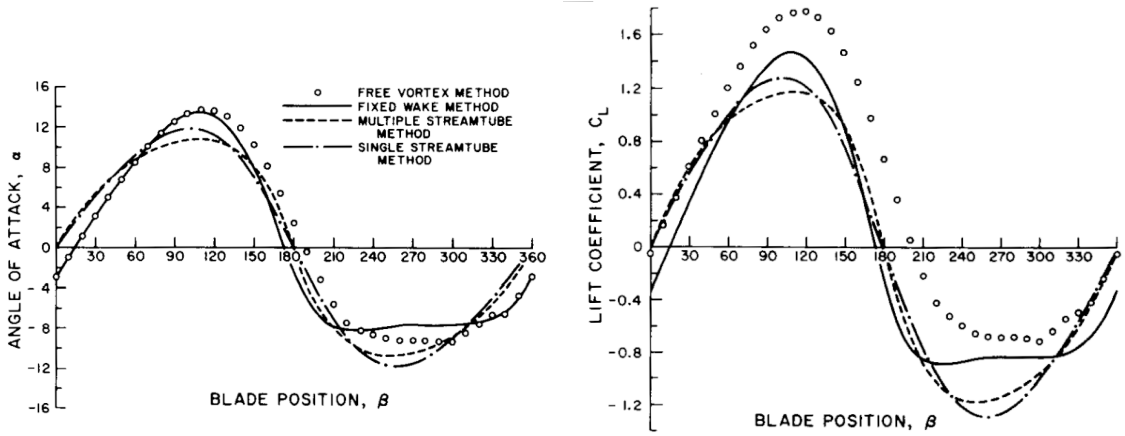


(a) Predicted angle of attack versus blade position by streamtube and vortex models

(b) Predicted lift coefficient versus blade position by streamtube and vortex models

Figure 2.3: Numerical results for streamtube and vortex models obtained from Wilson and McKie [4]

In their work, Wilson and McKie [4] present a 2D free wake vortex model which yields insight into the unsteady effects on rotor performance. As can be seen in Figure 2.3a, the vortex model better emulates the difference between the upwind and downwind parts of the rotor in terms of local angle of attack. This difference between upwind and downwind also infers changes to the lift coefficient at that blade position which is evident from Figure 2.3b. However, one of the shortcomings of the vortex model posed by Wilson [30] include: not capturing the effects of stall. Moreover, this early vortex method can only be used for straight-bladed rotors and the values for the performance and blade loading are approached asymptotically. The latter is the result of the model not fulfilling the conservation condition as stated by Kelvin's theorem. This means that there will always be an error in the system that reduces with the number of time steps; this yields slightly higher loads than if the wake were finite and circulation is conserved. Additionally, much of the precision of the vortex model is dependent on the accuracy of the airfoil polars available; this is particularly of an issue for low Reynolds number aerodynamics.

Further work by Strickland et al. [31] describes an extensive 3D vortex model that incorporates the aerodynamic stall. This model is subsequently reduced to a 2D model for straight-bladed rotors. Experiments were carried out to validate the 2D model using a simple H-rotor submerged in a water tank to visualise the flow structure. This experiment yielded good agreement between the experimental data and the analytical predictions, this includes the near-field wake structure and velocities in the wake.

As an amendment to the model from Strickland et al., Cardona [32] included the effects of flow curvature in addition to dynamic stall. This yielded a superior correlation than was previously achieved between experimentation and vortex models. Nevertheless, vorticity-based models are still inviscid.

### CACTUS Vortex Model

At present, the open-source CACTUS (Code for Axial and Cross-flow TUrbine Simulation) software, developed at Sandia National Laboratories, is a vorticity-based model that is specifically designed for the application of VAWTs and HAWTs. The authors Murray and Barone [33] describe the general capabilities of the software in their work. CACTUS simulates fluid motion and blade loading on individual blade elements of arbitrary geometry. The blade loading is obtained using empirical airfoil data which returns force coeffi-

cients as a function of the local angle of attack; the latter reaffirms the necessity for accurate airfoil data.

The CACTUS vortex model has the functionality of using either a fixed- or a free-wake vortex model. The free-wake vortex model accounts for the wake deformation, meaning the mutual induction of the shed vortices is determined which yields a variable local velocity throughout the wake. The fixed wake vortex model does not account for wake deformation and thus assumes a fixed wake convection velocity is used. This means that for the fixed method, only geometric constraints and the free stream velocity are parameters that affect the wake. The trade-off between these two methods is improved accuracy at the cost of computational effort, with the free wake model being the most demanding computationally (scaling with $N^2$) compared to the fixed method (scaling with $N$) whilst most closely representing the flow physics in the wake. [34]

The CACTUS model also has dynamic stall capabilities that are particularly relevant to VAWT simulation. The two dynamic stall models available are the Boeing-Vertol empirical [35] model and the Leishman-Beddoes Model [18, 36]. the Boeing-Vertol model is based on empirical observations of airfoil stall angles. This model aims to represent the hysteresis loop effects of oscillating airfoils on the force coefficients. Accounting for the hysteresis effect is accomplished by utilising a modified angle of attack $\alpha_m$ that lags behind the geometric angle of attack $\alpha_b$. Whilst also based on empirical data, the Leishman-Beddoes model uses a more physical approach in describing the dynamic stall effects meaning that it can be applied more generally. The model represents the unsteady aerodynamics by considering the three primary effects present during dynamic stall; these effects are leading edge separation, trailing edge separation and vortex lift. This yields a more complete description of the dynamic stall process in time, however, this model is computationally more expensive to execute.

# 3

# EXPERIMENTAL SIMULATION

In this chapter, the experimental campaign of the pitchVAWT with actuator mesh disks will be presented. This includes descriptions of the test conditions, experimental setup and an overview of all the tests to be conducted. Procedures for data post-processing are also explained before presenting the final results of the experimental campaign. Discussions of the results will also be provided.

## 3.1. TEST DESCRIPTION

This section provides a description of the pitchVAWT test, details will be provided regarding the experimental facilities and instrumentation utilised throughout the experimental campaign. Additionally, information on the VAWT model and actuator mesh disk model is also included.

### 3.1.1. WIND TUNNEL SETUP

The test facility used for experimentation with the PitchVAWT is the Open Jet Facility (OJF) at TU Delft, the Netherlands. This is a closed-loop wind tunnel with an open test section as shown in Figure 3.1. The outlet, octagonal in shape, measures 2.85 × 2.85 m and has a contraction ratio of 3:1; the outlet opens into a 13 m wide test section [5]. Within the wind tunnel test section flow velocities between 4 m/s to 35 m/s can be achieved. Characteristics of the flow in the tunnel are shear layers with a semi-angle of 4.7° and a turbulence intensity of 0.5% [37]. However, Jux [28] found that when the (HSFB) seeding rig is present inside the outlet of the wind tunnel, the turbulence intensity is increased to 2%.

Throughout all the experiments, testing is conducted at a constant wind speed of 4 m/s. Additionally, cooling meshes are present downstream of the test section which ensures that the air temperature is independent of the flow velocity. The experiments took place in November so temperatures within the tunnel were between 291 K and 293 K.

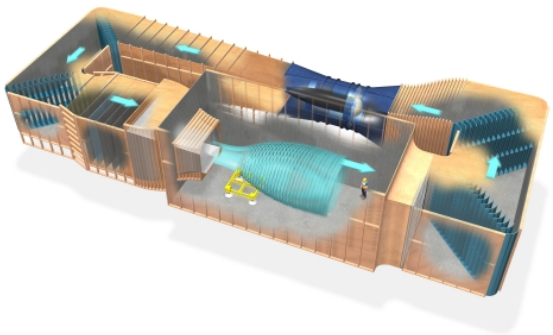

Figure 3.1: An illustration of the OJF, retrieved from [5]

### 3.1.2. VAWT SPECIFICATIONS

The VAWT utilised throughout this project is the PitchVAWT, the design of which is attributed to the work of LeBlanc and Ferreira [9] who developed it in 2018. The PitchVAWT is a twin-bladed Darrieus H-VAWT, the turbine is shown in Figure 3.2. The height and diameter of the PitchVAWT are both 1.5 m. The turbine blade geometry consists of a constant (spanwise) NACA0021 profile, each blade is supported by a pair of struts mounted at 25% and 75% of the blade. For the profiling of the rotor struts, the NACA0018 geometry is used. Both the blades and struts are manufactured from extruded aluminium. The struts attach to the central shaft which is connected by two thrust bearings to the base of the turbine where the torque sensor and the motor are located. The turbine motor is powered by a 24 V DC power supply which is sufficient to allow the turbine to rotate at a maximum speed of 255 RPM. More design specifications are listed in Table 3.1, additionally, a full description of the rotor design can be found in the work of LeBlanc and Ferreira [9].

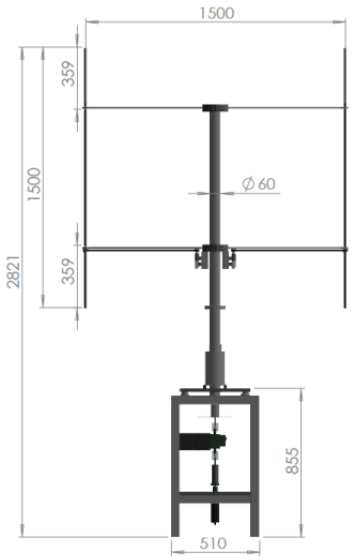


Figure 3.2: Schematic representation of the PitchVAWT, retrieved from LeBlanc and Ferreira [6]

Table 3.1: The design specification of the PitchVAWT, retrieved from [9]

| Parameter | Value |
|---|---|
| Number of blades | 2 |
| Number of struts | 4 |
| Height | 1.5 m |
| Diameter | 1.5 m |
| Blade chord | 0.075 m |
| Strut chord | 0.055 m |
| Solidity | 0.1 |
| Blade airfoil | NACA0021 |
| Strut airfoil | NACA0018 |

Table 3.2: PitchVAWT strut material properties, retrieved from [10]

| Parameter | Value |
|---|---|
| $\rho_{strut}$ | 2620 kg m$^{-3}$ |
| $E_{strut}$ | 55.0 GPa |
| $A_{strut}$ | 142.5 mm$^2$ |

### 3.1.3. VAWT Instrumentation

The PitchVAWT is equipped with several instruments which enable data logging of key parameters, such as rotational velocity, azimuth angle, torque and blade loading. The turbine features a rotary encoder mounted in the driveline between the main bearing and the motor; this device measures the rotational speed of the turbine and logs the azimuthal position of the rotor. The rotary encoder is capable of measuring the azimuth position to 0.25° and angular velocities as low as 2.5 RPM. Moreover, the rotary encoder is paired with a rotary torque transducer which measures the torque. [9]

The top struts of both blades are equipped with full-bridge strain gauges to measure the axial strain on the struts. This strain gauge layout accounts for axial stress induced by bending and temperature fluctuations. The gauge factors for blade 1 and blade 2 are 2.13 and 2.12 respectively, additionally, both have an excitation voltage of 3.3 V. The strain gauges are connected via a slip ring to the National Instruments$^{TM}$ Compact Rio hardware which allows for data acquisition, turbine control and data logging to LabVIEW. The turbine housing is mounted to the base via four load cells, these load cells in turn bear the full weight of the turbine and thus are capable of measuring the magnitude and direction of the thrust. The Piezoelectric load cells (PCB 208C02) are calibrated at a sensitivity of 10 mV/N. All data is acquired at a sample rate of 500 Hz. [8, 9]

As the name suggests, the PitchVAWT is capable of actively pitching the blades using onboard controllers. These controllers actuate pulleys mounted along the struts which in turn pitch the blades. However, for this project active blade pitch is not investigated thus the controllers are commanded to maintain a 0° pitch angle for all experiments. Further work regarding the active pitch system can be found in [9] and [10].

The experimental setup is shown in Figure 3.3 with annotations for all the components referenced in Table 3.3. Additionally, the measurement domain is highlighted and the right-handed global coordinate system is included with the x-axis defined in the flow direction.

### 3.1.4. Actuator mesh disk model

Modelling of the secondary (tip) rotors is achieved through the use of porous disks. The representation of horizontal-axis wind turbines by means of porous plates or meshes has been applied to the experimental simulation of HAWT wind farm configurations [38]. It has been observed that actuator mesh disks yield similar mean flow characteristics, particularly in the wake beyond 3 rotor diameters ($x/D > 3$). This also applies for low turbulence intensities of the order 4% with increased similarity observed with increasing turbulence levels, as concluded by Aubrun et al. [39]. However, certain instantaneous flowfield properties and vortical structures are not reproduced by actuator mesh disks [40]; these include rotor swirl and its interaction with the blade tip vortex.

Flow equivalency between actuator mesh disks and rotors is determined using the power/thrust coefficient through empirical relations obtained through testing. Empirical relations for equivalent actuator disks can be found in the work of Huang et al. [7] which identifies mesh porosity and shape as key drivers for the induced momentum deficit on the flow across the actuating surface.

The sizing of the actuator disks is based on data presented by Ming et al. [7]. In this paper, the authors present empirical data on the relation between actuator disk porosity ($\beta$) and the thrust coefficient ($C_T$). By applying linear regression to the data ($R^2$=0.87), an empirical function that satisfies Equation (3.1) is obtained which is used for sizing the actuator disks porosity. The variation in the empirical data is likely the result of key differences across the experiments from which the data is collected such as the shape of the porous mesh being either square or circular. Additionally, the bulk of the empirical data is collected in

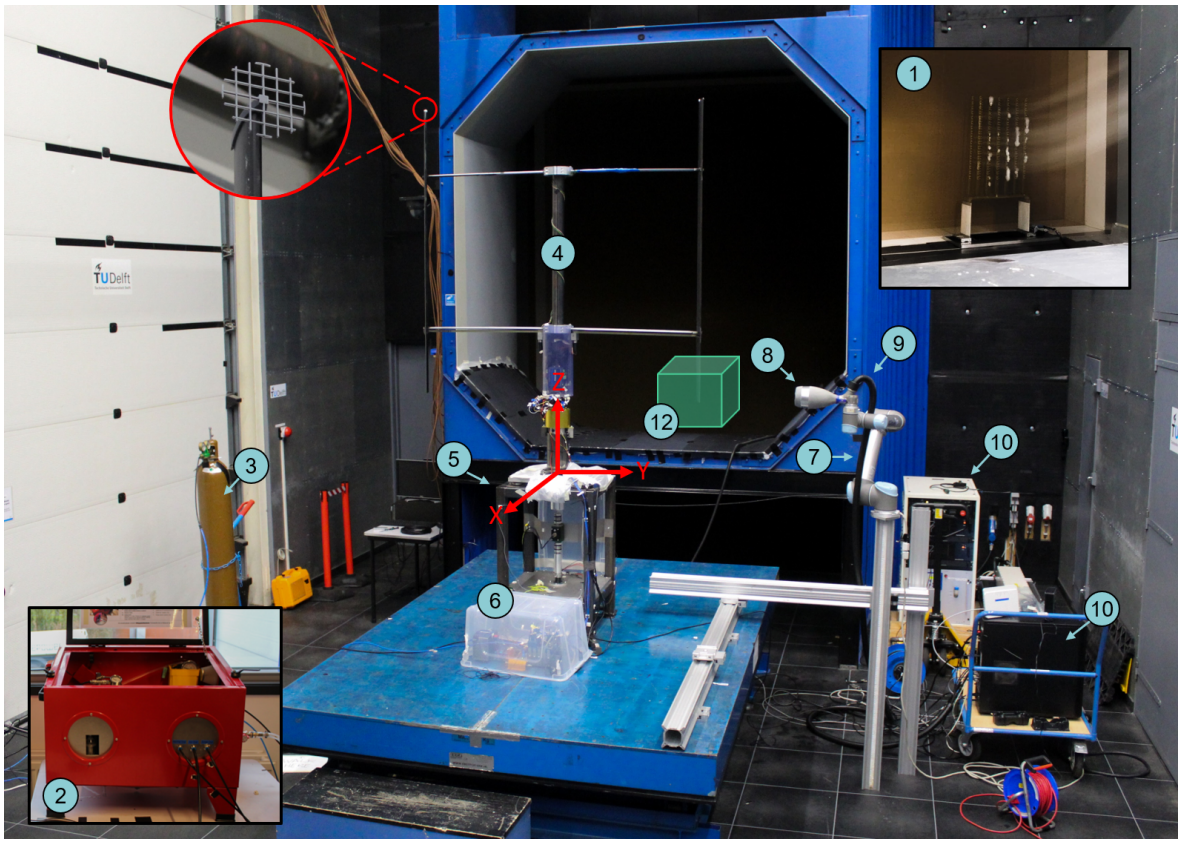


Figure 3.3: The VAWT experimental setup inside the OJF with PTV installation, indicated are various equipment and instrumentation

Table 3.3: Annotations for experimental test setup of the VAWT inside the OJF test section, see Figure 3.3

| Bullet | Description |
|---|---|
| 1 | The seeding rake |
| 2 | HSFB fluid supply unit |
| 3 | Helium supply tank |
| 4 | PitchVAWT |
| 5 | Turbine base |
| 6 | National Instruments$^{TM}$ Compact Rio hardware |
| 7 | UR5 robotic arm |
| 8 | LaVision MiniShaker coaxial velocimeter |
| 9 | Optical fibre |
| 10 | Quantronix Darwin Duo NdLYLF laser with lens array |
| 11 | PTV processing unit |
| 12 | Measurement volume (not to scale) |

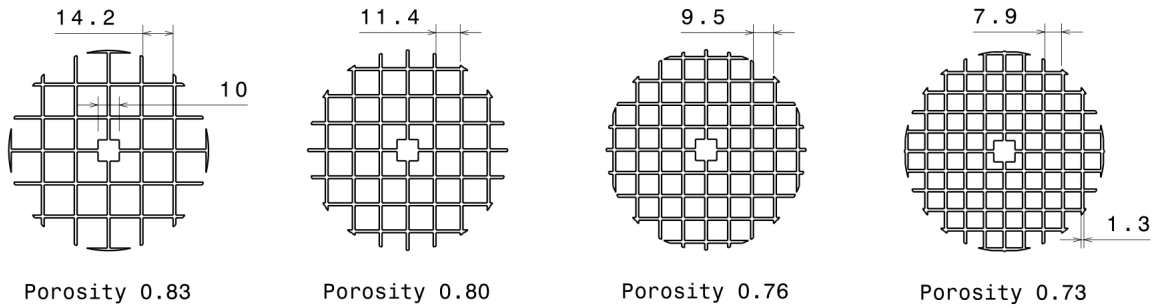


Figure 3.4: Schematics of the mesh disk models, all dimensions are in mm

the range $0.3 < \beta < 0.7$ with only a single data point for $\beta = 0.8$, thus, for the porosities tested in this campaign a higher degree of interpolation/extrapolation is necessary. Four sets of actuator disks selected of varying thrust coefficient and porosity based on the empirical data available at the time; they are tabulated in Table 3.4. Actuator disk theory is employed to determine the equivalent power coefficient of the actuator mesh disks. After the initial sizing of the actuator mesh disks, a separate wind tunnel experiment was conducted to verify the assumptions on porosity and thrust coefficient using the same mesh disks; the results of this test will be presented in Section 3.4.2.

$$C_T = -1.406 \cdot \beta + 1.421 \tag{3.1}$$

Table 3.4: Actuator mesh disk porosity, power- and thrust coefficient

| Porosity | $C_P$ | $C_T$ |
|---|---|---|
| 0.73 | 0.37 | 0.40 |
| 0.76 | 0.32 | 0.35 |
| 0.80 | 0.27 | 0.29 |
| 0.83 | 0.23 | 0.25 |

The diameter of the actuator disk is determined using data from the X-rotor concept. Hereby the diameter of the secondary rotor is ≈6% of the diameter of the primary rotor. This yields a diameter of 9.4 cm for the secondary rotor. These actuator disks are produced through 3D printing using polylactic acid (PLA), the mesh disk is attached to the PitchVAWT blades by means of a sleeve (also 3D printed) that is fastened onto the tip of the blade and is designed to be non-intrusive. The mesh disk attaches to the sleeve through a 10x10 $mm^2$ square section located at the centre of the mesh, the area of this square is accounted for when determining the mesh porosity. The dimensions for all the mesh disks are presented in Figure 3.4, the only dimension that varies between the disk is the size of the square voids. The depth of each mesh disk is kept constant at 2 mm. An example of the tip rotor installed on the blade can be seen in Figure 3.3.

#### W-TUNNEL TEST

Following the present experimental campaign, a separate yet-to-be-published experiment is conducted on the actuator disks by David Bensason. The aim of this experiment is to verify the assumption regarding the thrust coefficient using the empirical models. The experiment follows the procedures for determining the loads on the actuator disk described by Ming et al. [7] and applying it to the actuator disk model presented in this thesis. The results of the tests in the W-tunnel will be presented also in Section 3.4.2 when assessing the actuator disk thrust. A brief description of the test is given here.

The tests are conducted in the W-tunnel of the TU Delft Aerospace Engineering Laboratories. This tunnel is a low-speed open jet tunnel that features an outlet cross-section of $0.6 \times 0.6$ m, the measurements are

made at a freestream flow velocity of 4 m/s. The thrust of the actuator disk is measured using a load sensor comprised of strain gauges that measure the strain on the strut, the strain measured is a result of the aerodynamic drag acting on the actuator disk. Each of the actuator mesh disks listed in Table 3.4 are tested.

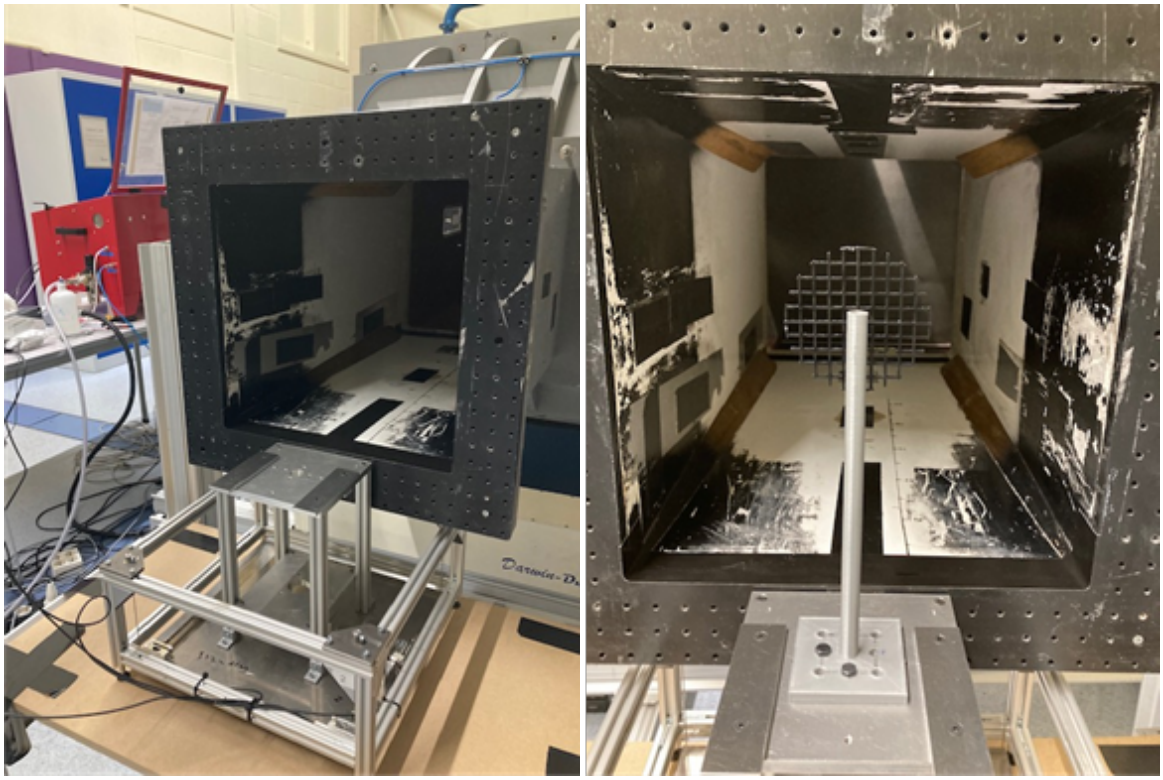

(a) The outlet of the W-tunnel

(b) Actuator disk model installed with force balance

Figure 3.5: The experimental setup of the W-tunnel test with force balance developed by Ming et al. [7]

### 3.1.5. Particle Tracking Velocimetry System

This section presents the utilisation of the Particle Tracking Velocimetry (PTV) system via the Lagrangian Particle Tracking algorithm (LPT) called Shake-the-box (STB) [41], the sub-components of this system include the Helium Soap Filled Bubble (HSFB) seeding generator and the Coaxial Volumetric Velocimetry (CVV) system.

#### Seeding Generator

The production of neutrally buoyant HFSB tracers is achieved by an in-house built Fluid Supply Unit (FSU) attached to a seeding rake that is placed inside the setting chamber of the wind tunnel. The production of the HSFB tracing particles is regulated by mixing air, helium and liquid soap. For optimal fidelity (i.e minimum slip angle and time response) 2 bar of air, 1.8 bar of helium and 2.4 bar of liquid soap are applied. The rake contains 192 probes that are distributed over two rows of 6 wings; these can be observed in Figure 3.6a and Figure 3.6b. The bubbles are fed through the nozzles at equal mass-flow rates; the diameter of the nozzle orifices measures 1mm The seeding rake itself measures $0.6 \times 0.8$ m$^2$ and produces a measurement domain spanning $30 \times 20 \times 20$ cm$^3$ (from Jux et al. [26]); this domain is constrained by the width/height of the bubble stream and the field-of-view (FOV) of the cameras. A single array of nozzles are utilised (96) which is sufficient to maintain a bubbling stream consisting of approximately 25,000 tracers/second; this yields a seeded flow of 5 tracers/cm$^3$.

The seeding rake is positioned inside the setting chamber such that the bubble stream immerses the desired area of study; this measurement volume is shown in Figure 3.3. The measurement volume is taken such that the blade is in the middle ensuring that tracer particles are present on both the pressure and suction side of

the blade. The chosen target area ensures that the bubbles are present when either blade is at an azimuthal position within the range $-10° < \theta < 10°$.

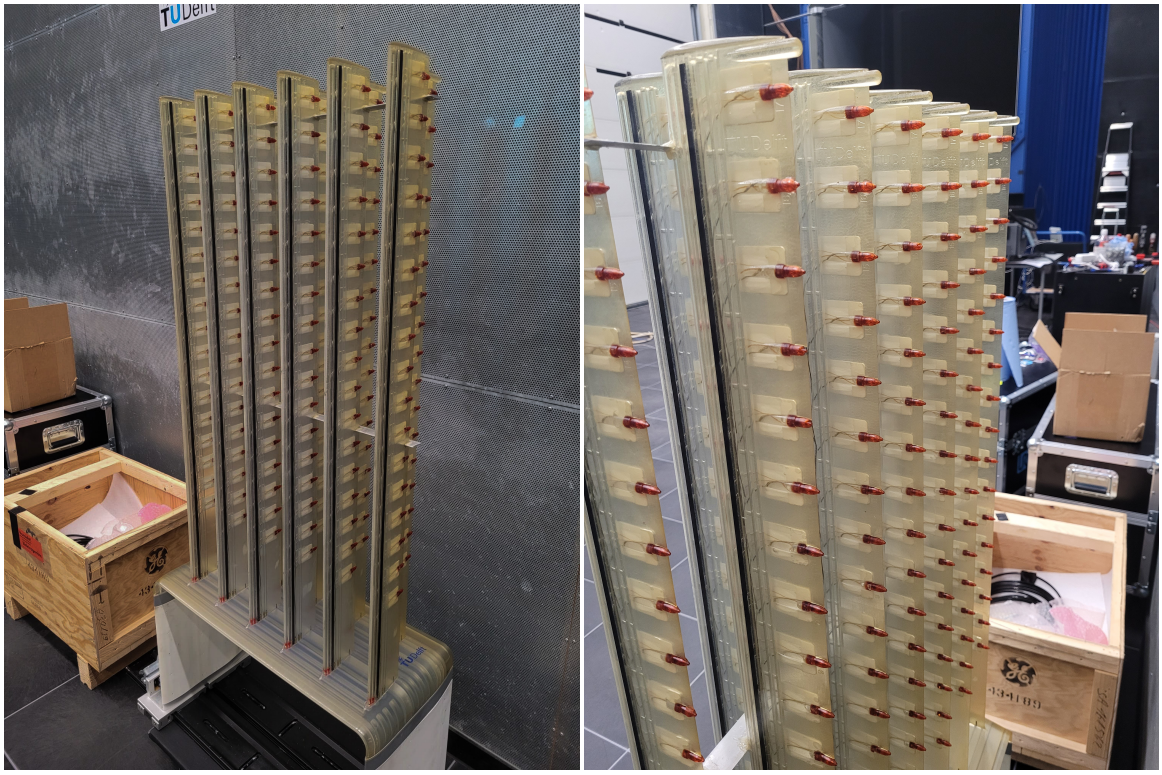

(a) Seeding rake in dry-dock

(b) Seeding rake nozzles

Figure 3.6: The seeding rake used to produce the bubble stream in dry dock

### CVV

The Coaxial Volumetric Velocimetry or CVV, the system consists of several sub-components which include the imager, the robotic arm and the illumination source. The advantage of the CVV system is the superior optical access that is obtained from combining the illumination source and imagers into a single component. This also expedites the process of moving the measurement domain compared to more established tomographic PIV systems. More details regarding the working of the CVV system are provided by Schneiders et al. [42].

The imager is the LaVision$^{TM}$ MiniShaker Aero probe which consists of four metal oxide semiconductor cameras that capture at a resolution of 640 × 476 such that a maximum acquisition frequency of 821.3 Hz is attained. The probe housing is designed to be non-intrusive and measures approximately 130 mm × 90 mm × 80 mm. The volume illumination is provided by the Quatronix Darwin-Duo Nd:YLF laser capable of achieving a frequency of 20 kHz. This source is coupled with an array of lenses before sending light through an optical fibre to the CVV probe. For this experimental campaign, the laser is operated at 22 mJ pulse energy at 1kHz which results in a wavelength of 527nm.

The CVV probe is attached to the Universal Robots UR5 allowing for control of the probe. The robotic arm joints allow for three degrees of rotation and three degrees of translation. When the arm is fully extended a maximum reach of 850 mm can be achieved. Thus, when the mounting position of the robot arm coincides with the centre shaft of the rotor, the diameter of the PitchVAWT completely fits within the range of the robotic arm. Moreover, the robotic arm boasts a repeatability of ±0.1 mm. This data is obtained from the technical specifications provided by the manufacturer: Universal Robots [43]. The robotic arm is operated using RoboDK software. RoboDK allows for interfacing with the robotic arm which enables the user to program target positions in space based on a single calibration step. This allows for rapid data acquisition as the robotic arm moves the probe to its targeted positions based on its programming; data from different

probe positions are subsequently stitched together during post-processing.

### 3.1.6. Test Case Overview

This section functions as an overview of all the test cases that will be completed as part of this experimental campaign. The test cases can be categorised into two parts, the first consists of the acquisition of blade load data and turbine torque which only requires the pitchVAWT to be installed in the wind tunnel. The second requires the full extent of the PTV setup and involves acquiring flowfield data.

The design space of the experiment is constrained by the maximum rotational speed of the turbine, this is limited to 255 RPM. During cases when the wind tunnel is active, the freestream velocity is kept constant at 4.0 m/s which allows for a large range of tip-speed ratios to be tested. Locally, a Reynolds number of Re=2x10$^4$ is achieved based on the freestream velocity and blade chord as characteristics.

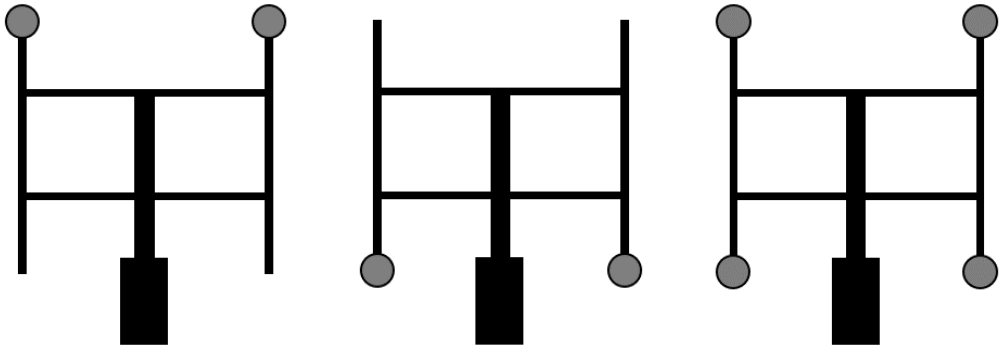

(a) PitchVAWT with top-mounted actuator mesh disks

(b) PitchVAWT with bottom-mounted actuator mesh disks

(c) PitchVAWT with four mounted actuator mesh disks

Figure 3.7: The different configurations of actuator mesh disk mounting on the PitchVAWT blade tips

During the experiment, four mesh disks that function as tip rotors are tested of varying porosity/thrust coefficient, these are listed in Table 3.4. The turbine blades are also tested without the tip rotors, these cases will be called "clean" henceforth. Clean case data is necessary to quantify the effect of the tip rotors. The tip rotors are tested in several configurations: top-mounted (called "top" cases), bottom-mounted (called "bottom" cases) and mounted to all blade tips (called "four" cases); each of the actuator mesh disk configurations is illustrated in Figure 3.7. The top and bottom mounted configurations are there to ascertain (if) any asymmetric behaviour is present. The case where all tip rotors (four) are mounted is preferred since it will further amplify the effect of the tip rotors above the measured noise. Moreover, the rotor sleeves without the mesh disks assembled will also be tested.

All the tests completed during the experimental campaign are listed in Appendix A. Some of the test cases include static noise measurements which are used to correct for inherent electrical noise within the instrumentation of the PitchVAWT. Moreover, data is also collected when the PitchVAWT is ramping to the maximum RPM, this data is necessary when removing centrifugal forces from the strain gauge data, this procedure is referenced in LeBlanc and Ferreira [10]. Furthermore, the tip-speed ratios tested are [2.0, 2.5, 3.0, 3.5, 4.0, 4.5, 5.0].

For the dynamic PTV measurement series, the CVV probe captures the flowfield within a specified domain. To measure the desired domain, the CVV probe must move between pre-defined targets. The probe targets are shown in Figure 3.8. The acquisition time at each target is chosen such that the rotor completes ≈ 100 rotations.

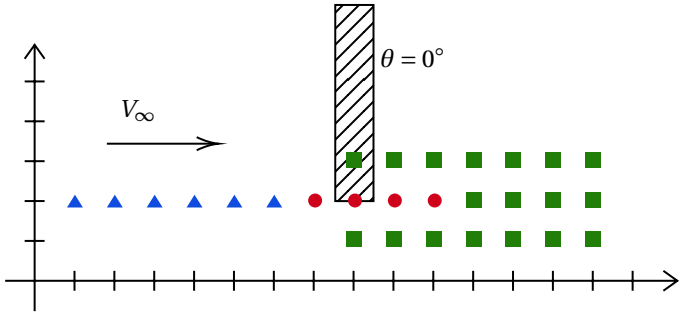


Figure 3.8: The test space with CVV probe targets. ms023, ms025 and ms026 are measured on the smallest domain (●). ms022 and ms024 are measured on the complete domain which is extended downstream (■) and upstream (▲)

## 3.2. Post Processing

In this section, the experimental data post-processing measures will be detailed. There are two main data sources that are presented in the section: the first is blade normal loads, load cell and encoder torque data, and the second section considers post-processing of the PTV data.

### 3.2.1. Blade Loading

As described in Section 3.1.3, the blade normal force data is obtained using full-bridge strain gauges mounted on the top strut of one of the turbine blades. This data is logged by National Instruments™Hardware at an acquisition frequency of 500Hz. The raw data output from the turbine instrumentation contains the voltages measured over the strain gauge, this is the output voltage $V_{\text{out}}$. This voltage is the result of a resistance imbalance in the Wheatstone bridge. An excitation velocity is applied to the strain gauge in order to amplify the small changes in voltage. Additionally, the first few seconds of each measurement point contains static noise measurements, this background noise level is removed from the output voltage in order to retrieve the change in voltage due to the strain gauge imbalance, this step is shown in Equation (3.2).

$$V_r = \frac{V_{out} - V_{noise}}{V_{ex}} \tag{3.2}$$

The manufacturer provides the strain gauge with a gauge factor. The gauge factor is used to determine the strain measured. With the voltage change due to the strain known it is possible to compute the strain on the strut using Equation (3.3), here GF is the gauge factor.

$$\epsilon = \frac{2V_r}{GF\,(1 + V_r)} \tag{3.3}$$

From the strain it is possible to obtain the associated stress using Hooke's Law with the elastic modulus of the strut, this is expressed in Equation (3.4). The axial loading in the strut is determined using the stress and the cross-sectional area of the strut, this is shown in Equation (3.5)

$$\sigma = E\epsilon \tag{3.4}$$

$$F_{ax} = \sigma A_{sect} \tag{3.5}$$

The turbine has two struts equally distributed on each blade, this means that the normal force acting on the blade is twice the axial force on the strut, $2F_{ax}$. This axial force is the total force acting on the blade, when the turbine is rotating this force consists of both the aerodynamic forces and centrifugal forces. In order to isolate the aerodynamic forces acting on the blades the centrifugal forces must be subtracted. This is accomplished by using a polynomial fit of the centrifugal test data, this is further explained in Section 3.3.1.

However, the centrifugal data does contain small aerodynamic effects due to flow curvature, this effect will yield a perceived increase in centrifugal force. In order to correct for the flow curvature an estimation is made using the lift polar of the blade airfoil and the incidence angle w.r.t the flow at the quarter chord.

Finally, when the blade normal forces are corrected for noise and centrifugal forces, the loads are binned azimuthally. In the case of this experimental campaign, the forces are bin-averaged by 5°.

### 3.2.2. Load Cell Data

The turbine is equipped with four load cells which are fixed between the base plate and the main bearing housing. The installation of the load cells can be seen in Figure 3.10; here the load cells are located equidistant from each other at the four corners of the square base plate. A schematic of the load cell pattern is shown in Figure 3.9 where $d$ is the known distance between the load cells. The bending moment on the shaft of the turbine can be determined by evaluating the difference in loads measured between the load cells across each bending axis. The thrust (x-direction) and the side force (y-direction) can then be inferred using the height, $h$, from the base plate to midway along the blades. The forces measured by each load cell are denoted as $L_{x,y}$, $L_{x,-y}$, $L_{-x,y}$ and $L_{-x,-y}$; where the subscript indicates the quadrant of the base plate where the load cell is fixed. A depiction of the load cell arrangement with forces and distances is provided in Figure 3.9, here x is pointing into the flow. Forces in x and y are computed using Equation (3.6) and Equation (3.7).

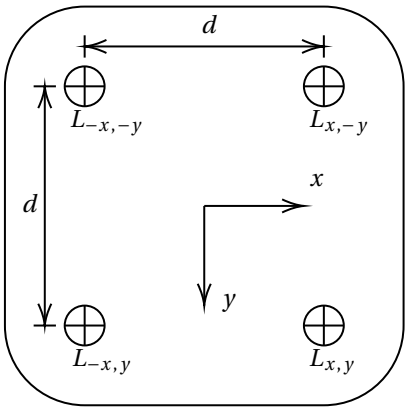


Figure 3.9: A schematic showing the arrangement of the load cells on the base plate

$$F_x = \frac{M_{yy}}{h} = \frac{\left(L_{x,y} + L_{x,-y} - L_{x,-y} - L_{-x,-y}\right) \cdot d}{h} \tag{3.6}$$

$$F_y = \frac{M_{xx}}{h} = \frac{\left(L_{x,y} + L_{-x,y} - L_{x,-y} - L_{-x,-y}\right) \cdot d}{h} \tag{3.7}$$

With the forces defined in Cartesian coordinates, it is possible to determine the thrust magnitude and azimuthal directions using Equation (3.8) and Equation (3.9) respectively. This yields a description of the turbine thrust vector in polar coordinates.

$$|T| = \sqrt{F_x^2 + F_y^2} \tag{3.8}$$

$$\phi_T = \arctan\left(\frac{F_x}{F_y}\right) \tag{3.9}$$

The forces measured by the load cells are also corrected for centrifugal forces. Failing to correct the centrifugal effects will ensure that the thrust magnitude and vector cannot be ascertained from the data. In

addition to being noise filtered, the load cell data is also frequency filtered; this will be discussed in more depth later.

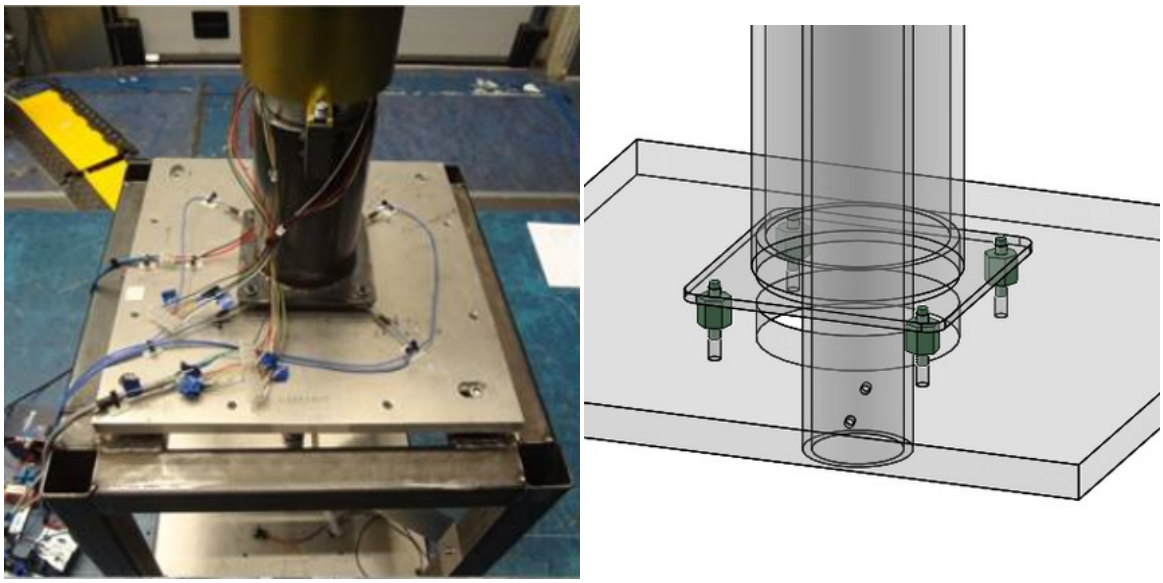

(a) The four load cells mounted between the base plate and main bearing housing

(b) A dimetric view of the load cells at the four corners of the base plate

Figure 3.10: The identical installation of the load cells on the PitchVAWT as used during testing, from [8, 9]

### 3.2.3. Torque Data and Actuator Thrust

Torque data is received from the rotary torque transducer which is placed between the main bearing housing and the generator. The torque measured by the encoder is the torque applied to the turbine shaft in order to operate the turbine at a prescribed tip-speed ratio since the free stream flow velocity is kept constant. An example of the raw torque output is shown in Figure 3.11, note that this data has been binned by tip-speed ratio. The torque shown in the figure includes the torque necessary to overcome internal friction forces, the drag of the blades, the drag of the struts and the drag of the pulleys.

The internal friction is removed by subtracting the torque data measured when the wind tunnel is off and the turbine is rotating (centrifugal tests). Moreover, the drag of the pulleys (used for blade pitching) is a large contributor to the torque; for this, the pulleys are considered as vertically positioned flat plates with a drag coefficient, $C_{D,p} = 1.28$ [44]. Note, that the drag varies along the length of the pulley due to the rotational motion, as does the pulley's contribution to the torque. Equation (3.10) describes the total torque (per pulley, of which there are two) as an integrated value over the length, $r$, of the pulley. Note, $h_p$ is the height of the pulley.

$$Q_p = \int_0^R \frac{1}{2} \rho V_{eff}(r)^2 C_{D,p} h_p r dr \tag{3.10}$$

Once the torque is known, the power can be determined using Equation (3.11). Subsequently one can non-dimensionalise both the torque- and power coefficients. The definition of these coefficients is shown in Equation (3.12) and Equation (3.13) where they are normalised by the freestream velocity, $V_\infty$.

$$P = \omega \cdot Q \tag{3.11}$$

$$C_Q = \frac{Q}{\frac{1}{2} \rho V_\infty^2 A_T R} \tag{3.12}$$

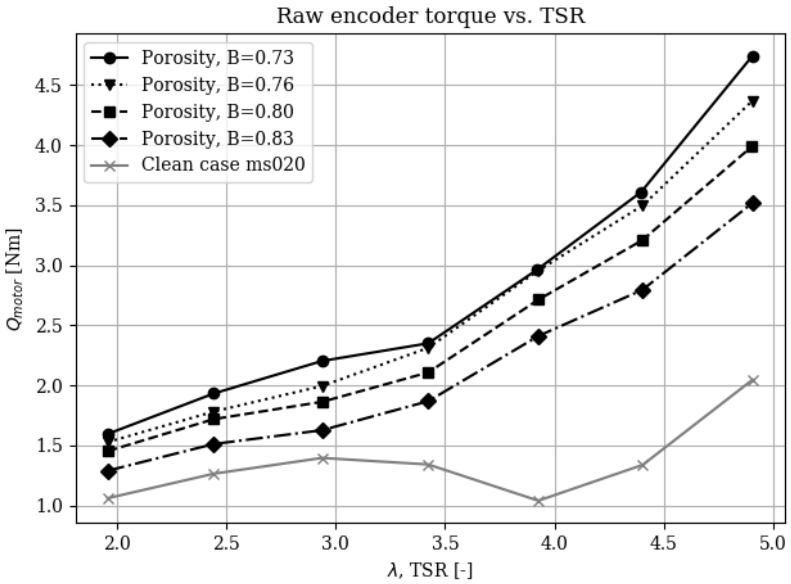


Figure 3.11: The raw torque output from the rotary encoder. This is the torque applied by the motor and includes data from the actuator disks and the turbine in the clean configuration

$$C_P = \frac{P}{\frac{1}{2}\rho V_\infty^3 A_T} \tag{3.13}$$

In order to validate the performance of the actuator disks, the thrust of the actuator disk can be inferred from the torque data with and without the secondary actuator disks installed. In other words, when comparing data without actuator disks to data with actuator disks it is possible to isolate the performance parameters of the actuator disks through subtraction; this is described in Equation (3.14), where $Q_{AD}$ is torque data with actuator disks installed and $Q_{clean}$ is the torque measured without actuator disks.

$$\Delta Q = Q_{AD} - Q_{clean} \tag{3.14}$$

This results in $\Delta Q$ being the difference between these two cases. This difference in torque is attributed to the presence of the tip rotors and can be used to determine the thrust coefficient and power coefficient of the actuator disks, with the power being determined by Equation (3.15).

$$P_{tip} = \frac{\omega \Delta Q}{n} \tag{3.15}$$

$$C_t = \frac{\Delta Q}{\frac{1}{2} R n \rho \overline{V_{eff}}^2 A_{AD}} \tag{3.16}$$

$$C_p = \frac{\Delta Q}{\frac{1}{2} R n \rho \overline{V_{eff}}^3 A_{AD}} \tag{3.17}$$

In Equation (3.16) and Equation (3.17), $R$ is the radius of the primary rotor, $n$ is the number of actuator disks (in this case 4) and $A_{AD}$ is the reference area of the actuator disk. Finally, $\overline{V_{eff}}$ is the azimuth-average of the effective flow velocity $V_{eff}$ experienced by the actuator disk which is defined by Equation (3.18). Note that this expression for the effective velocity neglects any components of the induced velocity due to force fields produced by the blades and actuator disks, thus is exclusively comprised of the rotational speed and freestream flow.

$$V_{eff}(\theta) = \sqrt{(V_\infty \cdot sin(\theta))^2 + (\omega R + V_\infty \cdot cos(\theta))^2} \tag{3.18}$$

### 3.2.4. Frequency Response

So far frequency response has been omitted in the discussion of post-processing, however, it is a key aspect that is present across all data. Therefore, the frequency response post-processing discussed here applies to all previously mentioned data. In Figure 3.12a, a power density spectrum is shown of the raw output voltage of the strain gauge, this functions as an example to show the full range of frequencies measured by the instrumentation. Figure 3.12b shows the spectrum once it is passed through a low pass filter.

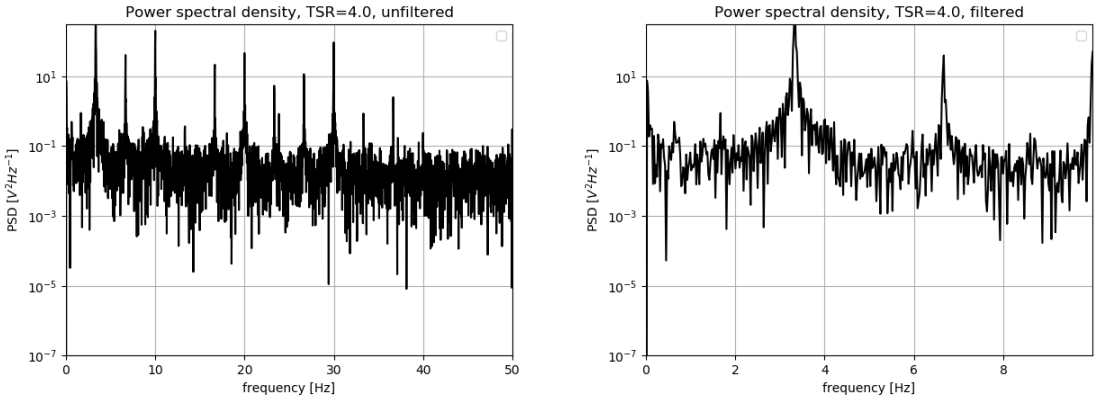


(a) The power spectral density unfiltered

(b) The power spectral density filtered after 3 periods

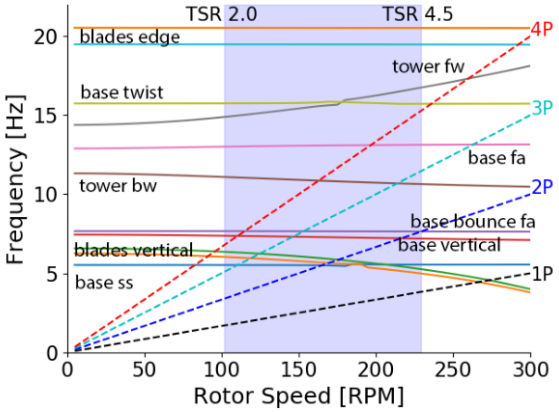


(c) PitchVAWT Campbell diagram produced by LeBlanc and Ferreira [10] for $\lambda = 4$

Figure 3.12: The power spectral density based on the strain gauge voltage at a tip speed ratio, $\lambda = 4.0$ (ms003_mpt002) and the Campbell diagram showing the structural frequencies of the turbine

In their work, LeBlanc and Ferreira [10] produced a Campbell diagram of the pitchVAWT installed in the wind tunnel (see Figure 3.12c). This also shows the periodic motions due to the rotation of the turbine. In the case of a tip-speed ratio, $\lambda = 4.0$, the turbine is operating at $\approx 204$ RPM which in the frequency spectrum amounts to 3.4Hz. In the frequency spectrum, the turbine rotation shows harmonic periods at 2P and 3P and represents frequencies that drive the aerodynamic forces acting on the blades. Other peaks are due to structural motions, such as the swirl of the tower or twisting of the blades, some of these are also shown in Figure 3.12c. From this diagram, it is evident that the large peak at $\approx$ 20Hz is due to structural motion due to bending on the blades, for this reason, the data is low pass filtered after 3P since the high-frequency aerodynamic motions appear to be damped out beyond this. An example of the filtered data compared to the raw output is shown in Figure 3.13 where the normal force of the blades is graphed against the azimuthal position. Note all azimuthally binned data contains at least 100 samples.

Lastly, for the load cells, it was discovered by LeBlanc and Ferreira [9] that there is a resonance frequency

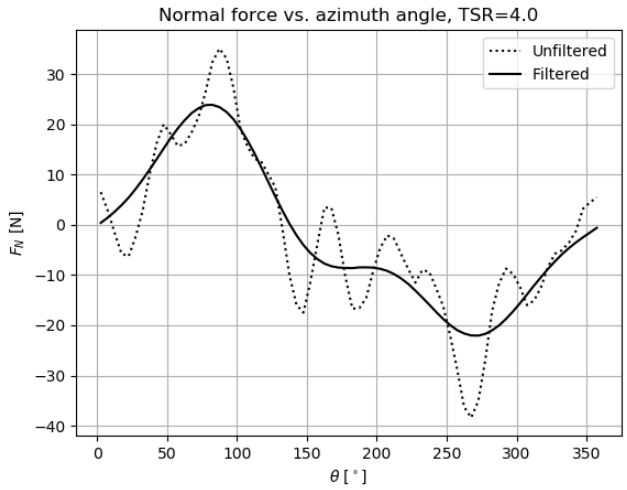


Figure 3.13: Normal force with and without 3P low pass frequency filter applied to it, $\lambda = 4.0$

at 3.47 Hz. To avoid this resonance the data is passed through a band-pass filter that cuts below 4 Hz and above 45 Hz.

### 3.2.5. PTV Data

The objective of the PTV system is to extract and capture tracer particles within the freestream flow, from this one can infer a series of aerodynamic properties. These aerodynamic properties include mean flow velocity, vorticity, and vortex core trajectory amongst others. The instrumentation utilised to acquire PTV data is described in Section 3.1.5. The steps required to extract the aerodynamic properties are detailed in this section. Note, temporal data processing and stitching of volumetric data were conducted by David Bensason; thus the implementation of these steps is omitted.

#### Volumetric Self Calibration

The first step for post-processing the PTV data requires a geometric and volumetric self-calibration; the process of the volumetric self-calibration is presented in the work of Wieneke [45] and will be reiterated in here in short. This calibration is performed by triangulating the 3D particle positions within a volume using the 2D particle positions obtained from each camera. The particle positions are mapped using the best-fit scheme which minimises the distances between 2D particle location $(x_i, y_i)$ and the projection of the 3D triangulated position $(x_i', y_i')$ on the camera image, this is known as the disparity $d_i$ and is defined in Equation (3.19).

$$d_i = (x_i, y_i) - (x_i', y_i') \tag{3.19}$$

Disparity maps are produced for each camera and are the result of multiple recordings summed together. The highest disparity peaks inform which disparity vector is used to correct the vector field. This process is repeated until a satisfactory disparity is yielded, this is in the order of 0.1-0.2 pixels.

As an additional step to the calibration, a non-uniform optical transfer function (OTF) is utilised as described by Schanz et al.[46]. The OTF is calibrated using the same data obtained from the volumetric self-calibration, the shape parameters of the OTF are tuned to the shape of the particles within individual sub-volumes. This allows for OTF maps to be determined and used to reconstruct the peak position of each particle. Applying the OTF to the experimental data improves the accuracy of the particle positions by reducing optical distortions such as blurriness and crucially suppressing the presence of ghost particles. The latter is the result of a single particle "appearing twice" as it is not recognised as the same particle by two separate cameras.

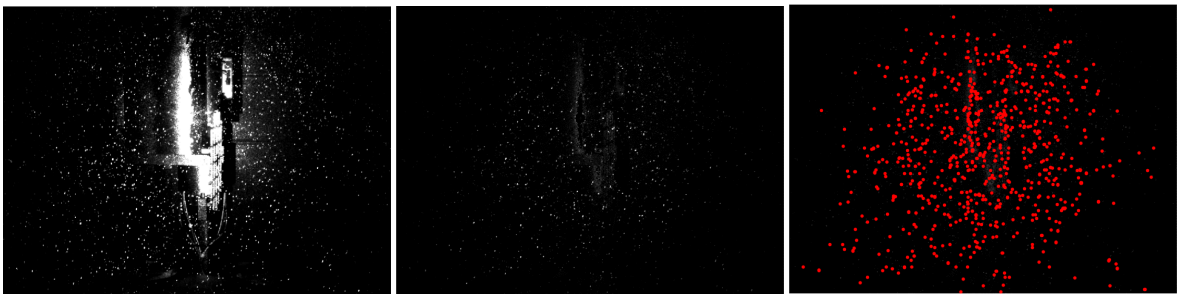

(a) Unprocessed image of the flowfield with the blade and actuator disk in view

(b) Pre-processed image of the flowfield with tracer particles isolated

(c) Tracer particles identified by the tracking software

Figure 3.14: Samples of images captured by the PTV system. The raw image shows large bright spots produced by reflections coming off the turbine blade and actuator disk assembly. The pre-processed image is refined using a Butterworth filter before the tracking software identifies the tracer particles, in Figure 3.14c ≈ 800 tracers are identified in the frame

### Image Pre-Processing

The removal of noise due to the unsteady (due to rotation) light reflections is treated using a high pass frequency filter in the form of a Butterworth filter, how this is applied is presented in the work of Sciacchitano and Scarano [47]. This step is subsequently followed by a directional minimum filter with a local pixel size of $5 \times 5$ px$^2$. An example of the images that result from the pre-processing is shown in Figure 3.14b. In Figure 3.14a the reflections of the blade and actuator disk cause bright illuminations in the image, drowning out the reflected light from the particles. However, once the pre-processing is completed it is possible to identify particles in the regions illuminated by the blade and actuator disk reflections, this is evident in Figure 3.14c.

### Lagrangian Particle Tracking

The implementation of the Lagrangian Particle Tracking (LPT) is conducted through an algorithm known as Shake-the-Box (STB), the methodology of this procedure is presented by Schanz et al. [27]. LPT is desirable for it enables the tracking of tracer particles contained within a flow; from this, it is possible to infer local velocities and accelerations without spatial averaging. The positions of tracer particles are determined similarly as described in the volumetric self-calibration; where particles are triangulated within a volume by an array of cameras (four cameras in the case of the present study) for multiple time steps. The key limitation of this method is the particle density, insufficient tracer density results in coarse spatial resolutions whilst too high tracer densities introduce many ghost particles. The ghost particle issue is improved by the volumetric self-calibration procedure. For successful usage of LPT, one should aim to achieve 0.005 particles per pixel [27].

STB uses an iterative procedure in which images are overlapped and matched using the 3D Gaussian peak fitter, Novara and Scarano [48]. The iterations are completed by "shaking" the particles such that the local residual of the fitter is reduced. On the temporal domain, STB uses the available velocity information to extrapolate trajectories and thus predict particle distributions for subsequent time steps. This yields a rapid process for handling 3D data with high particle precision.

Once the tracking is concluded, the particle tracks are converted from the probe reference frame to the turbine-centred reference. This coordinate change is conducted for each set of volumetric data which allows for all the measurement domains to be concatenated thus yielding the complete measurement domain.

## 3.3. VERIFICATION

In this section, the results of the experimental campaign will be compared to pre-existing data to verify the credibility of the experiment. The verification will be limited to the data on the blade force distribution and the turbine thrust forces.

### 3.3.1. TURBINE OPERATION

As previously mentioned, the pitchVAWT is a model turbine that pre-exists the present experimental campaign; it is a system developed by LeBlanc and Ferreira [9]. Although the previously conducted work using the pitchVAWT differs from the work present in this document, certain sets of data are similar in both works and thus provide grounds for verification. This verification analysis will provide an indication of whether the turbine is operating consistently thus meaning experimental results are repeatable. Moreover, this analysis will highlight any abnormalities such as blade imbalances or errors in faulty strain gauges which might have arisen during the turbine's time in storage.

An initial "sanity" test was conducted during the experimental campaign, this data is collected in ms001. The data in this measurement series is obtained by gradually ramping the rotational speed of the turbine from 0 to 25 rad/s. Forces measured are a direct result of the strut-mounted strain gauges from which the output voltage is converted to a strain/force (as explained in Section 3.4.1). This data is used to correct centrifugal loads but also functions as a means to verify nominal operations of the turbine when compared to data found by LeBlanc and Ferreira [10]. A comparison between these two data sets is shown in Figure 3.15a, in this figure the polynomial fit retrieved from the data is presented for the present experimental campaign and the work conducted by LeBlanc and Ferreira. Comparisons between the two polynomial fits show acceptable congruence between the two experiments; this is particularly the case for the range of rotational frequencies investigated in this experiment. The experiment will require the turbine to operate between the range of 10-26 rad/s, from Figure 3.15a it is apparent that there is on average a 2% deviation with the results from LeBlanc and Ferreira in this range. From this one can conclude that the turbine was operating nominally during the experiment.

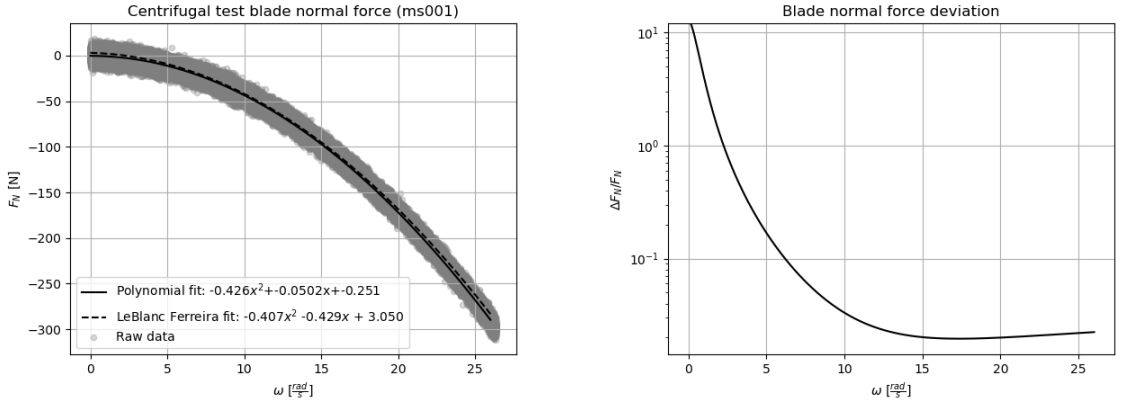


(a) Centrifugal test raw data with polynomial fit

(b) Deviation of present results and data from LeBlanc and Ferreira

Figure 3.15: Raw blade normal force measure by strut-mounted strain gauges. A polynomial fit is derived from the experimental data and compared to a similar analysis by LeBlanc and Ferreira [10]. The deviation between the present results and the data from LeBlanc and Ferreira is presented as a fraction of the normal force measured, $\Delta F_N/F_N$

### 3.3.2. LOAD CELL MEASUREMENTS

As described in Section 3.2.2, data from four load cells are also collected. This data can be used to determine the forces in the x- and y-direction acting on the turbine, thus allowing one to infer the total thrust produced by the turbine (and its direction). The thrust loading has extensively been tested by LeBlanc and Ferreira in [11], this data provides the opportunity to compare results between two separate experiments on the same turbine. From this comparison, conclusions can be made about the robustness of the experiment and the

validation of the experimental data collected in this test.

As previously mentioned in Section 3.4.1, the load cell data is band-pass filtered below 4 Hz and above 45 Hz. This filter is consistent with the methodology presented by LeBlanc and Ferreira in [9]. In Figure 3.16, experimental data from ms020 is presented and compared to similar data collected by LeBlanc and Ferreira in [11] at a tip-speed ratio of 3.5. The experimental data presented for this campaign consists of at least 100 rotations binned at 5° azimuth. Looking at Figure 3.16a shows the force coefficient in the x-direction, two peaks are distinguishable and are located at roughly 90° and 270° azimuth, this is consistent since one expects peak forces in the x-direction when the blade is most upwind (90° azimuth), the peak at 270° is the result the second blade being upwind. Compared to the results of LeBlanc and Ferreira, the peaks are located at similar positions, however, there is a discrepancy in the magnitude of the first peak. From Figure 3.16a it appears that in the data of LeBlanc and Ferreira, blade 1 appears to be more heavily loaded since its peak is larger than the second peak. The difference in peak loads suggests a combination of two phenomena are at work in the experiment of LeBlanc and Ferreira: first, that blade 1 is more heavily loaded than blade 2 and second that there is a forward-to-rearward tilting motion of the turbine shaft. In any case, it is desired to have the peak forces be equal for this suggests that the turbine is operating symmetrically in the x-direction. Another notable difference between the two data sets is a slight bump in force around $\theta = 150°$, this bump is present in the current data but is absent in the results of LeBlanc and Ferreira. This bump is likely the result of local dynamic stall of the blades, this has been witnessed by Ferreira et al. [24] to occur at azimuth angles of $\approx 110°$. The reason that the dynamic stall is not shown in LeBlanc and Ferreira's data is likely the result of dissimilar filtering approaches, in [11] the authors describe utilising notch filters to further smooth the results; these notch filters have not been used in the present data since no vibrational analysis has been conducted. Moreover, data from vibrational and structural tests presented in [6] have been found not to apply to the present work due to variations in the mounting of the turbine inside the wind tunnel. Regardless, it appears that in terms of peak loads in the x-direction, the data from the load cells appears to be consistent with previous works.

In Figure 3.16b, the force coefficient in the y-direction is plotted against the azimuth angle. When compared to the result of LeBlanc and Ferreira [11] several differences are evident. First, note the asymmetry between blade forces in the data collected during this campaign. When blade 1 is upwind, the force coefficient is more negative compared to when blade 2 is upwind. Another difference is observed around peaks when the blades are around $\theta = 110°$, in the current test data the rate of increase in force coefficient decreases likely due to dynamic stall. As mentioned prior, this phenomenon does not appear in the works of LeBlanc and Ferreira likely due to differences in post-processing. The off-peak comparisons between the two data sets appear to be very consistent, it is the peak behaviour that is dissimilar between the two studies.

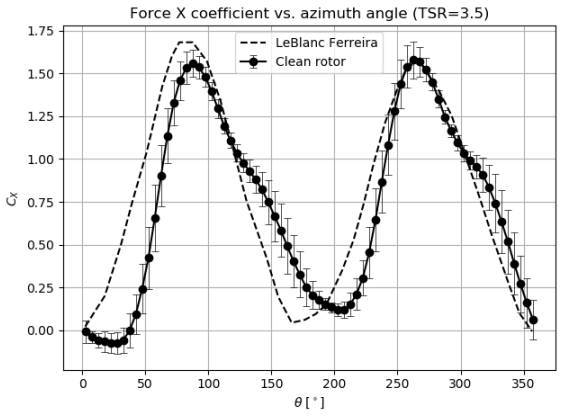


(a) Coefficient for the force in x-direction versus azimuth angle with an average standard deviation of $\bar{\sigma} = 0.10$

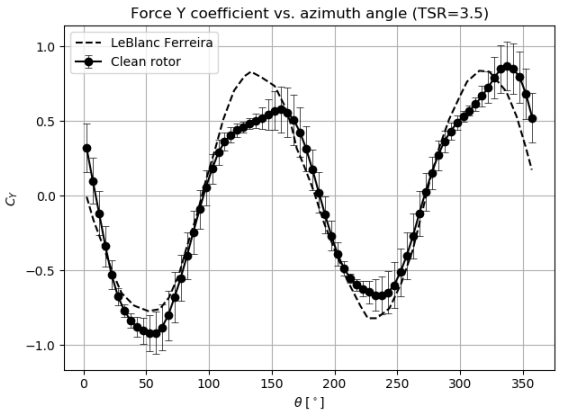


(b) Coefficient for the force in the y-direction versus azimuth angle with an average standard deviation of $\bar{\sigma} = 0.11$

Figure 3.16: Force coefficients in x- and y-direction derived from the load cell data. All data is gathered at a tip-speed ratio of 3.5; also plotted is the data collected by LeBlanc and Ferreira in [11]. The test data presented is retrieved from ms020

### 3.3.3. TURBINE PERFORMANCE

Turbine performance can be quantified by the non-dimensional value of the power coefficient. There is much research conducted on the performance of VAWTs [23, 49–52], as such there is an abundance of test cases to compare the results for the pitchVAWT performance too.

In Figure 3.17, the power coefficient of the pitchVAWT in the clean configuration (without tip-rotors) is presented. The reader is reminded that the specification of this turbine can be found in Table 3.1. A peak power coefficient of 0.37 is achieved at a tip-speed ratio of 4.5. This result is consistent with data on similar low solidity VAWTs even those using the NACA0018 airfoils such as in Battisti et al. [51], their peak power coefficients were found to be of a similar order of magnitude. They are notable differences between the experiment conducted in the present campaign and the experiments conducted by Battisti et al., these include rotor solidity and Reynolds number. Nevertheless, this comparison ultimately provides adequate verification of the pitchVAWT power performance which in turn verifies the means through which this data has been acquired, namely the torque transducer and the methods of post-processing described in Section 3.4.1.

Finally, it is observed that the turbine underperforms significantly for $\lambda < 4.0$ as evidenced by the sharp drop in power coefficient. Moreover, for $\lambda < 3.0$ are seen in Figure 3.17 the power coefficient is found to be negative; this result is due to how the power is measured. The power "extracted" by the turbine is assumed to be equal to the power delivered by the motor to operate the turbine at a predefined tip-speed ratio. At low tip-speed ratios, the losses due to drag are very high which results in low power performance. Additionally, the Reynolds number becomes of the order $Re = 3.3 \cdot 10^4$ for TSR=2.0; such low Reynolds numbers likely introduce flow separation on the airfoil which impairs its performance. The phenomenon of dynamic stall does have consequences for the performance of actuator mesh disks at low tip-speed ratios, as such when determining the tip rotor performance these data points should be excluded.

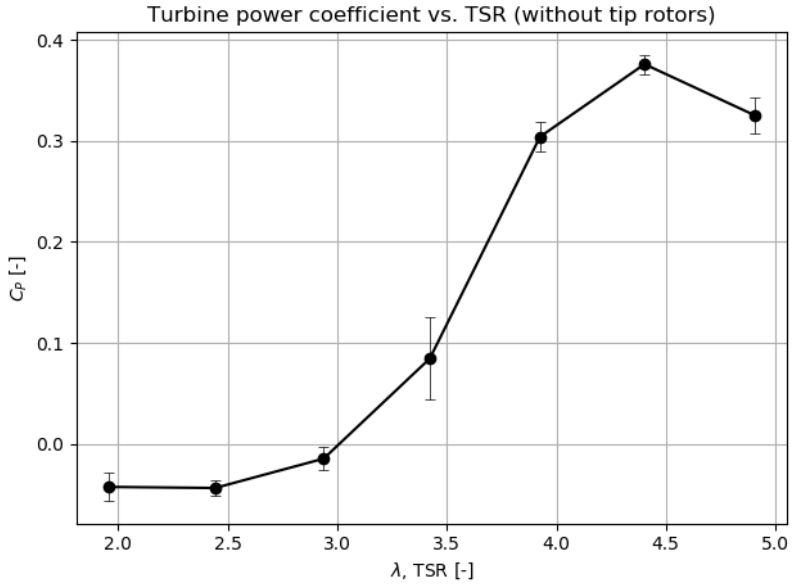


Figure 3.17: Power coefficient versus tip-speed ratio for the pitchVAWT. Measurements were conducted at a freestream velocity of $V_\infty = 4.0$ m/s and at a Reynolds number of $Re = 7.5 \cdot 10^4$ (which is based on the maximum tip-speed ratio)

## 3.4. RESULTS

This section presents the results of the experimental campaign. The performance of the turbine will be assessed with the presence of actuator mesh disks on the blade tips. Furthermore, the performance of the actuator mesh disks will be evaluated based on the results for the torque and the flow field data acquired by the PTV.

### 3.4.1. BLADE LOADING

The experimental results will be treated in several parts due to the large degree of variation in the available data. In this section, the blade loading data will be presented which includes data obtained from the strut-mounted strain gauges and thrust measured by the load cells.

As mentioned previously, several configurations of actuator mesh disk mounting have been tested, these include top mounting, bottom mounting and the combination of top and bottom mounting (four actuator mesh disks). In Figure 3.18, normal force coefficient data from the three actuator mesh disk configurations are shown at a tip-speed ratio of $\lambda = 4.0$ for all levels of mesh disk porosity.

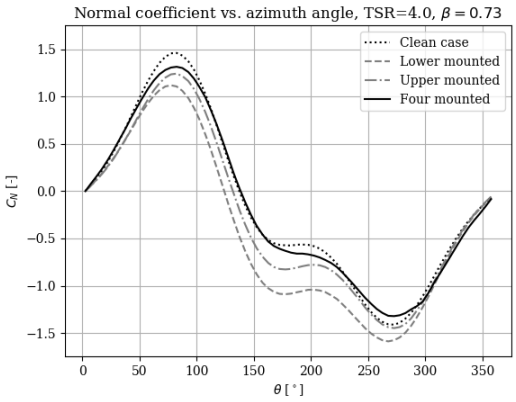


(a) Blade normal force coefficient plotted azimuthally for $\beta = 0.73$, average variation of 0.19 w.r.t the clean case

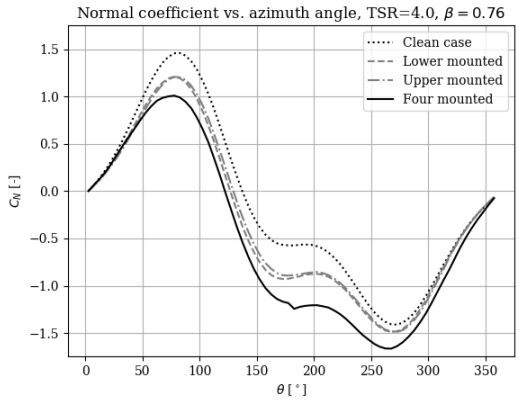


(b) Blade normal force coefficient plotted azimuthally for $\beta = 0.76$, average variation of 0.17 w.r.t the clean case

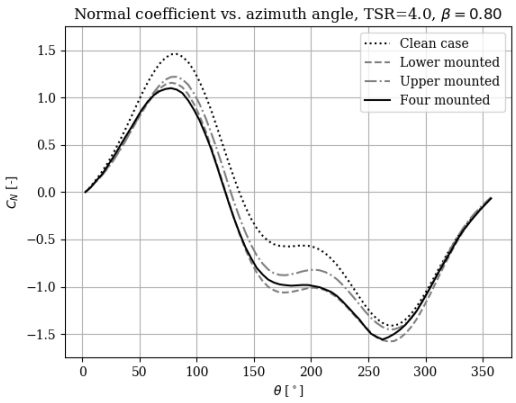


(c) Blade normal force coefficient plotted azimuthally for $\beta = 0.80$, average variation of 0.20 w.r.t the clean case

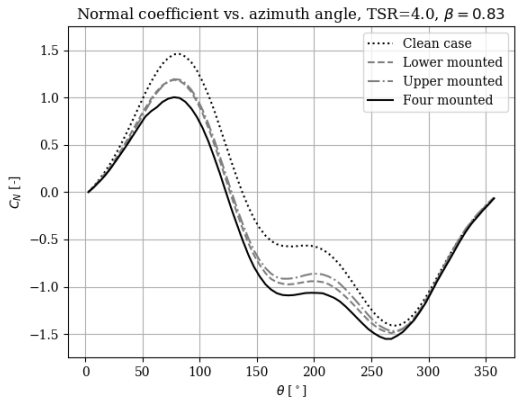


(d) Blade normal force coefficient plotted azimuthally for $\beta = 0.83$, average variation of 0.18 w.r.t the clean case

Figure 3.18: Blade normal force coefficient plotted azimuthally for the four porosities of actuator mesh disk. These results are averaged based on two actuator mesh disk configurations: one with top-mounted disks and the other with bottom-mounted disks. All data shown is for TSR=4.0

Glancing at Figure 3.18 it becomes evident that the presence of the actuator mesh disk appears to have a reductive effect on the blade's normal force coefficient. Across all the levels of porosity tested, the deficit w.r.t the clean case (without actuator mesh disk) is greatest around 90° and 180°, this azimuth range is also prone to dynamic stall. There is no clear correlation between the magnitude of the normal force coefficient

and the porosity of the actuator mesh disk, the largest normal force coefficient observed is $C_N = 1.23$ for $\beta = 0.76$ (Figure 3.18b). The lowest observed normal force coefficient is $C_N = 1.20$ for $\beta = 0.73$ (Figure 3.18a). On average when compared to the clean case, the peak normal force coefficient underperforms in the upwind part by 15% when actuator mesh disks are mounted. Conversely, on the downwind part of the rotation, the forces magnitude of the normal force is greater when the actuator mesh disks are present, and the peak performance in the downwind region is on average 6% higher (in absolute terms) when the actuator mesh disks are present. When comparing the actuator mesh disk cases to one another, the differences between the top and bottom cases are $\approx 2\%$, thus any observed variations are not distinct from experimental uncertainties. For the configuration with four actuator mesh disks, the results yield lower normal force coefficients than the top and bottom cases for all porosities with the exception of $\beta = 0.73$.

It also appears that the case with the upper-mounted actuator mesh disks yields higher normal force coefficients for certain porosities when compared to the lower-mounted case. The explanation for this is in part due to experimental uncertainties but it can also be backed up by the claim that there are more perturbations for the lower-mounted actuator mesh disk due to them being in closer proximity to the turbine base and shaft. Overall, the effect of the actuator mesh disks on the blade's normal force coefficient is expected to be minimal since the primary force produced by the mesh-disk acts tangentially (in the rotations path). Likely, the deviations w.r.t the clean case seen in Figure 3.18 are the result of actuator disk wakes affecting the blade tip region.

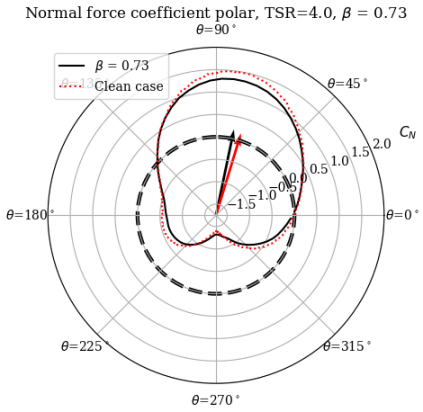


(a) Polar plot of the normal force coefficient and total thrust direction for $\beta = 0.73$, the thrust variation is 5.1°

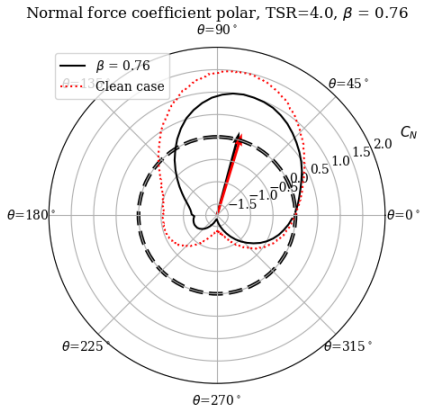


(b) Polar plot of the normal force coefficient and total thrust direction for $\beta = 0.76$, the thrust variation is 1.9°

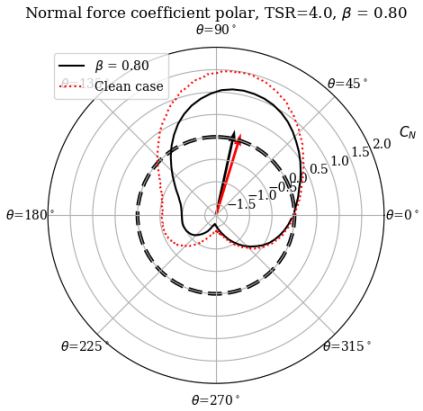


(c) Polar plot of the normal force coefficient and total thrust direction for $\beta = 0.80$, the thrust variation is 4.5°

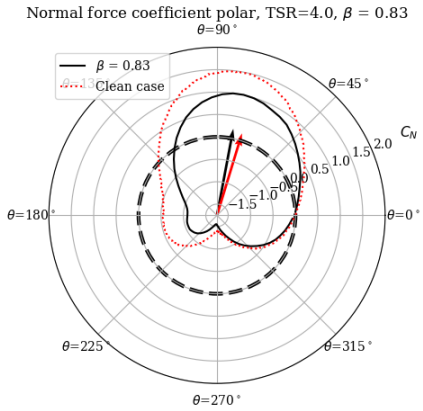


(d) Polar plot of the normal force coefficient and total thrust direction for $\beta = 0.83$, the thrust variation is 6.3°

Figure 3.19: Polar plots of the normal force coefficient plotted azimuthally for each porosity for the actuator mesh disk in the four-mesh disk configuration. The thrust vector and normal force coefficient variation w.r.t the clean case are also plotted. Results shown are for TSR=4.0

In Figure 3.19 polar plots are presented for each porosity of the actuator mesh disk for the four mesh disk configuration. These plots show the normal force coefficient ($C_N$) of the pitchVAWT blades as a function of the azimuth position of the blade. Similarly to the Cartesian plots in Figure 3.18, each actuator mesh

disk case is compared to the pitchVAWT in its clean configuration. Lastly, each figure contains an arrow indicating the direction of the pitchVAWT thrust vector for the actuator mesh disk case (in black) and the clean case (in red), thus indicating the thrust variation.

The polar plots shown in Figure 3.19 are obtained at a tip-speed ratio of 4.0. The variation of the thrust direction observed in the actuator mesh disk cases is minimal but not insignificant. The average thrust variation that is observed across all the presented actuator mesh disk cases consists of a 4.5° deviation which results in a more leeward thrust vector. Upon analysing the thrust direction and the normal force distribution it is clear once more that the changes in normal force (for the actuator mesh disk cases) are not causing a more leeward thrust vector, the key argument for this is that the locations of the peaks shown in Figure 3.18 are consistent between the actuator mesh disk case and the clean case. Mostly likely the azimuthal distribution of the tangential force field is driving the thrust direction variations since the tangential blade forces are more heavily affected by the drag of the actuator mesh disks which acts in the tangential direction.

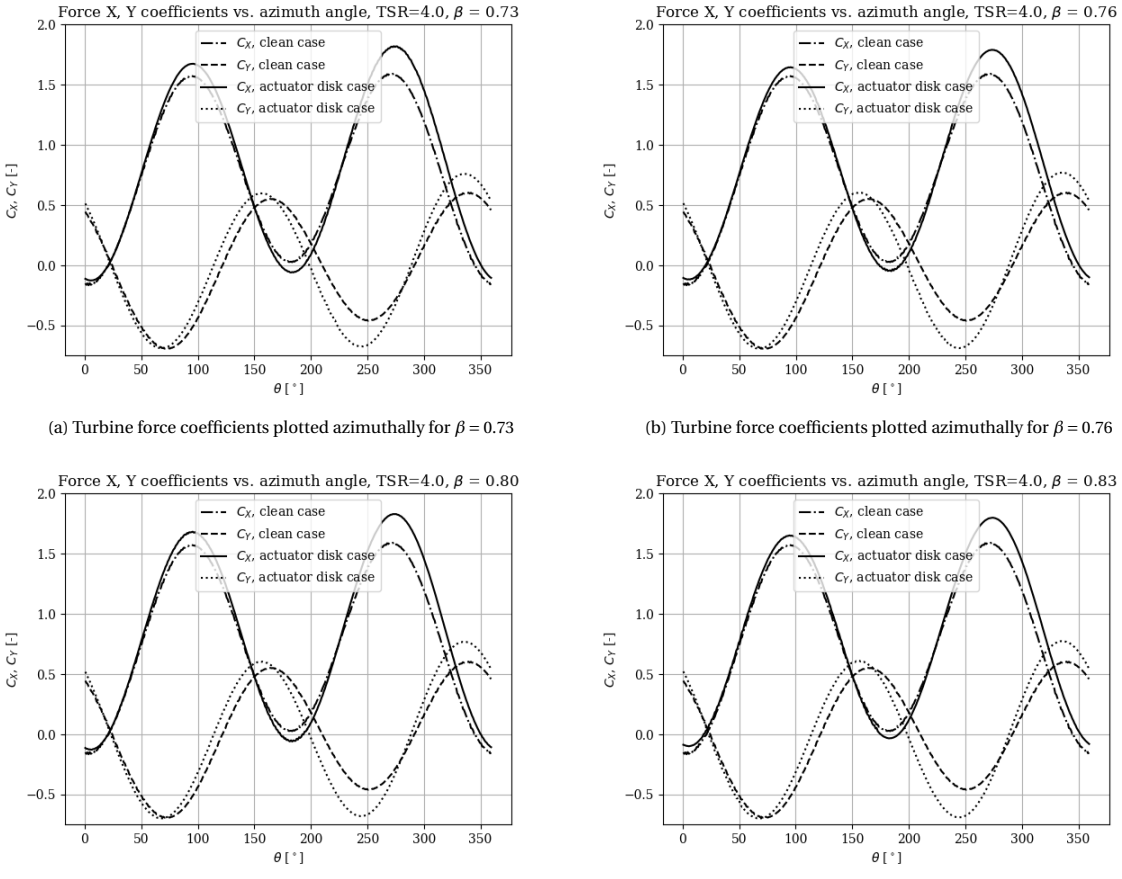


(a) Turbine force coefficients plotted azimuthally for $\beta = 0.73$

(b) Turbine force coefficients plotted azimuthally for $\beta = 0.76$

(c) Turbine force coefficients plotted azimuthally for $\beta = 0.80$

(d) Turbine force coefficients plotted azimuthally for $\beta = 0.83$

Figure 3.20: Turbine force coefficients plotted azimuthally for the four porosities of actuator mesh disk. These results are obtained from cases where four actuator mesh disks are mounted to each blade end (upper and lower). All data shown is for TSR=4.0 and binned at 1° azimuth

In order to gain insight into the variation in thrust direction observed in Figure 3.19 it is fruitful to look at the distribution of forces acting in x- and y-direction. The forces in x- and y-direction are obtained from load cell measurements at the turbine base thus they measure the total force acting on the turbine, the process of acquiring this data is explained in Section 3.2.2. The results of Figure 3.20 show the turbine force coefficients in x- and y-direction; the data consists of the cases where actuator mesh disks were mounted on the upper and lower blade ends. The behaviour shown in the figures is expected for both $C_X$ and $C_Y$, where the former is characterised by a periodic distribution that stays positive and the latter a periodic distribution that oscillates around zero. Initial impressions indicate that the presence of actuator mesh disks appears to increase the magnitude of the forces, particularly in the x-direction. This result is expected since the actuator mesh disks contribute to an increase in drag which is a key force that acts in the windward

direction (x). For $C_X$, the location of the peaks appears similar to the clean case with the exception of Figure 3.20a. Additionally, there appears to be a degree of asymmetry between the two blades for the cases with actuator mesh disks. Recalling that the azimuth position denoted in Figure 3.20 is the position of blade 1, it is apparent that blade 2 is more heavily loaded when it is upwind (i.e blade 1 is downwind). This is deemed to be a systematic error for it appears in all cases that might be due to a difference in blade pitch between the two blades.

Accounting for the asymmetry in blade loading, it appears that the $C_Y$ magnitudes are relatively similar between the actuator mesh disk cases and the clean case. However, what is evident is a shift in the location of the peak $C_Y$ value. For three out of the four cases, the shift in peak location observed around $\theta = 165°$ consists of about 10°; this ultimately results in a more leeward location of the peak $C_Y$ value. This shift appears to be of similar magnitude across all the cases compared in Figure 3.20 with the exception of the $\beta = 0.73$ case (Figure 3.20a) which shows a shift of roughly 5°.

The forces in the x- and y-direction are shown in Figure 3.20 and are combined to yield the azimuthal distribution of the turbine thrust coefficient. The thrust coefficient is shown in Figure 3.21 is presented for each actuator mesh disk case. Many of the characteristics observed in Figure 3.20 carry over to Figure 3.21, with most notably the increase in thrust coefficient when the actuator mesh disks are present. Artefacts such as the blade load imbalance are also visible, with blade 2 being more heavily loaded. One additional observation that can be made is by looking at the location of the thrust coefficient peaks. All peaks show an average leeward shift 2.5° which is consistent with the observation made in Figure 3.19 where the direction of the total thrust is more leeward for the actuator mesh disk cases.

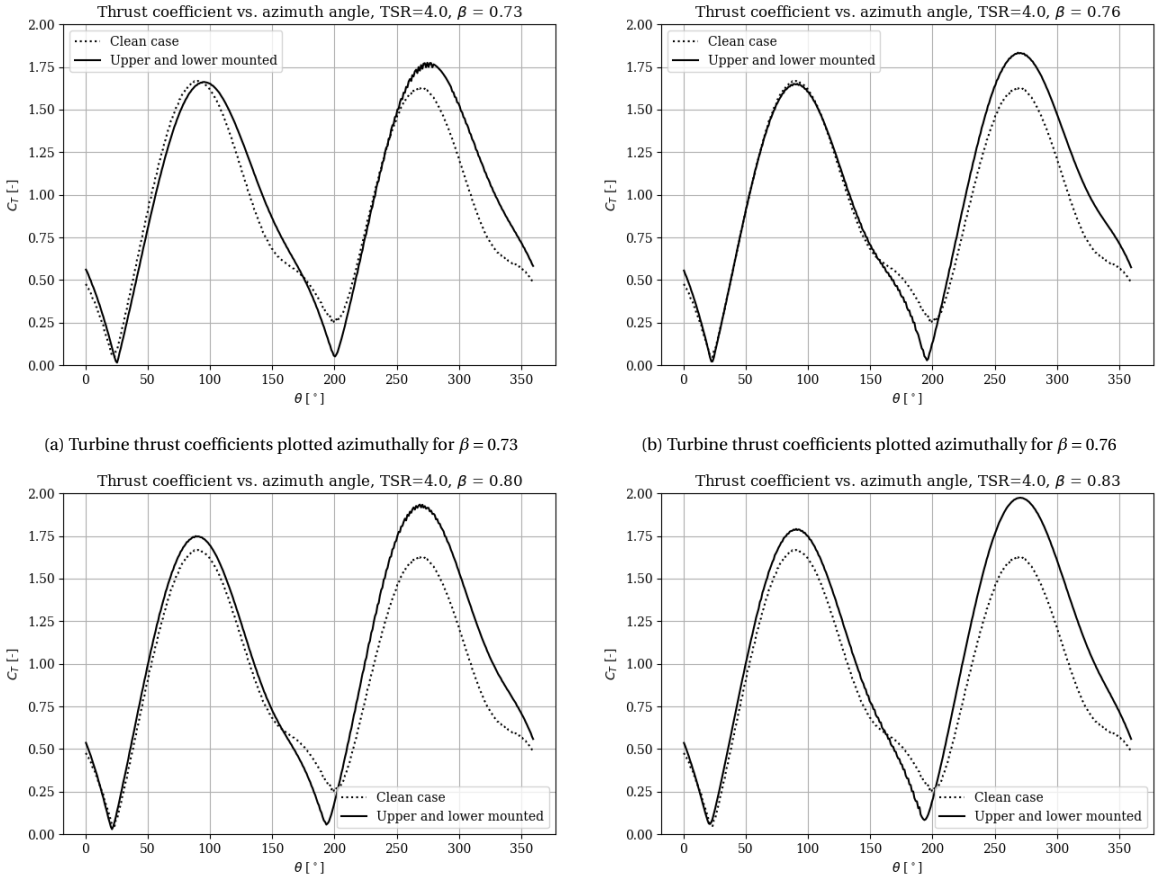


(a) Turbine thrust coefficients plotted azimuthally for $\beta = 0.73$

(b) Turbine thrust coefficients plotted azimuthally for $\beta = 0.76$

(c) Turbine thrust coefficients plotted azimuthally for $\beta = 0.80$

(d) Turbine thrust coefficients plotted azimuthally for $\beta = 0.83$

Figure 3.21: Turbine thrust coefficients plotted azimuthally for the four porosities of actuator mesh disk. These results are obtained from cases where four actuator mesh disks are mounted to each blade end (upper and lower). All data shown is for TSR=4.0 and binned at 1° azimuth

Finally, the relation between the peak thrust coefficient and the actuator mesh disk porosity is shown in

Figure 3.22a. Note that the peak thrust has been averaged between the two peaks in order to account for the blade imbalance that has been observed. Furthermore, Figure 3.22a suggests that the peak thrust coefficient is proportional to the porosity, thus meaning it is inversely proportional to the thrust coefficient of the actuator mesh disk. Looking at the integrated thrust coefficient in Figure 3.22b a largely similar relationship is observed. This result suggests that the presence of an actuator mesh disk impairs the total thrust of the turbine, this effect is greater when the porosity is lower (i.e the actuator mesh disk thrust coefficient is higher). This is also consistent with the observation regarding the blade normal forces which were reduced by the effect of the actuator mesh disks.

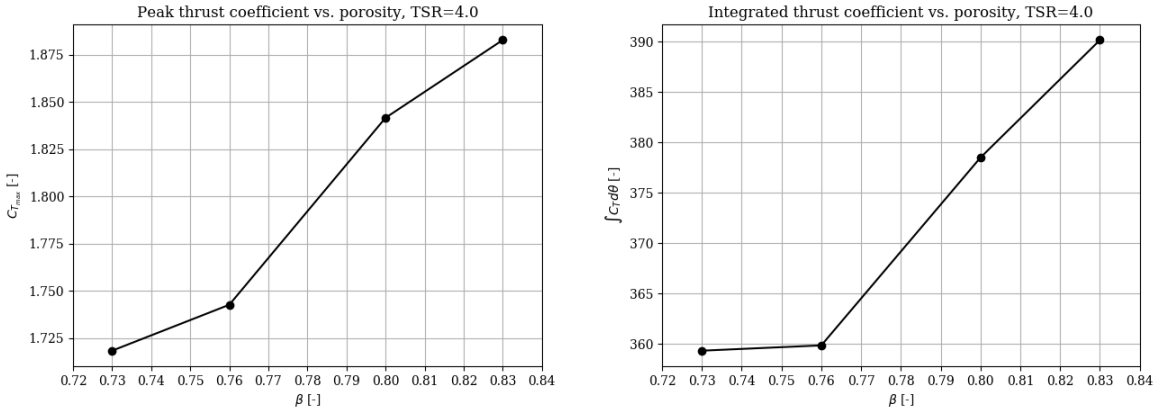


(a) Average peak turbine thrust coefficient as a function of the actuator mesh disk porosity

(b) Integrated turbine thrust coefficient as a function of the actuator mesh disk porosity

Figure 3.22: Relations between the actuator mesh disk porosity and the thrust performance of the turbine. These results are obtained from cases where four actuator mesh disks are mounted to each blade end (upper and lower). All data shown is for TSR=4.0 and binned at 1° azimuth

### 3.4.2. ACTUATOR MESH DISK PERFORMANCE

In this section, the performance of the actuator mesh disks will be evaluated based on the torque data acquired during testing in addition to static PTV tests of the actuator mesh disks. The key performance parameter that will be analysed for the actuator mesh disks is the thrust coefficient. In Section 3.2.3 a description is provided for the methodology and post-processing employed to ascertain the actuator mesh disk thrust coefficient from the change in torque measured between cases with the actuator mesh disk and the clean case. Details on how the PTV data is retrieved can be found in Section 3.2.5.

First, the data obtained from the PitchVAWT test with the actuator mesh disks are discussed. The performance of the actuator mesh disk is evaluated by estimating the thrust coefficient. The present experiment with a rotating turbine yields torque data measured at the base of the turbine; as mentioned previously the torque data can be used to infer the thrust force on the actuator mesh disks. This data is collected for each of the cases presented in Table A.1 and can be statistically averaged to determine the actuator mesh disk thrust coefficient. In Figure 3.23 the actuator mesh disk thrust coefficient is presented as a function of the tip-speed ratio for the four porosities tested. The definition of the thrust coefficient requires the thrust to be non-dimensionalised by the tip-speed ratio amongst other parameters, thus it is expected that the thrust coefficient is invariant of the tip-speed ratio from a theoretical perspective. However, Figure 3.23 shows large deviations in the measured thrust coefficient. The four actuator mesh disk cases show similar trends with peak thrust coefficients observed at $\lambda = 2.0$ before reaching a minimum between the values of 3.0 and 3.5. At higher tip-speed ratios the value of the thrust coefficient climbs once more and appears to be more stable between 4.0 and 5.0. The decrease in measured thrust coefficient is an interesting result and cannot be ignored based on the magnitude of the decrease, the difference between the maximum and minimum thrust coefficient amounts to 0.3 on average across all actuator mesh disks. It is likely that structural harmonic behaviours are at play here and are influencing the results measured, this was also observed in the work of LeBlanc and Ferreira [6]. Referencing back to the Campbell diagram produced by LeBlanc and Ferreira [10] shown in Figure 3.12c, it becomes clear that when the turbine rotational speed is located between 100 and 175 RPM the 2P, 3P and 4P motions are affected by structural flexibility motions; this RPM range

coincides with the TSR range of 2.5 to 3.5. These structural motions are caused due to flapping motions of the struts which cause heaving motions on the primary blades and ricking of the tower. The latter will have considerable effects on turbine thrust measurements but also the torque measurements due to the harmonic frequencies of the turbine structure.

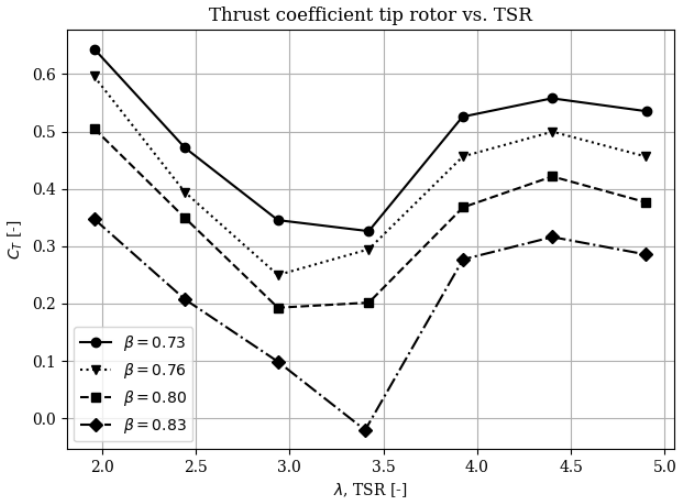


Figure 3.23: Tip rotor thrust coefficient versus the tip speed ratio. Data for across all actuator mesh disk cases is binned per tip-speed ratio

Additionally, for the higher tip-speed ratios of 4.5 and 5.0, there are also structural uncertainties. Again referring to Figure 3.12c it is evident that the $TSR = 4.5$ which runs at 227 RPM cases see bouncing motions of the base platform affecting the second-period motions of the rotor. For $TSR = 5.0$, the turbine is operating at 255 RPM which see the first-period motions are also affected by the flapping motions of the struts.

Further uncertainties are also considered namely dynamic stall, the presence of dynamic stall is expected to occur at lower tip-speed ratios/Reynolds numbers. This phenomenon will shed further uncertainty on the results for the actuator mesh disk performance since it will cause periodic fluctuations in the measured torque which in turn will affect the final result of the actuator mesh disk thrust coefficient. Note, that that the value for the thrust coefficient measured at $\lambda = 3.5$ for a $\beta = 0.83$ has been omitted. This result is an obvious experimental error due to suggesting that the actuator mesh disk is thrusting, which is non-physical. Due to the aforementioned experimental uncertainties that are the result of structural motions and dynamic stall, only data collected for tip-speed ratios equal to 4.0 will be used to determine the actuator mesh disk performance.

The induction field of the static PTV cases with actuator mesh disks will be presented. This data is acquired by measuring the flow field in the wake of the actuator mesh disk; this data is static in the sense that the primary turbine was fixed during this part of the experiment thus not rotating. The rotor induction (shown in Equation (3.20)) is a function of the freestream velocity and the in the wake of the rotor, it is a description of the velocity deficit in the flow due to the presence of the rotor. The induction can also be used to infer the thrust coefficient of the rotor, as seen in Equation (3.21).

$$2a = 1 - \frac{V_w}{V_\infty} \tag{3.20}$$

$$C_T = 4a(1-a) \tag{3.21}$$

Displayed in Figure 3.24 are the induction fields measured in the wake of each actuator mesh disk for each porosity at a grid size of 15x15. The coarseness of the grid resolution is a limitation of the PTV system and its low particle density; in order to improve the grid resolution more data is collected and averaged over the acquisition time. On a qualitative level, the induction distribution in the wake is consistent with the

expectations for the wakefield with induction peaks located at the core of the wake. The induction distribution decreases radially away from the peak until it becomes zero at the boundary between the wake and freestream flow. Moreover, the wake of the primary rotor wake is also present in the induction fields, particularly in Figure 3.24a and Figure 3.24b where the contour lines become more concentrated and tapered above the location of peak induction. Additionally, the distribution of the induction field, and by extension, the wake, shows asymmetry, particularly where the wake of the primary blade interacts with the wake of the actuator mesh disk. In Figure 3.24 one can discern a "pinching" of the induction distribution in the vicinity of the coordinates: $[-0.4; 1.0]$. This is likely the result of an experimental error where the angle of attack of the primary blade was not zero, this will cause rotation in the wake and produce the asymmetry observed in the measurements. Between the tests the angle of attack was kept the same, thus the error is systematic across all the data.

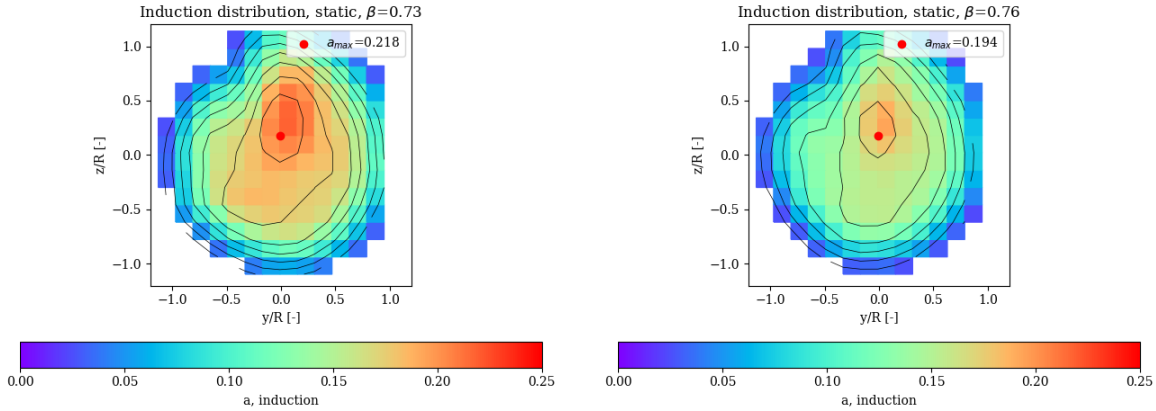


(a) Actuator mesh disk induction field, $\beta = 0.73$




(b) Actuator mesh disk induction field, $\beta = 0.76$

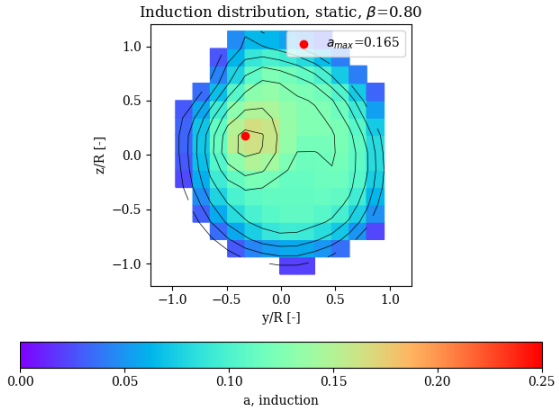


(c) Actuator mesh disk induction field, $\beta = 0.80$

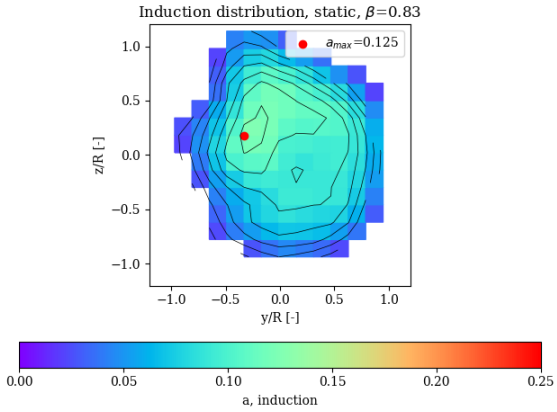


(d) Actuator mesh disk induction field, $\beta = 0.83$

Figure 3.24: Induction field for each actuator mesh disk measured statically (non-rotating turbine) at zero angle of attack and at a freestream velocity of $V_\infty = 4.0$ m/s. The induction fields are measured in the wake of the actuator mesh disk at a distance of 2 rotor diameters

The data presented in Figure 3.25 shows the relation between the actuator mesh disk thrust coefficient and the porosity of the actuator mesh disk. Four different sources of data are used and include torque data from the PitchVAWT at $TSR = 4.0$, W-tunnel test results, induction field data from the static PTV test and an empirical model. The empirical model is also used to size the actuator mesh disks and can be retrieved from the data presented by Ming et al. [7].

A large disparity is observed between the PitchVAWT data (determined from the turbine torque) and the other data sets. It appears to yield a higher estimation of the thrust coefficient, this is likely the result of a key assumption that is made when determining the actuator mesh disk thrust coefficient. The thrust of the actuator mesh disk is determined by measuring the difference in torque observed between the turbine in its clean configuration and when the turbine is mounted with the tip rotors, this is shown by Equation (3.14). However, this assumes the torque of the primary blades in both the clean case and the case with actuator

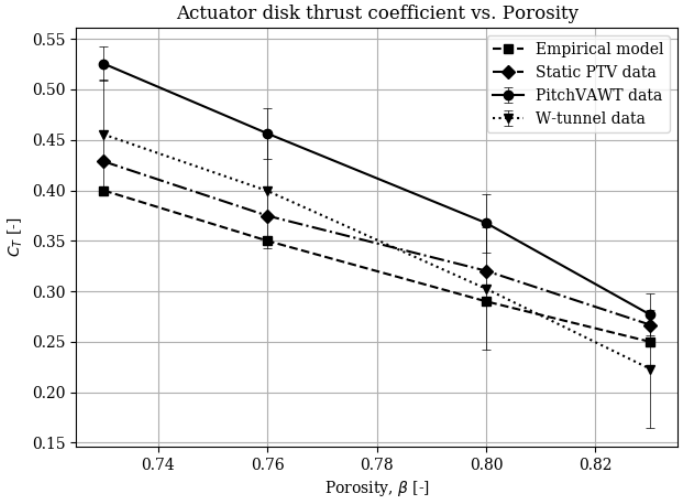


Figure 3.25: Tip actuator mesh disk thrust coefficient compared to results of the W-tunnel test and empirical results obtained from Ming et al. [7]. The PitchVAWT data set is an average across all the tip-speed ratios measured. The pitchVAWT data has an average standard deviation of $\bar{\sigma_P} = 0.046$ and the average standard deviation for the W-tunnel data is $\bar{\sigma_W} = 0.058$

mesh disks is the same. This is likely untrue since the wake of the actuator mesh disks will reduce the primary blade loading and thus the torque. Therefore, the primary blades will produce less torque with the actuator mesh disks mounted to the blade tips, thus Equation (3.14) will overestimate the added torque due to the actuator mesh disks which leads to an overestimation of the thrust coefficient.

Another key difference is observed in the slope gradient between both the pitchVAWT/W-tunnel data and the empirical model/static PTV data; each pair shows similarities in thrust coefficient sensitivity w.r.t porosity, however, they are distinct from the other pair. A key difference between the aforementioned data pairs is how the data is acquired. For the PitchVAWT data and the W-tunnel data; the thrust coefficient is inferred from the turbine torque or bending moments acting on the turbine shaft. The empirical data presented by Ming et al. [7] is comprised of measurements conducted by Yu et al. [53] and Lignarolo et al. [54], in these studies the thrust coefficient is determined from the velocity deficit in the wake. Likewise, the static PTV data also derives the thrust from the rotor wake induction field. As such, the differences observed in thrust coefficient sensitivity w.r.t the porosity in Figure 3.25 can be influenced by the differences in the measurement techniques.

When looking at the PitchVAWT data and the W-tunnel data the results of the disparity between them exceeds one standard deviation; a large contributor to this deviation is the aforementioned overestimation of primary blade torque. Furthermore, the PTV test yielded a higher average thrust coefficient than the empirical model whilst using similar measurement techniques. These results seem to suggest that the actuator mesh disks yield higher thrust coefficients when mounted on the PitchVAWT, i.e they are present in an unsteady rotational flow. For the PTV data obtained from the PitchVAWT, the increased thrust coefficient is likely the result of the actuator mesh disk wake and primary blade wake mixing and thus exacerbating the velocity deficit observed in the wake. As mentioned previously, the primary blade wake is observed in the induction distributions shown in Figure 3.24.

### 3.4.3. Tip Vortex Interactions

The scale of the PTV experiment and the quantity of the available data lend themselves to a turbine-scale analysis of the flow field around the blade tip region. Information regarding the setup of the PTV test can be found in Section 3.1.5 and Section 3.1.6; post-processing of this data is described in Section 3.2.5. The PTV data presented in this section will predominantly be discussed in a qualitative sense as relates to the previously presented results for both the blade loading in addition to the performance of the actuator mesh disks.

The measurement domain captures the trajectory of the blade within 90° of its rotation from $-45° < \theta < 45°$.

The domain, shown in Figure 3.26 for the clean case and the actuator mesh disk case ($\beta = 0.80$), has been normalised with the blade chord length, $\bar{c}$. The origin of this domain is the LE of the blade tip when the blade is located at an azimuth position of $\theta = 0°$ (the junction between the upwind and downwind rotor halves).

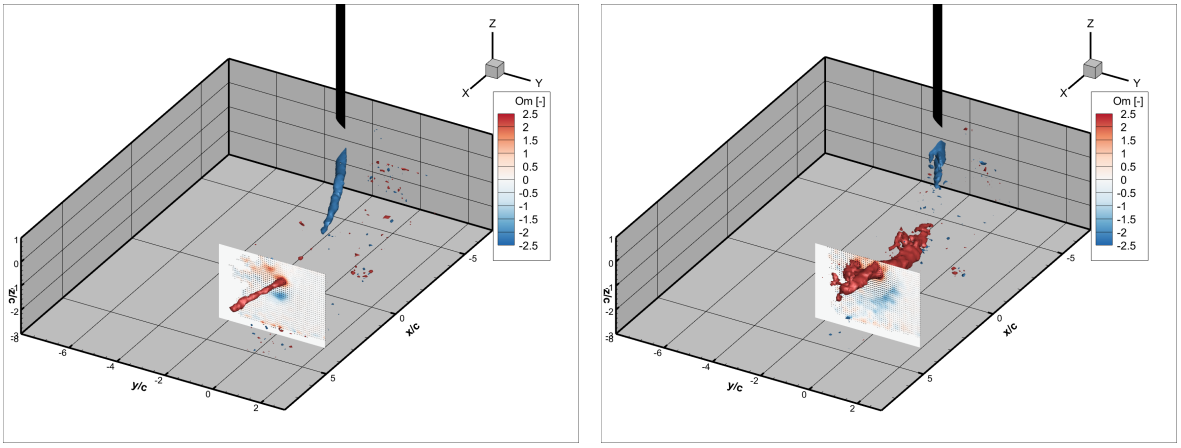


(a) Blade tip vortex of the turbine in clean configuration. Three vortices can be identified: 1) the negative vortex shed by the blade in the frame upwind, 2) the positive vortex produced by the blade in the frame downwind and 3) the negative vortex shed upwind by the second blade

(b) Blade tip vortex of the turbine with mesh disks mounted, $\beta = 0.80$. Two vortices can be identified: 1) the negative vortex produced by the blade in frame upwind and 2) the positive vortex produced by the blade in frame downwind

Figure 3.26: Isometric views of the blade tip vortex captured through the PTV process. Isosurfaces are plotted for $\omega = 2.2$ [-] and $\omega = -2.2$ [-], the images also include the turbine blade geometry (shown in black). Both sets of data are captured for a TSR=4.0 and an azimuthal angle of $\theta = 45°$

An isometric view of the vorticity (about the x-axis) generated by the rotor blade is provided by Figure 3.26. Note, the vorticity presented in this text is non-dimensional through the normalisation w.r.t freestream velocity and the blade chord length. The isosurfaces shown in each sub-figure distinguish vorticities of magnitudes: $\omega = 2.2$ [-] and $\omega = -2.2$ [-]; this means that rotation of the vortices plotted in Figure 3.26 are counter to each other. Looking at one can distinguish three different vortices. 1) nearest to the blade in the region of $0 < x/c < 5$ negative vorticity is generated due to the lift being generated on the inboard part of the blade; this is consistent with the theory and the results of the blade loading shown in Figure 3.18 which show positive normal forces in the upwind region. 2) positive vorticity is observed in the wake region of $-5 < x/c < 0$, this vorticity was generated some time steps earlier and the orientation is once again consistent with the blade loads expected in the downwind region. 3) the last vortex that can be distinguished is one of negative vorticity and is in close proximity to the second vortex. The third vortex is the result of the second blade tip vortex that is generated upwind before it moves downstream where it encounters the vortex of the first blade.

In Figure 3.27b one can see the vorticity generated by the rotor blades when equipped with the actuator mesh disk. In contrast to Figure 3.27a, one can no longer observe the third vortex generated by the second rotor blade. Instead one can only observe the two blade tip vortices. The fact that the third vortex is not present in the case with the actuator mesh disk does have consequences for the blade tip vortex, this can be observed when one takes a slice in the wakefield at the location shown in Figure 3.26. A two-dimensional plot of the vorticity field is shown in Figure 3.27 at a slice located a distance of $x/c = 4.2$ measured from the blade LE when it is at $\theta = 0°$. In Figure 3.27a one can readily identify the two counter-rotating vortices, in Figure 3.27b one can only observe the positive rotating blade tip vortex. Some further differences between the clean case and the actuator mesh disk case are the size and position of the positive-rotating blade tip vortex. The actuator mesh disk case shows a larger tip vortex being produced with its vorticity expanding more into the wake. There are two reasons for the larger vorticity in the actuator mesh disk case, the first is that the mesh of the actuator mesh disk is shedding small vortices that mix with the blade tip vortex causing it to expand more in the wake. The second reason is the lack of the counter-rotating vortex that is present in the clean case. Since the two vortices are counter-rotating, they work to weaken one another and thus diminish their relative vorticity strength. Another key difference between the two cases is the location of (positive) blade tip vortex: for the clean case, the vortex core is located around $z/c \approx -0.13$ whereas, for the case with the actuator mesh disk, the vortex core is located at $z/c \approx 0.38$. In the clean case, the tip vortex appears to move downwards away from the blade, for the actuator mesh disk case the tip rotor vortex

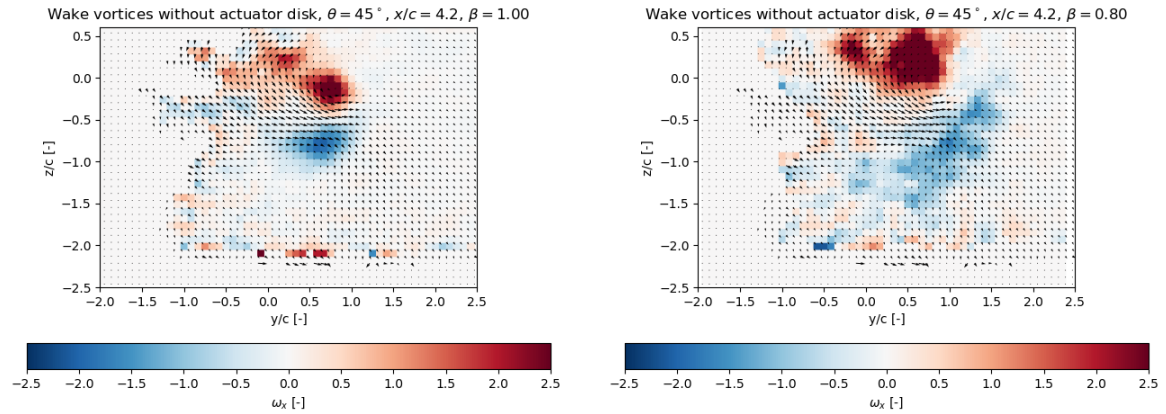


(a) Vorticity component about the x-axis in the wake of the blade without an actuator disk

(b) Vorticity component about the x-axis in the wake of the blade with an actuator disk ($\beta = 0.80$)

Figure 3.27: Vector fields captured at $x/c = 4.2$ at $\theta = 45^\circ$ and TSR=4.0, the slice is shown in Figure 3.26. The contours indicate vorticity about the x-axis ($\omega_x$) normalised w.r.t the freestream velocity and the blade chord

appears to move upwards.

An observation made in the wake of the actuator mesh disk case is the formation of vortex rings. These vortex rings are observed by evaluating the $\omega_{yz}$ which is the vector product of both $\omega_y$ and $\omega_z$, this results in the pattern observed in Figure 3.28. The formation of these ring-like patterns is characteristic of the vortex field in the wake of the actuator mesh disk and is part of a greater shroud of vortices that roll up, this has also been described in the work by van Kuik [55]. The observed vortex ring structure is indicative of a symmetric induction field and thus can more easily be observed at small angles of attack.

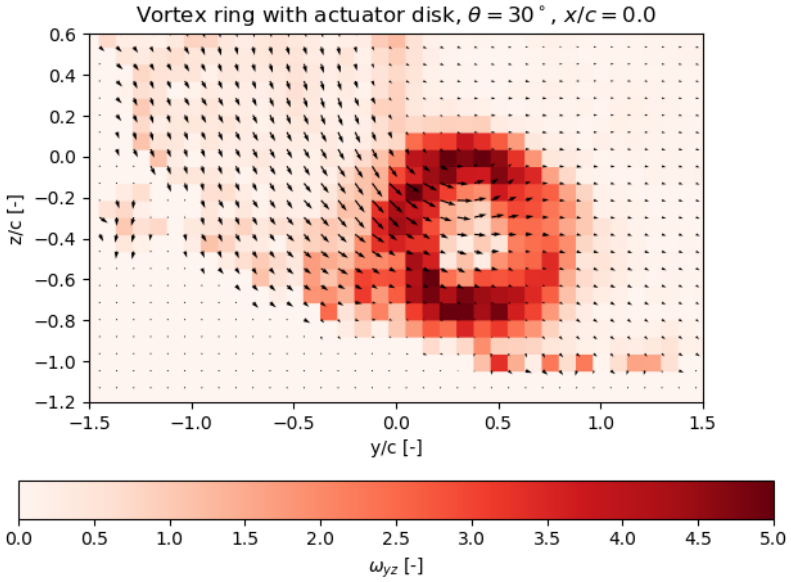


Figure 3.28: Vortex ring observed in the wake of the blade tip with actuator mesh disk, TSR=4.0

### 3.4.4. Reverse Flow

So far the wake of the blade tip has been discussed in relation to the vorticity generated and the mutual interaction between the upwind and downwind vortices. However, observations can also be made about the velocity field in the wake of the actuator mesh disks.

In Figure 3.29 the velocity field is shown in the wake of the actuator mesh disk mid-plane at the azimuthal position of $\theta = 15^\circ$ such as the wake is captured from two chord lengths aft of the turbine blade. It can be observed across all cases that the presence of the actuator mesh disk produces a wake that in the reference frame of the turbine, yields reverse flow which is not the case for the turbine without actuator mesh disks. This is evident when comparing the actuator disk cases to the clean case in Figure 3.29a. Furthermore, the magnitude of the flow reversal appears to increase with decreasing porosity, thus increasing with thrust coefficient, this is evident by evaluating the mean flow in the wake as can be seen in Figure 3.30.

In Figure 3.30, the reverse flow velocities are averaged over on a plane orthogonal to the x-axis at a distance of $x/c = 2.3$ from the actuator mesh disk. This seemingly arbitrary $x/c$ location is chosen such that the number of data points is maximised whilst also being sufficiently close to the actuator mesh disk. The contour plot reveals a region of reverse flow (in blue) along the rotational path of the turbine blade. These results for the velocity field are overall consistent with expectations for the velocity in the wake, where one would expect to see a velocity deficit due to the drag produced by the actuator mesh disks; furthermore, the velocity deficit appears to increase with decreasing porosity (increasing thrust). From Figure 3.25 it was found that the thrust coefficient scales linearly with the actuator mesh disk porosity, thus theoretically, the velocity in the wake should scale quadratically with the actuator mesh disk porosity. However, the quadratic scaling of the wake velocity is not easily discerned from Figure 3.30, an explanation as to why this is the case is provided. The qualm with the data resides in the case for $\beta = 0.83$ shown in Figure 3.29e, there the wake velocity deficit is expected to be higher (more negative) according to the quadratic nature of the scaling. However, recalling from Figure 3.25 it was observed in the pitchVAWT data that the $\beta = 0.83$ actuator showed non-linear behaviour which deviated from previous cases; this resulted in a lower than expected result for the thrust coefficient. This lower thrust coefficient is consistent with the lower-than-expected velocity deficit in the wake. This may be due to some experimental error, or an error in the actuator mesh disk model which alters the porosity; regardless, the result appears consistent throughout the data.

The reverse flow observed in Figure 3.30 has implications for the wake/vortices produced by the blade tip and actuator mesh disk. As a result of the flow reversal, the actuator mesh disk wake appears to linger for a longer duration allowing it to persist until the second blade enters this phase angle, this is evident in Figure 3.31 which shows the blade at $\theta = -35^\circ$ slightly before it intersects the wake of the upwind blade. In Figure 3.31a the clean blade is shown entering the region $-35^\circ < \theta < 35^\circ$, ahead of the downwind blade one can see a large velocity deficit in the flowfield. When comparing the clean case in Figure 3.31a to the actuator disk case in Figure 3.31b, it is evident that the velocity deficit ahead of the downwind blade is significantly greater due to the lingering wake observed in the wake of the actuator wake. This is a departure from the BVI observed for the turbine without the tip rotors since the BVI is no longer caused by the upwind shed vortex convecting downstream. This also aligns with the observations in Figure 3.27 where the upwind (negative) vortex is absent from the wakefield. In contrast to the BVI observed in the clean turbine case, the vortex that causes BVI in the actuator mesh disk case appears to linger at a higher position, closer to the path of the blade thus being impactful on the blade/actuator mesh disk performance.

Although the regions investigated are limited, the areas of flow reversal appear to coincide with the rotational path of the blades. Flow reversal may be present for other azimuthal positions, this becomes increasingly more likely when the thrust coefficient of the actuator mesh disk is higher since the magnitude of the flow reversal becomes greater. This will need to be investigated in future works.

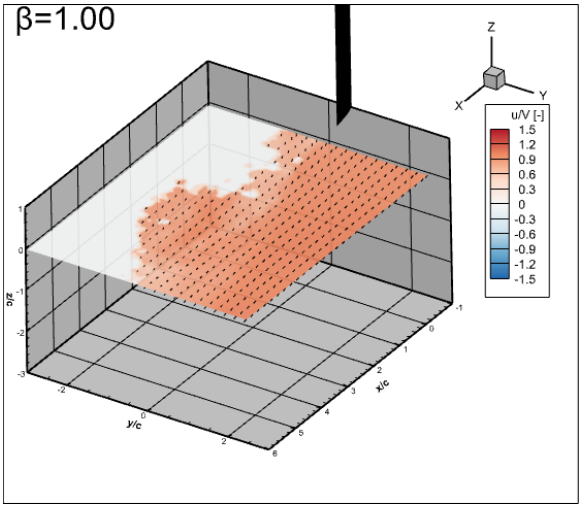


(a) Actuator mesh disk velocity field, $\beta = 1.00$ (clean case)

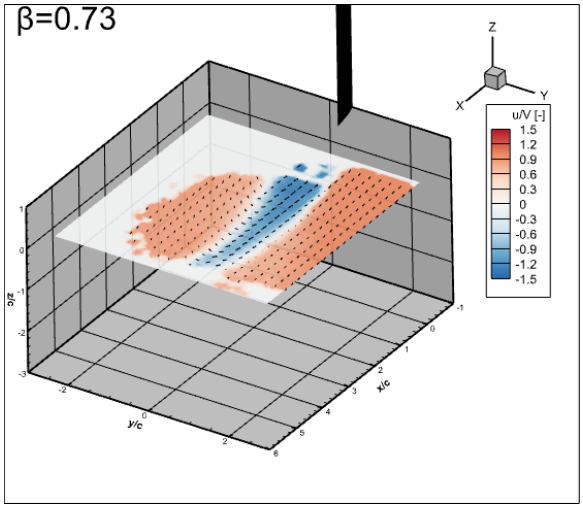


(b) Actuator mesh disk velocity field, $\beta = 0.73$

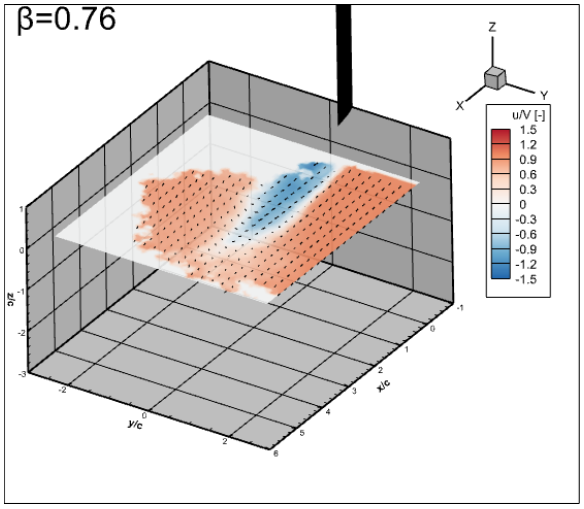


(c) Actuator mesh disk velocity field, $\beta = 0.76$

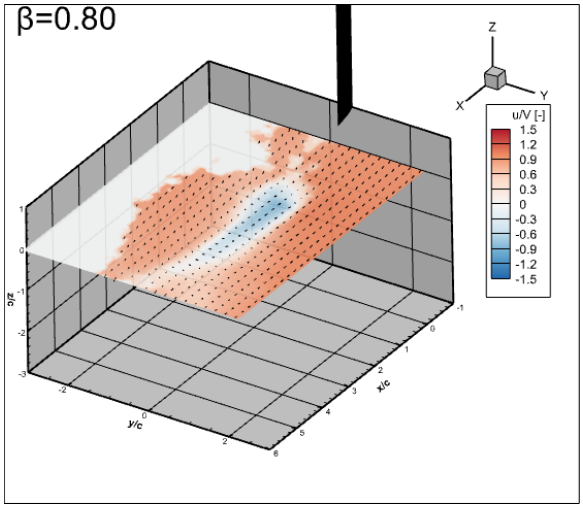


(d) Actuator mesh disk velocity field, $\beta = 0.80$

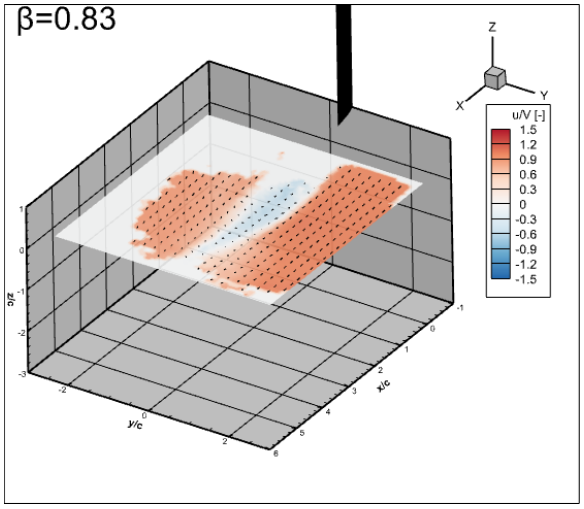


(e) Actuator mesh disk velocity field, $\beta = 0.83$

Figure 3.29: The velocity field at the actuator mesh disk mid-plane ($z/c = 0$) that shows the reverse flow in the wake of the actuator mesh disk. All the velocity fields are shown at $\theta = 15°$ with $V_\infty = 4.0$ m/s

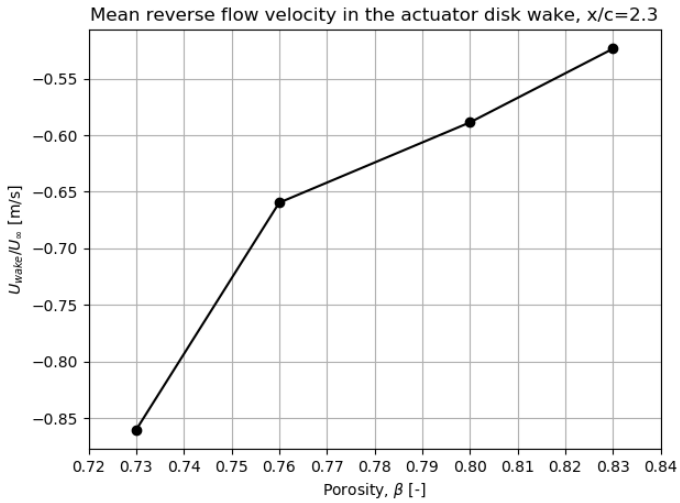


Figure 3.30: The mean reverse velocity in the wake of the actuator mesh disk mid-plane at $\theta = 15°$ with $V_\infty = 4.0$ m/s

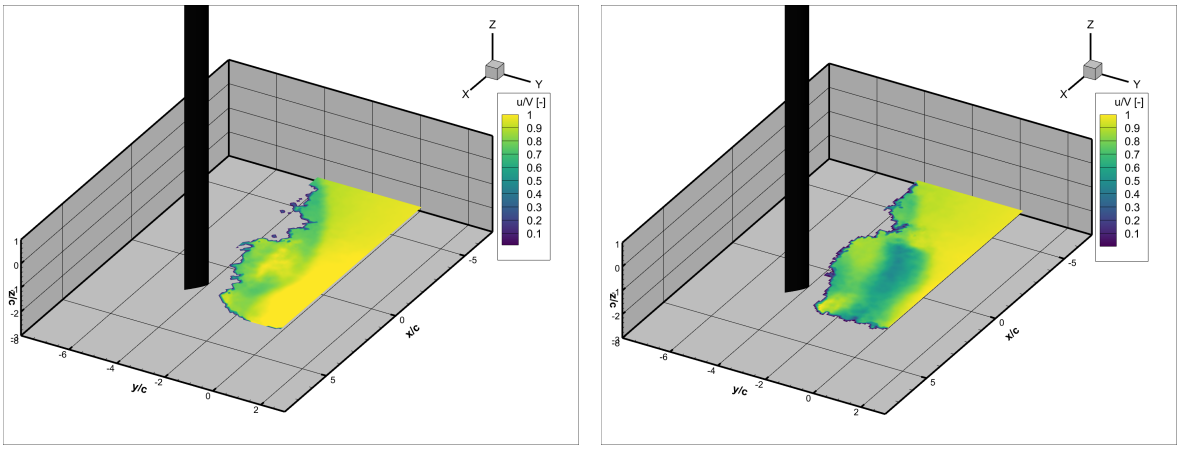


(a) Velocity component in the x-direction for the blade without an actuator disk

(b) Velocity component in the x-direction for the blade with an actuator disk ($\beta = 0.80$)

Figure 3.31: Velocity fields captured at $z/c = 0.0$ at $\theta = -35°$ and TSR=4. The contours indicate the magnitude of the velocity component in the x-direction relative to the freestream velocity ($u/V_\infty$), this velocity field is projected onto a plane at the tip of the blade. This figure shows the degree of the velocity deficit in the wake when BVI occurs

# 4

# NUMERICAL SIMULATION

This chapter of the thesis is dedicated to the proposed numerical vortex model. The implementation of the tip rotor geometries will be presented in addition to the overall functionality of the model. Furthermore, the stability of the numerical model will be assessed by means of an independence study that will determine both grid and temporal convergence. The results of the numerical model will be compared to the experimental results, additionally, data will be presented to demonstrate the capabilities and potential of the numerical model.

## 4.1. CACTUS NUMERICAL MODEL

This section will discuss the CACTUS numerical model: how it functions and to what extent it is used for numerical simulation in the present work. CACTUS (Code for Axial and Cross-flow TUrbine Simulation) is a numerical vortex model capable of estimating turbine performance, this includes vertical-axis wind turbines. The software has been developed at Sandia National Laboratories (SNL) at the Department of Energy and is built on the VDART3 software developed at Texas Tech by Strickland et al. [56]. A summary of the CACTUS numerical model is provided with much of the information being retrieved from the work of Murray and Barone [57]. Moreover, computations are carried out using clusters available at the Delft High-Performance Computing Centre (DHPC) [58].

The CACTUS model is capable of simulating the fluid flow about an arbitrary geometry that consists of several blade elements. Each blade element can be defined by its span, root- and tip chord and by its twist angle. For each blade element, CACTUS returns a load coefficient that is derived from the local flow conditions in combination with airfoil polar data this is then outputted in the form of a local (two-dimensional) lift- and drag coefficient. The local blade loads are based on a local blade-oriented coordinate system and can be combined for each element to describe the total turbine performance. The numerical model computes the blade element loads in time based on the number of time steps per rotor revolution. The simulation concludes when the revolution-averaged power coefficient of the turbine converges within predefined criteria.

The velocity field of the CACTUS numerical model is described using a potential flow model in combination with a free (or fixed) vortex lattice system which defines the wakefield, this system is shown schematically in Figure 4.1. This system applies the Kutta-Joukowski theorem [29] to determine the relation between the strength of the bound vortex ($\Gamma_B$) to the lift coefficient of each blade element at each time step. Expressions using the bound vorticity of each blade element for the lift coefficient are shown in Equation (4.1); here $s$ is the distance along the spanwise direction.

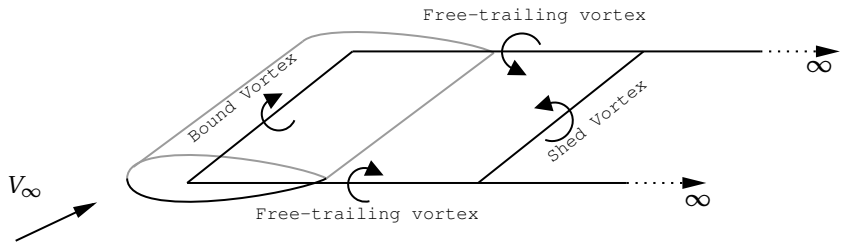


Figure 4.1: Blade element geometry with its vortex lattice system consisting of bound, trailing and shed vortices

$$C_L = \frac{2}{V_\infty S_{elem}} \int \Gamma_B(s)\, ds \tag{4.1}$$

After each time step, the system is updated based on the inflow conditions and the temporal changes to the bound vortex causing a vortex to be shed into the wake. By applying the conservation of vorticity along a vortex line as stipulated by the Helmholtz theorem retrieved from Katz and Plotkin [29], the trailing vorticity ($\Gamma_T$) and the shed vorticity ($\Gamma_S$) can be determined thus yielding a description of the wakefield. From conservation, the trailing vortices are the result of changes in the spanwise bound vorticity as shown by Equation (4.2). Furthermore, the shed vorticity is the result of changes in the bound vorticity in time as shown by . In these equations, $s$ denotes the spanwise location.

$$\Gamma_T(s,t) = \Gamma_B(s,t) - \Gamma_B(s-ds,t) \tag{4.2}$$

$$\Gamma_S(s,t) = \Gamma_B(s,t-dt) - \Gamma_B(s,t) \tag{4.3}$$

According to Kelvin's Theorem, the circulation is constant about a closed contour that moves with the fluid; mathematically this means $\frac{D\gamma}{Dt} = 0$. The vortex model is built up by a continuously advecting lattice structure that maintains the conservation of circulation; the velocity at which the wake advects is dictated by the local flow velocity.

The velocity field can be described using the Biot-Savart law which stipulates that the velocity at any point is comprised of the circulation strengths of each vortex line in the wake lattice system. This is shown in Equation (4.4) where the resulting velocity vector $\vec{V}$ is described by the sum of $N_{vor}$ induced velocity component by each vortex element $i$ with vector endpoints $\vec{r_{i,1}}$ and $\vec{r_{i,2}}$ with circulation strength $\Gamma_i$.

$$\vec{V} = \sum_{i}^{N_{vor}} \frac{\Gamma_i}{4\pi} \frac{\vec{r_{i,1}} \times \vec{r_{i,2}}}{\left|\vec{r_{i,1}} \times \vec{r_{i,2}}\right|^2} \left(\vec{r_{i,1}} - \vec{r_{i,2}}\right) \cdot \left(\frac{\vec{r_{i,1}}}{\left|\vec{r_{i,1}}\right|} - \frac{\vec{r_{i,2}}}{\left|\vec{r_{i,2}}\right|}\right) \tag{4.4}$$

The aerodynamic loads on each blade element at any time $t$ can be derived from the local velocity and the vorticity. The numerical model iterates through time, at each time step the blade loads are computed which subsequently informs the velocity field through the vortex lattice system, the local flow parameter can then be used to predict the blade loads for the next time steps. From Murray and Barone [57] it is stated that the CACTUS solver advances the solution in time through a second-order predictor scheme which applies the midpoint rule to predict the solution at time $t + \frac{dt}{2}$.

### 4.1.1. Dynamic Blade Loading

The aerodynamic blade loads for a VAWT are inherently unsteady due to the periodic behaviour of the blades, thus the CACTUS numerical model must be able to estimate higher-order dynamic blade loads. To understand this one must realise that when the blades are rotating, the blades are effectively pitching. This pitching behaviour means that the rate of change of angle of attack, $\dot{\alpha}$ is non-zero and thus each blade section experiences a temporally changing circulation/blade load. In CACTUS, the effects of airfoil pitching motions are computed at the ½ chord location whilst the Kutta condition is satisfied at the ¾ chord location. The latter then becomes the location where the local lift coefficient is defined. In this way, CACTUS derives the normal and tangential forces at ½ chord from the drag at ½ chord location and the local lift at the ¾ chord location.

$$C_N = C_{D,5}\sin(\alpha_5) + \left(C_{L,75} + \pi\dot{\alpha}\right)\cos(\alpha_5) \tag{4.5}$$

$$C_T = -C_{D,5}\cos(\alpha_5) + C_{L,75}\sin(\alpha_5) + C_{T,\dot{\alpha}}(\dot{\alpha_5}) \tag{4.6}$$

$$C_{T,\dot{\alpha}} = \frac{C_{L,5}}{2}\frac{\dot{\alpha}\bar{c}}{2V_{rel}} \tag{4.7}$$

In Equation (4.5) and Equation (4.6) the relations used by CACTUS are shown these are used to determine normal and tangential force coefficients respectively. Note the additional lifting component in Equation (4.5), $\pi\dot{\alpha}$, this term is a result of the numerically "massless" blade being accelerated due to the pitching motion. Similarly, the added force in the tangential direction due to the pitching of the blade is shown in Equation (4.7).

The CACTUS model also contains functionality to handle transient dynamic stall effects on the blade elements. Although not explored in the present work, the models available are briefly listed here and include the Boeing-Vertol empirical correlation model [35] and the Leishman-Beddoes model [36].

### 4.1.2. Turbine Geometry

The turbine geometry used in the CACTUS model is generated using a MATLAB script which is based on a script provided by SNL. The geometry of the turbine consists of several blade elements equal to $N_{elem}$, these blade elements comprise the lifting line elements of the system. Additionally, strut geometries can also be implemented, however, the influence of the struts will be omitted at this time. The turbine geometry file consists of parameters that define each blade element's start and end point at $t = 0$; subsequent locations of the turbine geometry are handled by CACTUS.

Each blade element consists of a local coordinate system placed at a 1/4 chord that defines the normal- and tangential directions. The direction of the normal vector defines the sign of the angle of attack at that blade element, with positive angles of attack being defined by a positive relative velocity component in the normal direction.

The implementation of the tip rotors in the CACTUS geometry is shown in Figure 4.2. The primary rotor blades are sized using the PitchVAWT used in the experimental campaign, thus featuring the NACA0021 airfoil. The scale of the tip rotors is defined as 6% of the primary rotor radius, thus the radius becomes $R_{tip} = 0.047m$. The number of tip rotor blades is derived from preliminary designs for the X-rotor concept which at the time of writing this feature 5-bladed tip rotors. The chord of the tip rotor blades is $\bar{c}_{tip} = 0.0047m$, moreover, there is no spanwise twisting of the tip rotor blades. It should be noted that the tip rotor geometry is not optimised for this turbine concept, this is beyond the scope of this project, thus the implementation of the tip rotors presented here functions merely as a proof of concept.

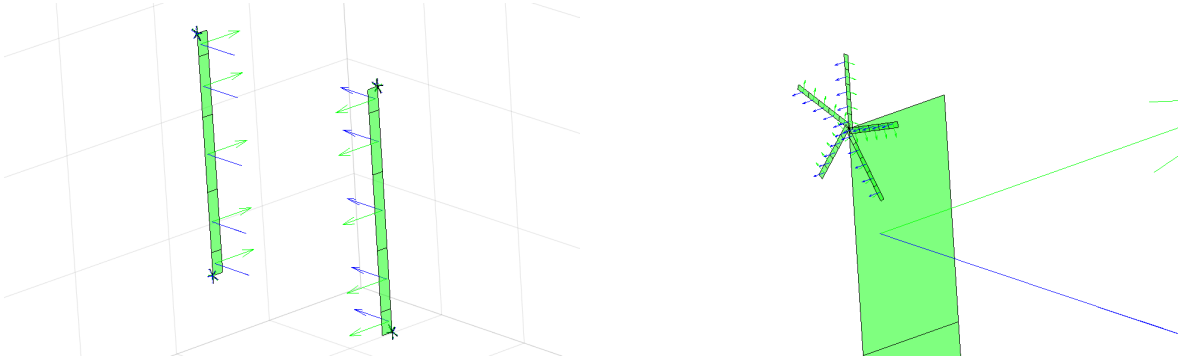

(a) Isometric view of the CACTUS geometry

(b) Isometric view of the CACTUS tip rotor geometry

Figure 4.2: Views of the turbine geometry used within CACTUS for $N_{elem} = 5$ for each blade (including tip rotor blades). The elements on the primary blades are defined according to a cosine distribution whereas the tip rotor elements are distributed linearly

The CACTUS numerical model utilises a global variable for the number of blade elements ($N_{elem}$) which applies to all blades. Additionally, due to the scale of the tip rotor and its high rotational speed which is 50 times greater than the primary rotor, the timescale is much smaller when compared to the primary rotor. To adequately resolve the solution of the tip rotors a sufficiently high number of time steps must be chosen whilst a reasonable computation time is maintained. Based on these requirements, a time step of 900 is

chosen this means that between every time step, the tip rotor rotates approximately 20°.

### 4.1.3. Airfoils and Polars

A key input variable for the CACTUS numerical model is airfoil polars that define the relationship between the angle of attack and the aerodynamic coefficients of lift and drag. In the case of the PitchVAWT with tip rotors, two airfoils can be distinguished: the NACA0021 for the primary rotor blades and the FFA-W3-241 airfoil for the tip rotor blades. The polar data is retrieved using the XFOIL suite within QBlade; there the polars are extended for higher angles of attack using the Viterna method described by Viterna and Janetzke [59]. This is necessary due to the blades experiencing large angles of attack at low tip-speed ratios.

The lift and drag polars used are shown in Figure 4.3. The Reynolds numbers are chosen such that they are as close to the conditions experienced during the experimental campaign whilst maintaining a sufficient degree of accuracy/reliability. The experiments were conducted at a Reynolds number of $\approx 8.0 \cdot 10^4$, however, airfoil polars from XFOIL become unreliable at such low Reynolds numbers. To improve the reliability of the numerical model it is chosen to use airfoil polars at $Re = 1.5 \cdot 10^5$. This highlights a key limitation of the model, that being the accuracy of the aerodynamic polars. This inaccuracy is particularly concerning for tip rotors due to the relatively small chord length which reduces the local Reynolds number to $Re = \approx 1.5 \cdot 10^4$. This highlights an avenue for potential further research where relevant airfoil polar data is obtained experimentally.

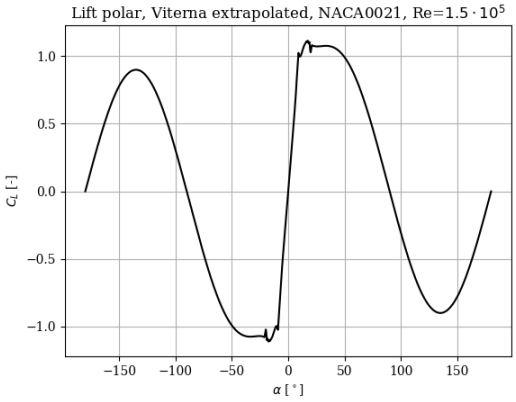


(a) The extrapolated lift polar for the NACA0021 airfoil

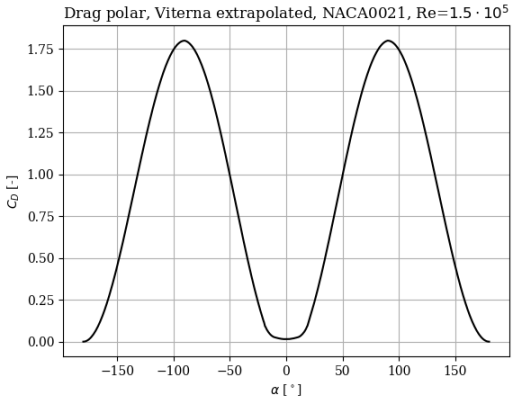


(b) The extrapolated drag polar for the NACA0021 airfoil

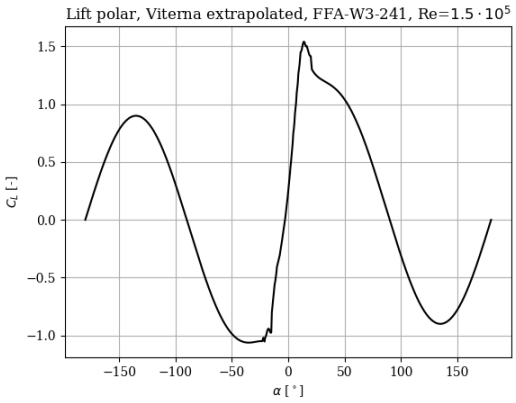


(c) The extrapolated lift polar for the FFA-W3-241 airfoil

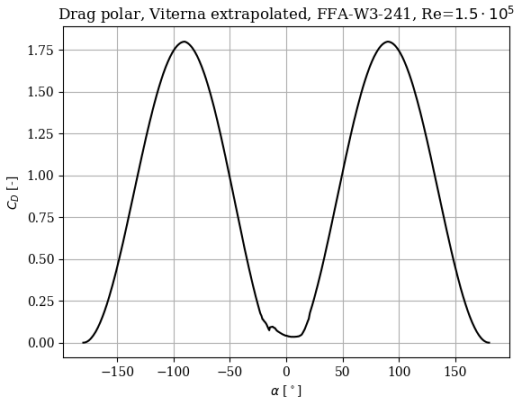


(d) The extrapolated drag polar for the FFA-W3-241 airfoil

Figure 4.3: The lift and drag polars used for the airfoil geometries. The NACA0021 airfoil is used for the primary rotor blades and the FFA-W3-241 airfoil is for the secondary rotor blades

### 4.1.4. TIP ROTOR IMPLEMENTATION

This section will provide an overview of the implementation of the tip rotors in CACTUS; a full description is provided in Appendix B. Most changes apply to the turbine geometry file and the case input file. In regards to the geometry, a definition of the location and direction of the tip rotor rotational axis is provided. This in combination with the rotational speed of the tip rotor allows for the numerical model to determine the position of the tip rotor blade elements at each time step. The procedure of rotating the tip rotors is simply added to the time-progressing routine of CACTUS and ensures that all the tip rotor elements are accounted for such that the blade geometry is updated at each time step.

Additional changes are made to CACTUS subroutines that determine the blade loading on the tip rotor blade elements based on the local flow properties. A key amendment is the contribution of the rotational velocity of the tip rotor to the tangential velocity component on the blade elements. Finally, the contribution of the tip rotor torque to the total torque is estimated using the normal forces on the tip rotor blade elements in combination with its distance to the turbine centre.

Computation of the local angle of attack is calculated using pre-existing functions which equate the XYZ components of the flow vector, these functions are present in the CACTUS software. Using the existing functions in combination with the additional tip rotor geometry parameters allows for a numerical description of the tip rotor flow field and blade loading.

## 4.2. Independence Study

In this section, an independence study for CACTUS and the pitchVAWT geometry will be provided based on both the spatial and temporal grids. To that end, this section aims to provide insight into the numerical sensitivity of the numerical model. Of particular interest, is the spatial grid sensitivity, because the tip rotor numerical model is operated at relatively low grid resolutions. The independence study is carried out for the highest tip-speed ratio tested since this case will be limiting in terms of final convergence.

In Figure 4.4 the convergence behaviour is shown of the numerical model as a function of the grid refinement (i.e the number of blade elements $N_{elem}$). This study is conducted using the pitchVAWT geometry in a clean configuration. In Figure 4.4a the final solution for the power coefficient is plotted against the number of blade elements, this shows that between the lowest and highest grid resolutions, there is a difference in $\approx$ 18% of the final solution. The final solution varies $\approx$ 8% when the number of elements increases from 5 to 10 per blade. In terms of thrust coefficient, Figure 4.4c appears to initially converge more rapidly based on the number of grid elements, however, the variance between the coarsest and finest grid is smaller with only an $\approx$ 8% deviation. Moreover, Figure 4.4b and Figure 4.4d show the convergence rate for both the power- and thrust coefficient based on the grid refinement. Interestingly, the convergence appears to oscillate after $N_{elem} = 30$ with the difference in solution increasing at $N_{elem} = 35$ before decreasing again. The limit of 15 revolutions is likely too few for geometries with a grid size that exceeds $N_{elem} = 30$.

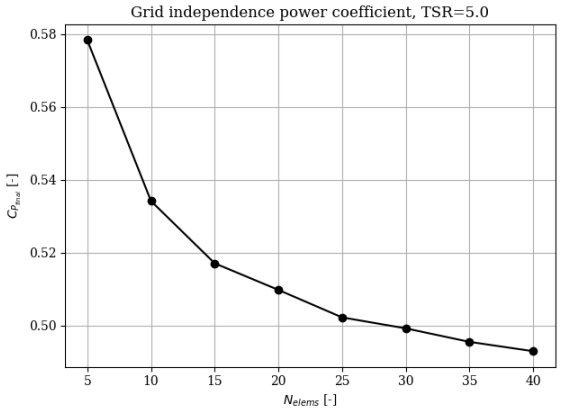


(a) Grid convergence on a linear scale, shown is the final solution for the power coefficient

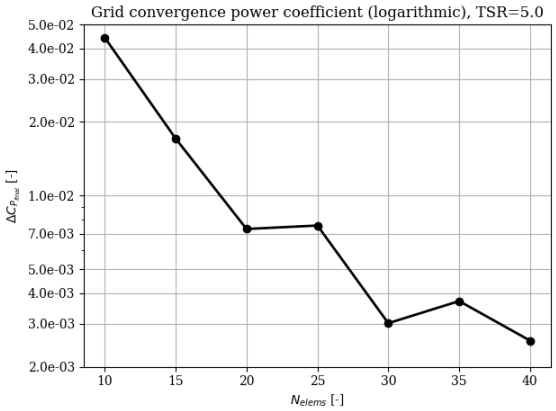


(b) Grid convergence on a log scale, each value represents the deviation with the previous grid resolution for the power coefficient

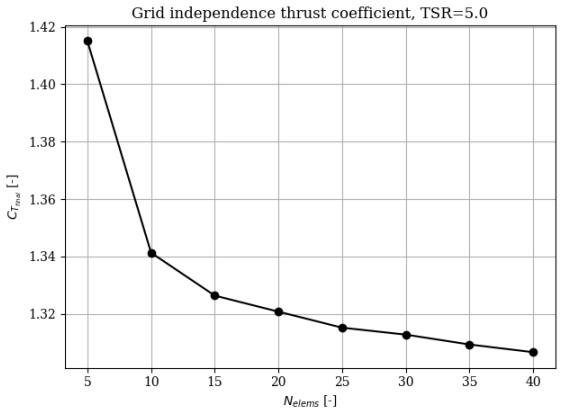


(c) Grid convergence on a linear scale, shown is the final solution for the thrust coefficient

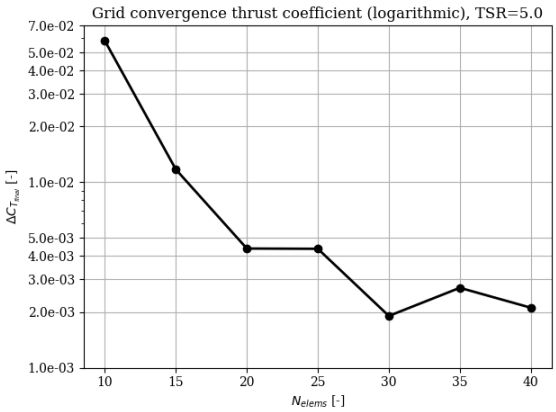


(d) Grid convergence on a log scale, each value represents the deviation with the previous grid resolution for the thrust coefficient

Figure 4.4: Grid convergence for the pitchVAWT in the clean configuration at TSR=5.0 and $N_{ti} = 900$. Each simulation is terminated after 15 revolutions thus the respective wakes are developed to an equal extent

Temporal grid convergence is also analysed for the pitchVAWT in its clean configuration, the results are shown in Figure 4.5. Since the numerical model with the tip rotors requires small time steps, the sensitivity of the final solution must be evaluated; the temporal sensitivity is tested with 5 blade elements. For both the power- and thrust coefficient, initial convergence is large before slowing down. Crucially, for $N_{ti} = 900$

the solution appears to diverge for the geometry test. This means that the model is not temporally stable; however, this is likely the result of the coarse spatial grid being insufficient to resolve the small time scales. The relatively low number of blade elements and the high number of time steps causes the wake points to be highly skewed which results in numerical instabilities.

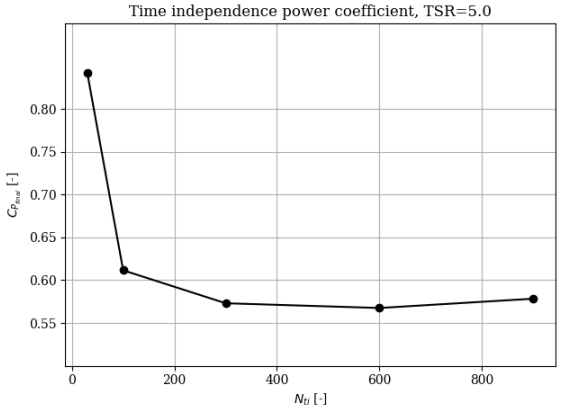


(a) Time convergence on a linear scale, shown is the final solution for the power coefficient

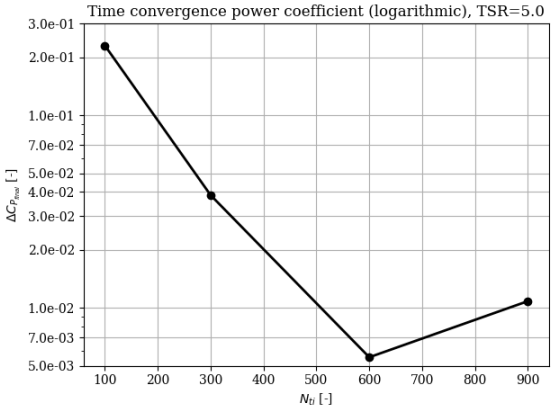


(b) Time convergence on a log scale, each value represents the deviation with the previous temporal grid for the power coefficient

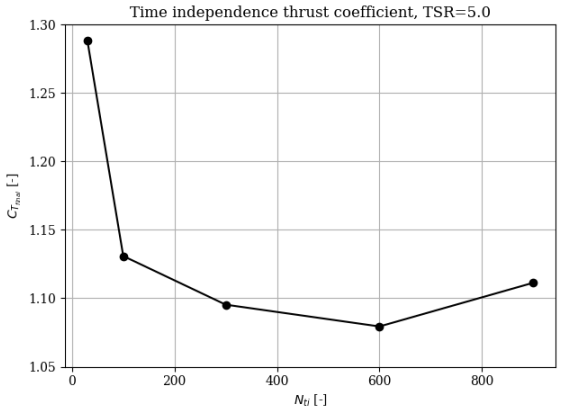


(c) Time convergence on a linear scale, shown is the final solution for the thrust coefficient

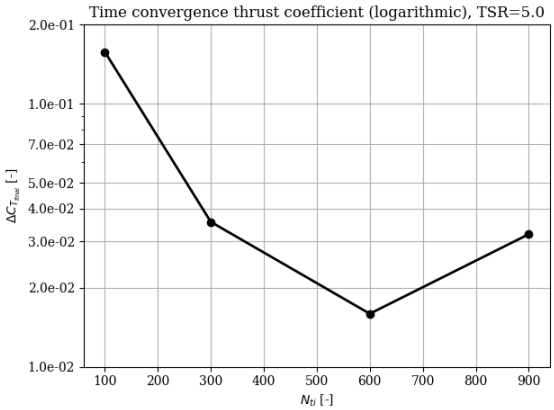


(d) Time convergence on a log scale, each value represents the deviation with the previous temporal grid for the thrust coefficient

Figure 4.5: Time convergence for the pitchVAWT in the clean configuration at TSR=5.0 and $N_{elem} = 5$. Each simulation is terminated after 15 revolutions thus the respective wakes are developed to an equal extent

## 4.3. Numerical Model Validation

This section will discuss the validity of the CACTUS results through comparison with the data collected during the experimental campaign outlined in Chapter 3. In addition, results will be presented with the CACTUS tip rotor model in which the tip rotor performance will be assessed and compared to the experimental data.

### 4.3.1. PitchVAWT in Clean Configuration

The pitchVAWT in its clean configuration will be assessed first. The nature of the experimental data acquisition means that analysing the turbine performance based on the power coefficient is not possible since the "output" torque is measured by the amount of torque delivered by the motor. As such, when comparing the experimental model to the numerical model (in the clean configuration) the assessment will exclusively consist of turbine force distributions. For the experimental campaign, this means that the load cell data will be used; this data has been verified based on repeatability as detailed in Section 3.3.2. Additionally, the numerical model will consist of 5 blade elements per blade since this is also the number of blade elements to be used in the tip rotor model.

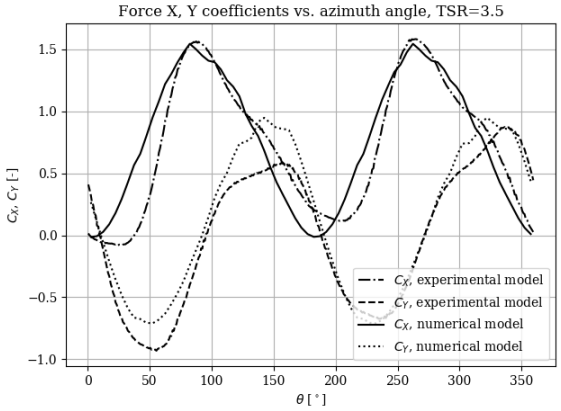


(a) Force coefficients in the x- and y-direction compared, TSR=3.5

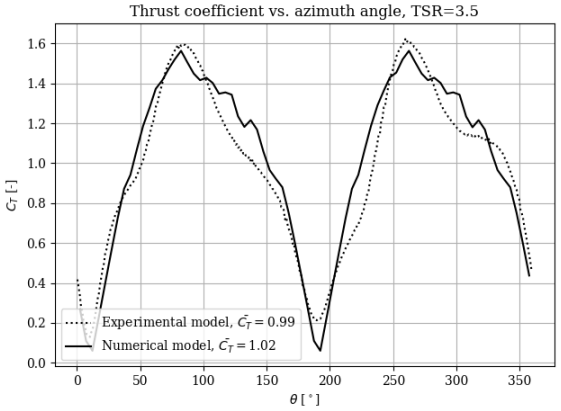


(b) Thrust coefficients compared, TSR=3.5

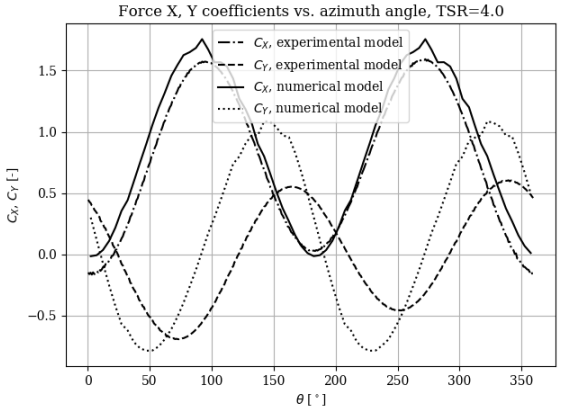


(c) Force coefficients in the x- and y-direction compared, TSR=4.0

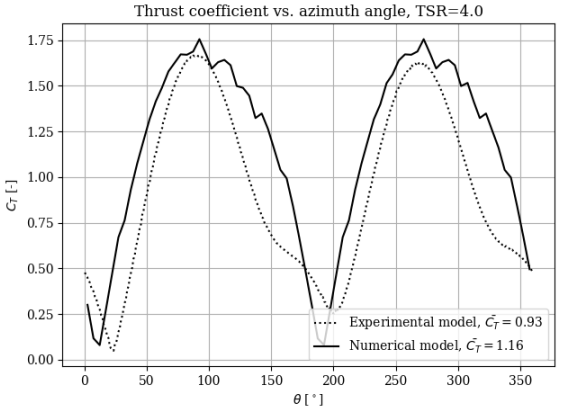


(d) Thrust coefficients compared, TSR=4.0

Figure 4.6: Comparison of the x- and y-force coefficients and the turbine thrust coefficient for experimental results and the CACTUS numerical model using a fixed wake. Data is shown for TSR=3.5 and TSR=4.0 using the (clean configuration) pitchVAWT geometry and all data is binned within 5° azimuth. The CACTUS numerical model uses $N_{elem} = 5$, $N_{ti} = 900$ and is terminated after 15 revolutions. No dynamic stall models are used in the CACTUS numerical model

The force distribution in the x- and y-direction for the CACTUS numerical model are compared to the data from the experimental model in Figure 4.6a. Data is compared for a tip-speed ratio of 3.5 with the numerical model completing 15 revolutions with the data retrieved from the final revolution. When looking at the force coefficient in the x-direction, $C_X$, the peak force coefficient behaviour appears to be similar between

the two models. The location of the local maximum $C_X$ appears to be consistent between the two models, however, there are differences observed around the local minima; this is most evident around $\theta = 0°$ and $\theta = 180°$ where the experimental model achieves higher $C_X$ values than the numerical model. It is possible that this discrepancy is due to a phase shift in either model, therefore the value of the experimental model appears to lag behind. Moreover, the forces in the y-direction are slightly higher for the numerical model, however, for the TSR=3.5 case, it is likely that these discrepancies are due to experimental errors. The numerical model is perfectly symmetric, whereas the experimental model shows variations between the forces on blade 1 and blade 2; this is most evident in the distribution of $C_Y$. Of the two blades, when blade 2 is upwind the result for $C_Y$ appears consistent with the numerical model. In Figure 4.6b the resulting thrust coefficient at TSR=3.5 is plotted, here the numerical and experimental models show high similarity. However, the numerical model does not exhibit the thrust "recovery" seen in the experimental model which appears as an inflexion point in the ranges $120° < \theta < 160°$ and $300° < \theta < 350°$.

When looking at the higher tip-speed ratio of 4.0 in Figure 4.6c, similar observations can be made yet overall the numerical results yield higher force coefficients than the experimental model. One can observe that the phase shift in $C_X$ between the numerical- and experimental models is no longer present. However, the results for the force distribution in y-direction for TSR=4.0 appear more dissimilar with the numerical model attaining significantly higher peak values, additionally, there appears to be a 30° phase shift of the $C_Y$ peaks between the numerical and experimental models. The dissimilarities in the $C_Y$ results also yield deviations when looking at the thrust coefficient shown in Figure 4.6d, this is most evident in the ranges $100° < \theta < 180°$ and $280° < \theta < 360°$ where the numerical model returns a significantly higher thrust coefficient. Overall for the tip-speed ratio of 4.0 cases, the numerical and experimental models show less cohesion.

The results between the numerical and experimental models presented in Figure 4.6 show the rotor force distributions, it appears to suggest that the two models scale the forces in similarly based on the tip-speed ratio. The key difference between the models is the azimuthal distribution of $C_Y$, which as mentioned before, results in the discrepancies observed for the thrust coefficient (mostly for TSR=4.0). Based on the comparison of the thrust coefficient, one can expect similar behaviour to apply other performance parameters such as the power coefficient. It is repeated that the results for the numerical model shown in Figure 4.6 used the coarsest grid investigated, thus based on the findings in Section 4.2, it is expected that for higher resolution models the final numerical solution will be lower, which may yield more favourable results for TSR=4.0. Moreover, the numerical model did not feature any dynamic stall models and fixes the wake element velocity after the first time step; these simplifications of the physics will further introduce numerical uncertainties and thus require further research.

### 4.3.2. Tip Rotor Model

Results of the pitchVAWT with tip rotors implemented in CACTUS are presented in this section. The data that is presented will be assessed in order to evaluate the tip rotor implementation in CACTUS.

In Figure 4.7, the turbine torque and power coefficient are plotted against the tip-speed ratio (of the primary rotor) for both the pitchVAWT in the clean configuration, in addition, the pitchVAWT with tip rotors. Now that these performance parameters are equated for the primary rotor, thus the torque/power generated at the primary rotor shaft. The results show that the effect of the tip rotors reduces the effectiveness of turbine torque and power which is to be expected due to the drag introduced to the total turbine system. Also, Figure 4.7a suggest that in addition to a large decrease in torque coefficient, the tip-speed ratio at which the peak torque coefficient is achieved shifts from TSR=3.0 to 3.5 <TSR< 4.0. When comparing the resulting power coefficients in Figure 4.7b, the tip rotor case appears to have a larger detrimental effect at TSR=5.0 thus ensuring a power coefficient peak at TSR=4.5; this is contrary to the clean case where the power coefficient appears to plateau for TSR>3.5

Another observation is that the tip rotor is not optimised (as expected) to extract all the power generated by the primary rotor. For this optimisation to be realised one would expect that the power coefficient of the pitchVAWT with tip rotors will become zero.

The results of the numerical model also allow for estimating the flow conditions at the tip rotor and quantifying the performance of the tip rotors. The results in Figure 4.8a show the angle of attack at the tip rotor blades as a function of the azimuthal position of the primary rotor blade. The distribution observed is ex-

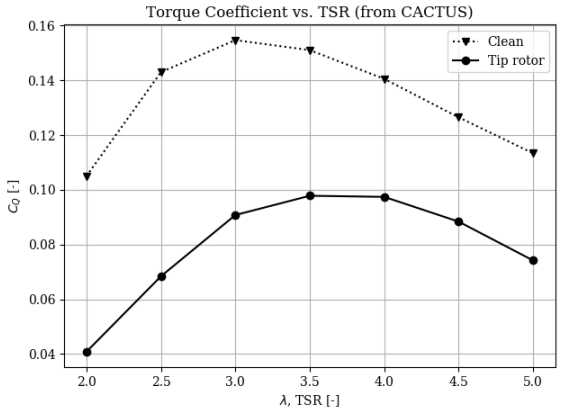


(a) Torque coefficient versus the tip-speed ratio for the clean case and tip rotor case, obtained from CACTUS

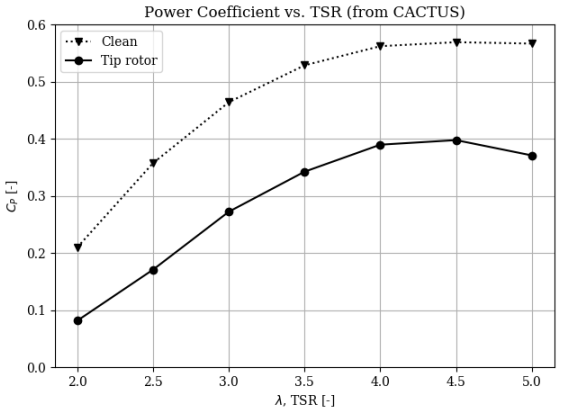


(b) Power coefficient versus the tip-speed ratio for the clean case and tip rotor case, obtained from CACTUS

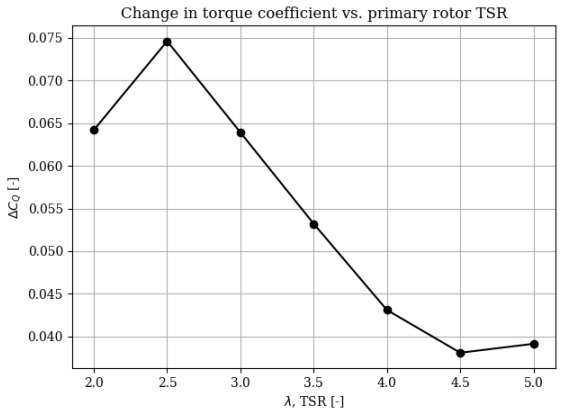


(c) Relative change in the turbine torque coefficient

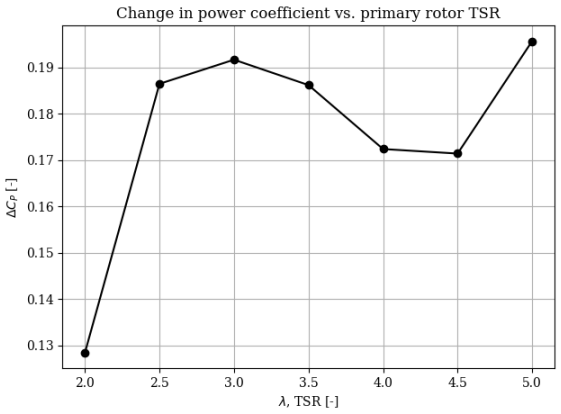


(d) Relative change in the turbine power coefficient

Figure 4.7: A comparison of the turbine torque and power- coefficient of the pitchVAWT model in clean configuration and the pitchVAWT with four tip rotors (one at each blade tip). Additionally, the change in turbine performance between the pitchVAWT in clean configuration and with tip rotors is also plotted. All the data that is presented is collected after 15 revolutions with 900-time steps per revolution

pected to vary depending on the tip-speed ratio, this is because both the primary and secondary are rotating at a constant rate therefore the incoming flow at the tip rotor is reduced to a ratio between the tip-speed ratio of the primary and secondary rotors. The maximum angle of attack is realised at $\theta = 0°$, this makes this azimuthal position most critical in terms of the stall conditions of the airfoil, the cases with the lowest tip-speed ratio suffer the most from this. All tip-speed ratio cases appear to have reduced thrust performance around the area of maximum angle of attack since the airfoil polar enters the stall region. The peak lift performance of the FA-W3-241 airfoil is realised at around $\alpha = 14°$, in the model tested this angle of attack is only reached when the tip rotor is moving downwind. Thus for the TSR=4.0 and TSR=5.0 cases, the peak thrust performance is reached at an azimuth position of $\theta = 180°$. Looking at Figure 4.8b it is apparent that for the cases TSR=2.0 and TSR=3.0 the minimum angle of attack becomes too low when the tip rotor moves downstream, this results in a significant drop in thrust performance at $\theta = 180°$. This means that the tip rotor must be optimised for both the upwind and downwind moving situations.

Insights into the tip rotor performance such as those provided in Figure 4.8, allow for optimising the tip rotor geometry based on the azimuthal position of the primary blade. When looking at the tip rotor performance as a function of the tip-speed ratio of the primary rotor, the effects of the tip-speed ratio can be seen in Figure 4.9. Here the performance parameters at lower tip-speed ratios suffer from a combination of the stall and a too-low minimum angle of attack; these factors are highlighted by the lack of tip rotor optimisation. Regardless, such optimisations are beyond the scope of the present work and will need to be investigated further, however, these results provide an indication of what is possible using this low-fidelity numerical model. It should be noted that due to the vast differences between the numerical tip rotor model and the porous actuator disk model, it is not possible to directly compare the results between the two models.

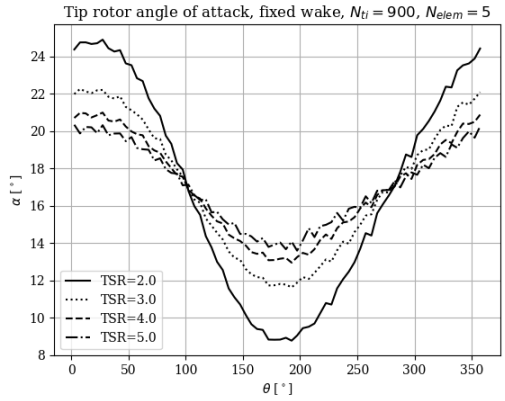


(a) The local angle of attack for tip rotor blades

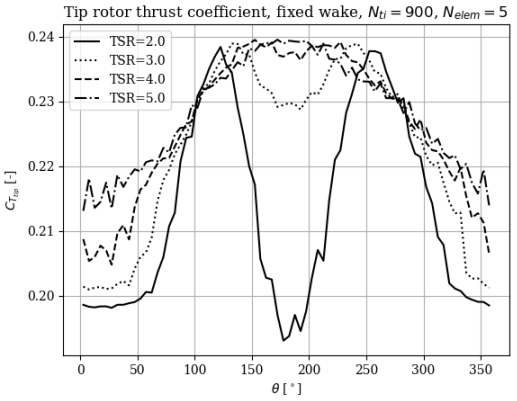


(b) The tip rotor thrust coefficient

Figure 4.8: The angle of attack and thrust coefficient on one of the tip rotor blades as a function of the primary turbine azimuthal position. The data is binned per 5° azimuth and does not employ any dynamic stall model

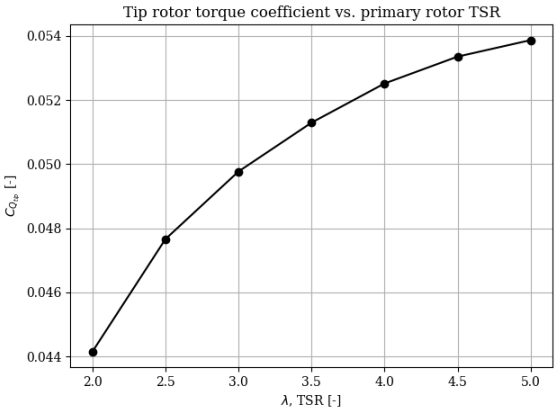


(a) Tip rotor torque coefficient

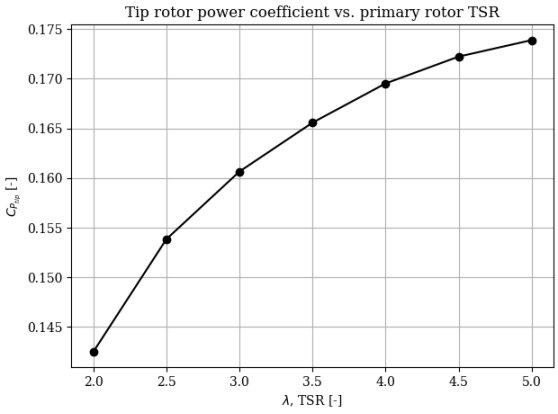


(b) Tip rotor power coefficient

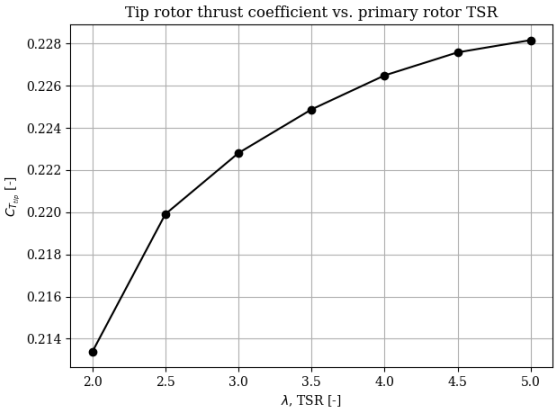


(c) Tip rotor thrust coefficient

Figure 4.9: The tip rotor performance as a function of the primary rotor tip-speed ratio. All the data that is presented is collected after 15 revolutions with 900-time steps per revolution and 5 elements per blade

# 5

# CONCLUSIONS AND RECOMMENDATIONS

In the work presented, the impact of secondary tip rotor geometries in combination with a conventional VAWT layout has been investigated on both an experimental and numerical basis. Experimentation utilises the PitchVAWT developed by LeBlanc and Ferreira [11] at the TU Delft, to quantify the effects of actuator mesh disks mounted at the blade tips. The impact on the primary turbine performance parameters such as torque and thrust are analysed concerning the actuator mesh disk geometry. Additionally, the thrust performance of the actuator mesh disk is also investigated and compared with auxiliary data. Further effects of the actuator mesh disk are quantified through the use of PTV which allows for measuring the fluid domain around the actuator mesh disk and in its wake. This allows visualising the flow field around the actuator mesh disk within 90° of its rotation from $-45° < \theta < 45°$, this highlights the interaction between the blade tip vortex and the wake of the actuator mesh disk.

To further the numerical capabilities of the novel secondary tip rotor VAWT concept, the pre-existing CACTUS vortex model developed at Sandia National Laboratories (SNL) at the Department of Energy, has been expanded to allow for the integration of more complex tip rotor geometries. The aim is to propose a means for inexpensive numerical estimation of tip rotor VAWT concepts, to that end the present work outlines the capabilities of the numerical model and highlights its advantages and drawbacks.

## 5.1. CONCLUSIONS

Experimentation with the PitchVAWT was conducted in the Open Jet Facility at TU Delft and was carried out using a free stream velocity of $V_\infty = 4.0$, this yielded an average Reynolds number of $Re = 7.5 \cdot 10^4$. The instrumentation on the pitchVAWT allowed for determining the normal force distribution on the turbine blades through the use of strain gauges mounted on the blade struts. Testing showed that the presence of actuator mesh disks appeared to have a reductive effect on the blade normal forces, this effect appeared throughout all azimuth angles but was most evident in the upwind half of the rotor. Variations in the thrust direction were observed between the cases with actuator mesh disks and those without, these were estimated to be 3.7°, however, it did not appear that the normal forces were responsible for the change in thrust direction observed. Instead, the changes in the tangential blade forces are likely driving the thrust vector more leeward due to the actuator mesh disks.

The thrust performance was determined using load cells at the turbine base, these measurement devices yielded a description of the turbine forces in the Cartesian directions. It was observed that increases in the forces along the free stream direction (x-direction) were increased as a result of the actuator mesh disks which in turn resulted in a slight increase in the thrust coefficient. However, these results also revealed that the turbine blade was not loaded equally which resulted in an asymmetric loading distribution for the thrust. Additionally, when assessing the porosity of the actuator mesh disk, it was found that higher porosities returned higher primary turbine thrust coefficients which are consistent with the reduction in blade normal forces mentioned previously.

The actuator mesh disks were originally sized for the thrust coefficient using empirical data obtained from Yu et al. [53] and Lignarolo et al. [54], with the available torque data from the experiment it was possible to determine the thrust coefficient and subsequently validate the empirical model. A methodology for determining the actuator mesh disk thrust coefficient as a secondary tip rotor device is proposed. Moreover, the static PTV test allowed for determining the induction field of the actuator mesh disk in the wake. These results were compared to the empirical model and auxiliary data obtained from the actuator mesh disks in a separate wind tunnel test. Overall the results are consistent between the different data sets, they show

an inverse proportionality between the actuator mesh disk porosity and the thrust coefficient. The results of the PitchVAWT experiment do show a significant discrepancy between the thrust determined from the torque and the thrust determined from the wake induction; the uncertainties of each measurement technique were discussed and are the subject of future research.

The domain investigated using PTV revealed changes to the blade tip vortex which had consequences for BVI, tests were conducted at TSR=4.0. A key difference between the turbine with an actuator mesh disk and the turbine without (clean case) was the absence of the upwind shed vortex (shed from the other blade). In the clean case, the interaction between the upwind shed vortex and the blade tip vortex was destructive, cancelling one another and forcing the pair out of the blade path. However, the wake of the blade with the actuator disk appears to not show the upwind/blade tip vortex pair witnessed in the clean case. As a result, the wake of the actuator mesh disk lingers in the blade path until it is intercepted by the second blade thus suggesting that the blade wakes are more impactful on the blade performance. The observation of the lingering actuator mesh disk wake was further supported by the flow reversal witnessed in the wake; the degree of flow reversal (barring experimental uncertainties) also seemed consistent with the theory for the velocity deficit in the wake. A key limitation of the actuator mesh disk model as a replacement for a rotor is that the wake of the actuator mesh disk does exhibit any rotation, instead, its wake appears to expand the blade tip vortex whereas a counter-rotating tip vortex will have a destructive effect on the blade tip vortex.

A numerical vortex model is proposed that expands the capabilities of CACTUS allowing for the implementation of tip rotor geometries on conventional VAWTs. The CACTUS model is validated with the acquired data for the pitchVAWT in its clean configuration; the numerical model generally yields a higher result for the thrust coefficient than the experiment, this result is expected as the numerical model does not account for several aerodynamic and mechanical losses such as dynamic stall and internal frictions. A large dependency on the airfoil polar is identified, and the relatively low Reynolds number of the experiment cannot be replicated with sufficient accuracy using numerically generated airfoil polars. Because of the inaccuracy for low Reynolds numbers, the comparisons between the numerical and experimental models make more sense for higher tip-speed ratios.

Results using the proposed numerical vortex model indicate that the tip rotor implementation is showing behaviour that is within expectations. The increased drag induced by the tip rotors reduces the torque and power generated by the primary turbine. Additionally, the power generated by the tip rotors appears the increase based on the primary rotor tip-speed ratio, however, increases diminish for large TSRs. The impact of the primary rotor tip-speed ratio on the performance of the tip rotors is mainly due to the changing angle of attack at the tip rotor, which for low tip-speed ratios can cause the tip rotor blades to stall. Note, that the tip rotor geometry tested is not optimised for power extraction, however, there is potential for this numerical model to be utilised as a tool for optimisation.

## 5.2. RECOMMENDATIONS

The present work leaves many avenues for future work, particularly concerning the X-rotor project. One such possibility would see the X-rotor concept tested with tip rotors. This will shed light on how the tip rotor wake is affected by the more three-dimensional wakefield (due to the primary blade downwash) of the X-rotor. This can be further extended to include tip rotor geometries instead of actuator mesh disks to measure the swirling wake and what the effects of tip rotation would entail for the blade loading.

PTV excels in capturing large amounts of volumetric data which provides aerodynamic information on a macros scale. As shown in the present work, PTV is sufficient for tracking vortical structures at the scale of the tip rotors, however, finer details such as induction fields do lack fidelity when compared to stereoscopic PIV experiments. One limitation of the present work is the phase-lock averaging of the PTV data, this requires vast amounts of data to have a satisfactory sample size ($\approx$ 100 samples). Moreover, the resolution of the PTV is limiting as particles get further away from the cameras. It is suggested that a stereoscopic PIV setup might prove more successful in capturing the planar data on the surface of the actuator mesh disk or tip rotor, this would in turn yield a more accurate description of the induction field and thus thrust/power performance. To reduce the amount of data collected, one could implement a switch that timed the rotation of the primary rotor such that data is only collected when the blades are in the correct position.

Another avenue for continued research would be to investigate the upwind tip rotor wake. As discovered in the present work, the upwind shed vortex is no longer present in the investigated domain for the tip rotor case. A follow-up study might be aimed at determining the trajectory of the upwind shed vortices and how it is affected by the large velocity deficits measured in the wake of the actuator mesh disks.

Lastly, the proposed numerical vortex model shows the capabilities for estimating the VAWTs with tip rotors and its capabilities for optimisation. However, the current algorithm lacks optimisation and due to the small time scales of the tip rotors; difficulties arise when the number of blade elements is increased. Ideally, enabling a variable number of blade elements between the primary blades and the tip rotor blades is a first step in improving the computational effort required. Moreover, the accuracy of the numerical model is highly dependent on the accuracy of the airfoil polar data, therefore subsequent research projects might aim to produce more accurate airfoil data through experimental techniques at lower Reynolds numbers.

# BIBLIOGRAPHY


[1] G. Gygax, *Advanced Dungeons & Dragons Players Handbook*, Dungeons & Dragons (TSR Hobbies, 1978).

[2] W. Leithead, A. Camciuc, A. K. Amiri, and J. Carroll, *The x-rotor offshore wind turbine concept,* Journal of Physics: Conference Series **1356**, 012031 (2019).

[3] G. Tescione, D. Ragni, C. He, C. Simão Ferreira, and G. van Bussel, *Near wake flow analysis of a vertical axis wind turbine by stereoscopic particle image velocimetry,* Renewable Energy **70**, 47 (2014), special issue on aerodynamics of offshore wind energy systems and wakes.

[4] R. WILSON and W. MCKIE, *A comparison of aerodynamic analyses for the darrieus rotor,* in *Wind Energy Conference*, https://arc.aiaa.org/doi/pdf/10.2514/6.1980-605 .

[5] TU Delft, *Open jet facility,* https://www.tudelft.nl/lr/organisatie/afdelingen/aerodynamics-wind-energy-flight-performance-and-propulsion/facilities/low-speed-wind-tunnels/open-jet-facility (2022), accessed: 03-01-2022.

[6] B. LeBlanc and C. Ferreira, *Experimental characterization of h-VAWT turbine for development of a digital twin,* Journal of Physics: Conference Series **1452**, 012057 (2020).

[7] M. Huang, C. Ferreira, A. Sciacchitano, and F. Scarano, *Wake scaling of actuator discs in different aspect ratios,* Renewable Energy **183**, 866 (2022).

[8] B. LeBlanc and C. Ferreira, *Experimental determination of thrust loading of a 2-bladed vertical axis wind turbine,* Journal of Physics: Conference Series **1037**, 022043 (2018).

[9] B. LeBlanc and C. S. Ferreira, *Overview and design of pitchvawt: Vertical axis wind turbine with active variable pitch for experimental and numerical comparison,* in *2018 Wind Energy Symposium*, https://arc.aiaa.org/doi/pdf/10.2514/6.2018-1243 .

[10] B. Leblanc and C. Ferreira, *Experimental demonstration of thrust vectoring with a vertical axis wind turbine using normal load measurements,* Journal of Physics: Conference Series **1618**, 052030 (2020).

[11] B. P. LeBlanc and C. S. Ferreira, *Experimental determination of thrust loading of a 2-bladed vertical axis wind turbine,* Journal of Physics: Conference Series **1037**, 022043 (2018).

[12] M. D. Esteban, J. J. Diez, J. S. López, and V. Negro, *Why offshore wind energy?* Renewable Energy **36**, 444 (2011).

[13] E. Dupont, R. Koppelaar, and H. Jeanmart, *Global available wind energy with physical and energy return on investment constraints,* Applied Energy **209**, 322 (2018).

[14] P. Jamieson, *Top-level rotor optimisations based on actuator disc theory,* Wind Energy Science **5**, 807 (2020).

[15] D. G. J. Marie, *Turbine having its rotating shaft transverse to the flow of the current,* (U.S. Patent 1835018A, 1931).

[16] M. Islam, D. S.-K. Ting, and A. Fartaj, *Aerodynamic models for darrieus-type straight-bladed vertical axis wind turbines,* Renewable and Sustainable Energy Reviews **12**, 1087 (2008).

[17] G. Leishman, *Principles of Helicopter Aerodynamics with CD Extra*, Cambridge aerospace series (Cambridge University Press, 2006).

[18] J. G. Leishman, *Challenges in modelling the unsteady aerodynamics of wind turbines,* Wind Energy **5**, 85 (2002), https://onlinelibrary.wiley.com/doi/pdf/10.1002/we.62 .

[19] C. Ferreira, *The near wake of the vawt: 2d and 3d views of the vawt aerodynamics,* (2009).

[20] E. Ferrer and R. H. Willden, *Blade–wake interactions in cross-flow turbines,* International Journal of Marine Energy **11**, 71 (2015).

[21] G. Bangga, G. Hutomo, R. Wiranegara, and H. Sasongko, *Numerical study on a single bladed vertical axis wind turbine under dynamic stall,* Journal of Mechanical Science and Technology **31**, 261 (2017).

[22] J. Bartl, F. Mühle, J. Schottler, L. Sætran, J. Peinke, M. Adaramola, and M. Hölling, *Wind tunnel experiments on wind turbine wakes in yaw: effects of inflow turbulence and shear,* Wind Energy Science **3**, 329 (2018).

[23] R. Howell, N. Qin, J. Edwards, and N. Durrani, *Wind tunnel and numerical study of a small vertical axis wind turbine,* Renewable Energy **35**, 412 (2010).

[24] C. Ferreira, G. Kuik, van, G. Bussel, van, and F. Scarano, *Visualization by piv of dynamic stall on a vertical axis wind turbine,* Experiments in Fluids **46**, 97 (2009).

[25] P. Wernert and D. Favier, *Considerations about the phase averaging method with application to eldv and piv measurements over pitching airfoils,* Experiments in Fluids **27**, 473 (1999).

[26] C. Jux, A. Sciacchitano, and F. Scarano, *Aerodynamics of a cycling wheel in crosswind by coaxial volumetric velocimetry,* in *14th International Symposium on Particle Image Velocimetry*, Vol. 1 (2021).

[27] D. Schanz, S. Gesemann, and A. Schröder, *Shake-the-box: Lagrangian particle tracking at high particle image densities,* Experiments in Fluids **57** (2016), 10.1007/s00348-016-2157-1.

[28] C. Jux, *Robotic volumetric particle tracking velocimetry by coaxial imaging and illumination,* (2017).

[29] J. Katz and A. Plotkin, *Low-Speed Aerodynamics*, 2nd ed., Cambridge Aerospace Series (Cambridge University Press, 2001).

[30] R. Wilson, *Wind-turbine aerodynamics,* Journal of Wind Engineering and Industrial Aerodynamics **5**, 357 (1980), wind Energy Conversion Systems.

[31] J. H. Strickland, B. T. Webster, and T. Nguyen, *A Vortex Model of the Darrieus Turbine: An Analytical and Experimental Study,* Journal of Fluids Engineering **101**, 500 (1979), https://asmedigitalcollection.asme.org/fluidsengineering/article-pdf/101/4/500/5898437/500_1.pdf .

[32] J. L. Cardona, *Flow curvature and dynamic stall simulated with an aerodynamic free-vortex model for vawt,* Wind Engineering **8**, 135 (1984).

[33] J. Murray and M. Barone, *The development of cactus : a wind and marine turbine performance simulation code.* (2011).

[34] C. Ferreira, *Rotor / wake aerodynamics lecture series (lecture notes),* (2020).

[35] R. E. Gormont, *A mathematical model of unsteady aerodynamics and radial flow for application to helicopter rotors*, Tech. Rep. (Boeing Vertol Co Philadelphia Pa, 1973).

[36] J. Leishman, T. S. Beddoes, and W. H. Ltd, *A generalised model for airfoil unsteady aerodynamic behaviour and dynamic stall using the indicial method,* (1986).

[37] L. Lignarolo, D. Ragni, C. Krishnaswami, Q. Chen, C. Simão Ferreira, and G. van Bussel, *Experimental analysis of the wake of a horizontal-axis wind-turbine model,* Renewable Energy **70**, 31 (2014), special issue on aerodynamics of offshore wind energy systems and wakes.

[38] J. Bossuyt, C. Meneveau, and J. Meyers, *Wind farm power fluctuations and spatial sampling of turbulent boundary layers,* Journal of Fluid Mechanics **823**, 329–344 (2017).

[39] S. Aubrun, S. Loyer, P. Hancock, and P. Hayden, *Wind turbine wake properties: Comparison between a non-rotating simplified wind turbine model and a rotating model,* Journal of Wind Engineering and Industrial Aerodynamics **120**, 1 (2013).

[40] S. de Jong Helvig, M. K. Vinnes, A. Segalini, N. A. Worth, and R. J. Hearst, *A comparison of lab-scale free rotating wind turbines and actuator disks,* Journal of Wind Engineering and Industrial Aerodynamics **209**, 104485 (2021).

[41] D. Schanz, S. Gesemann, and A. Schröder, *Shake-the-box: Lagrangian particle tracking at high particle image densities,* Experiments in fluids **57**, 1 (2016).

[42] J. F. G. Schneiders, F. Scarano, C. Jux, and A. Sciacchitano, *Coaxial volumetric velocimetry,* Measurement Science and Technology **29**, 065201 (2018).

[43] *Universal Robots UR5 Technical Details*, Universal Robots (2017), url: https://www.universal-robots.com/media/1514597/101081_199901_ur5_technical_details_web_a4_art03_rls_eng.pdf, accessed on 19/01/2022.

[44] P. Gerhart, A. Gerhart, and J. Hochstein, *Munson, Young and Okiishi's Fundamentals of Fluid Mechanics* (Wiley, 2016).

[45] B. Wieneke, *Volume self-calibration for 3d particle image velocimetry,* Experiments in Fluids **45**, 549 (2008).

[46] D. Schanz, S. Gesemann, A. Schröder, B. Wieneke, and M. Novara, *Non-uniform optical transfer functions in particle imaging: calibration and application to tomographic reconstruction,* Measurement Science and Technology **24**, 024009 (2012).

[47] A. Sciacchitano and F. Scarano, *Elimination of piv light reflections via a temporal high pass filter,* Measurement Science and Technology **25**, 084009 (2014).

[48] M. Novara and F. Scarano, *A particle-tracking approach for accurate material derivative measurements with tomographic piv,* Experiments in Fluids **54** (2013), 10.1007/s00348-013-1584-5.

[49] A. Rezaeiha, H. Montazeri, and B. Blocken, *Characterization of aerodynamic performance of vertical axis wind turbines: Impact of operational parameters,* Energy Conversion and Management **169**, 45 (2018).

[50] U. S. Paulsen, M. Borg, H. A. Madsen, T. F. Pedersen, J. Hattel, E. Ritchie, C. S. Ferreira, H. Svendsen, P. A. Berthelsen, and C. Smadja, *Outcomes of the deepwind conceptual design,* Energy Procedia **80**, 329 (2015), 12th Deep Sea Offshore Wind RD Conference, EERA DeepWind'2015.

[51] L. Battisti, A. Brighenti, E. Benini, and M. Castelli, *Analysis of different blade architectures on small vawt performance,* Journal of Physics: Conference Series **753**, 062009 (2016).

[52] S. Brusca, R. Lanzafame, and M. Messina, *Design of a vertical-axis wind turbine: how the aspect ratio affects the turbine's performance,* International Journal of Energy and Environmental Engineering **5**, 1 (2014).

[53] W. Yu, C. Ferreira, and G. van Kuik, *The dynamic wake of an actuator disc undergoing transient load: A numerical and experimental study,* Renewable Energy **132**, 1402 (2019).

[54] L. E. M. Lignarolo, D. Ragni, C. J. Ferreira, and G. J. W. van Bussel, *Experimental comparison of a wind-turbine and of an actuator-disc near wake,* Journal of Renewable and Sustainable Energy **8**, 023301 (2016), https://doi.org/10.1063/1.4941926 .

[55] G. van Kuik, *The Fluid Dynamic Basis for Actuator Disc and Rotor Theories: Revised Second Edition* (IOS Press, Netherlands, 2022).

[56] J. H. Strickland, T. Smith, and K. Sun, *User's manual for the vertical axis wind turbine code vdart3,* (1981).

[57] M. Barone and J. Murray, *The development of cactus, a wind and marine turbine performance simulation code,* (2011), 10.2514/6.2011-147.

[58] Delft High Performance Computing Centre (DHPC), *DelftBlue Supercomputer (Phase 1),* https://www.tudelft.nl/dhpc/ark:/44463/DelftBluePhase1 (2022).

[59] L. A. Viterna and D. C. Janetzke, *Theoretical and experimental power from large horizontal-axis wind turbines,* (1982), 10.2172/6763041.

# A

# Measurement Cases

Listed below are the measurement case test during the experimental campaign.

Table A.1: List of all the measurement series completed during the experimental campaign

| ms | TSR | RPM | $U_\infty$ | Porosity | Mounting | Note |
|---|---|---|---|---|---|---|
| 000 | 0 | 0 | 0 | Nan | OFF | Measure instrument noise |
| 001 | 0 | 0-200 | 0 | Nan | OFF | RPM vs. $F_n$ sweep |
| 002 | 0 | 0-255 | 0 | 0.73, 0.83 | BOT, TOP, ALL | Measure centripetal loads |
| 003 | 2-5 | 0-255 | 4 | Nan | OFF | TSR sweep, clean turbine |
| 005 | 2-5 | 0-255 | 4 | 0.80 | BOT | TSR sweep, bottom mounted |
| 006 | 2-5 | 0-255 | 4 | 0.83 | BOT | TSR sweep, bottom mounted |
| 007 | 2-5 | 0-255 | 4 | 0.76 | BOT | TSR sweep, bottom mounted |
| 008 | 2-5 | 0-255 | 4 | 0.73 | BOT | TSR sweep, bottom mounted |
| 010 | 2-5 | 0-255 | 4 | 0.80 | TOP | TSR sweep, top mounted |
| 011 | 2-5 | 0-255 | 4 | 0.83 | TOP | TSR sweep, top mounted |
| 012 | 2-5 | 0-255 | 4 | 0.76 | TOP | TSR sweep, top mounted |
| 013 | 2-5 | 0-255 | 4 | 0.73 | TOP | TSR sweep, top mounted |
| 015 | 2-5 | 0-255 | 4 | 0.80 | ALL | TSR sweep, top and bottom mounted |
| 016 | 2-5 | 0-255 | 4 | 0.83 | ALL | TSR sweep, top and bottom mounted |
| 017 | 2-5 | 0-255 | 4 | 0.76 | ALL | TSR sweep, top and bottom mounted |
| 018 | 2-5 | 0-255 | 4 | 0.73 | ALL | TSR sweep, top and bottom mounted |
| 020 | 2-5 | 0-255 | 4 | Nan | Nan | TSR sweep, clean turbine |
| 021 | 2-5 | 0-255 | 4 | Nan | ALL | TSR sweep, rotor sleeves |
| 022 | 4 | 204 | 4 | Nan | Nan | PTV case, clean turbine |
| 023 | 4 | 204 | 4 | 0.83 | ALL | PTV case, top and bottom mounted |
| 024 | 4 | 204 | 4 | 080 | ALL | PTV case, top and bottom mounted |
| 025 | 4 | 204 | 4 | 0.76 | ALL | PTV case, top and bottom mounted |
| 026 | 4 | 204 | 4 | 0.73 | ALL | PTV case, top and bottom mounted |
| 027 | 4 | 204 | 4 | Nan | Sleeve | PTV case, top and bottom mounted |
| 028 | 4 | 204 | 4 | Nan | Nan | PTV case, clean turbine upwind |
| 029 | 4 | 204 | 4 | 0.80 | ALL | PTV case, top and bottom mounted upwind |
| 030 | Nan | Nan | 4 | Nan | Nan | PTV static pitch sweep, clean turbine |

| | | | | | | |
|---|---|---|---|---|---|---|
| 031 | Nan | Nan | 4 | 0.83 | Nan | PTV static pitch sweep |
| 032 | Nan | Nan | 4 | 0.80 | Nan | PTV static pitch sweep |
| 033 | Nan | Nan | 4 | 0.76 | Nan | PTV static pitch sweep |
| 034 | Nan | Nan | 4 | 0.73 | Nan | PTV static pitch sweep |
| 035 | Nan | Nan | 4 | Nan | Nan | PTV static pitch sweep, rotor sleeves |

# B

# CACTUS SECONDARY ROTOR IMPLEMENTATION

Simulation of secondary (blade tip) rotors in CACTUS requires additional routines to the existing version of CACTUS. For posterity, the alterations made to the CACTUS script will be disclosed here and an explanation of the implementation of the secondary rotors will also be provided.

The module *tipvars* (shown in listing B.1) introduces new parameters necessary for describing the tip rotor geometry. Some of the variables defined in *tipvars* are provided by the case input file and thus are defined by the user. An example of the case input file is shown in listing B.5; the parameters for the tip rotor are shown in lines 36-40.

```
1  module tipvars
2
3      ! Parameters defining the secondary (tip) rotor
4
5      integer :: tiprotorflag          ! Flag for tip rotors
6      real :: rpmtip                   ! RPM of tip rotor
7      real :: tsrtip                   ! Tip-speed ratio tip rotor
8      integer :: ntip                  ! Number of tip rotors
9      integer :: nbtip                 ! Number of tip rotor blades (per tip rotor)
10     integer :: nbprimary             ! Number of primary rotors
11     real :: tiptheta                 ! Phase angle tip rotor
12
13 end module tipvars
```

Listing B.1: The *tipvars* module from tipvars.f90

```
26 &CaseInputs
27
28     jbtitle = 'PVT5_t900_TSR40'
29
30     rho      = 2.342E-3       ! 1.207 kg/m3
31     vis      = 3.776E-7       ! 18.11E-6 Ns/m2
32     tempr    = 67.46          ! 19.7 C
33     hBLRef   = 0.28215        ! 0.08600 m
34     slex     = 0
35     hAG      = 4.33399        ! 1.321 m
36
37     RPM      = 204
38     Ut   = 4                  ! Tip-speed ratio
39
40     ! Tip rotor parameters
41     tiprotorflag = 1
42     rpmtip = 10494
43     tsrtip = 3.2281
44     ntip = 4
45     nbtip = 5
46
47     ! Turbine geometry
48     GeomFilePath='../test/TestGeom/PVT5.geom'
49
50     ! Airfoil section data
51     nSect    = 1
52     AFDPath = '../test/Airfoil_Section_Data/FFA_241.dat', '../test/Airfoil_Section_Data/NACA_0021.dat'
53
54 /End
```

Listing B.2: Example case input file ('.in') with tip rotor parameters

There are also changes to the geometry files (.geom) used by CACTUS. The first change is in the order in which each rotor blade is defined. For the secondary rotor implementation, it is necessary that the primary rotor is defined, thus preceding the definition of the secondary tip rotor blades. As an example, a VAWT with 2 primary blades and 4 tip rotors each with 5 blades will see blade 1 and blade 2 as the primary blades. Blades 3 through 22 are then the tip rotor blades, these can be listed in any order as long as they are listed after the primary blades.

A second change to the geometry file is the addition of several parameters that define the location and orientation of the tip rotor rotational axis. Tip rotor blades of the same tip rotor will all share the same rotational axis, therefore these parameters only change per tip rotor group. For the primary rotor blades, these parameters are ignored however, they must be allocated an arbitrary value; an example is shown in Listing B.3.

```
Blade 3:
    NElem:    5
    FlipN:    0
    QCx:   -4.20000e-02   -4.20000e-02   -4.20000e-02   -4.20000e-02   -4.20000e-02   -4.20000e-02
    QCy:    2.00000e+00    2.01253e+00    2.02507e+00    2.03760e+00    2.05013e+00    2.06267e+00
    QCz:   -9.99201e-01   -9.99201e-01   -9.99201e-01   -9.99201e-01   -9.99201e-01   -9.99201e-01
    tx:    0.00000e+00    0.00000e+00    0.00000e+00    0.00000e+00    0.00000e+00    0.00000e+00
    ty:    0.00000e+00    0.00000e+00    0.00000e+00    0.00000e+00    0.00000e+00    0.00000e+00
    tz:    1.00000e+00    1.00000e+00    1.00000e+00    1.00000e+00    1.00000e+00    1.00000e+00
    CtoR:    4.70000e-03    4.70000e-03    4.70000e-03    4.70000e-03    4.70000e-03    4.70000e-03
    PEx:   -4.20000e-02   -4.20000e-02   -4.20000e-02   -4.20000e-02   -4.20000e-02
    PEy:    2.00627e+00    2.01880e+00    2.03133e+00    2.04387e+00    2.05640e+00
    PEz:   -9.99201e-01   -9.99201e-01   -9.99201e-01   -9.99201e-01   -9.99201e-01
    tEx:    0.00000e+00    0.00000e+00    0.00000e+00    0.00000e+00    0.00000e+00
    tEy:    0.00000e+00    0.00000e+00    0.00000e+00    0.00000e+00    0.00000e+00
    tEz:    1.00000e+00    1.00000e+00    1.00000e+00    1.00000e+00    1.00000e+00
    nEx:   -1.00000e+00   -1.00000e+00   -1.00000e+00   -1.00000e+00   -1.00000e+00
    nEy:    0.00000e+00    0.00000e+00    0.00000e+00    0.00000e+00    0.00000e+00
    nEz:    0.00000e+00    0.00000e+00    0.00000e+00    0.00000e+00    0.00000e+00
    sEx:   -0.00000e+00   -0.00000e+00   -0.00000e+00   -0.00000e+00   -0.00000e+00
    sEy:   -1.00000e+00   -1.00000e+00   -1.00000e+00   -1.00000e+00   -1.00000e+00
    sEz:   -0.00000e+00   -0.00000e+00   -0.00000e+00   -0.00000e+00   -0.00000e+00
    ECtoR:    4.70000e-03    4.70000e-03    4.70000e-03    4.70000e-03    4.70000e-03
    EAreaR:    5.89067e-05    5.89067e-05    5.89067e-05    5.89067e-05    5.89067e-05
    iSect:    1    1    1    1    1
    tax:   -1.70000e-02   -1.70000e-02   -1.70000e-02   -1.70000e-02   -1.70000e-02
    tay:    2.00000e+00    2.00000e+00    2.00000e+00    2.00000e+00    2.00000e+00
    taz:   -1.00000e+00   -1.00000e+00   -1.00000e+00   -1.00000e+00   -1.00000e+00
    tnx:    1.00000e+00    1.00000e+00    1.00000e+00    1.00000e+00    1.00000e+00
    tny:    0.00000e+00    0.00000e+00    0.00000e+00    0.00000e+00    0.00000e+00
    tnz:    0.00000e+00    0.00000e+00    0.00000e+00    0.00000e+00    0.00000e+00
```

Listing B.3: Example of the blade parameters for a tip rotor blade in the CACTUS geometry (.geom) file

The main script, CACTUS.f90, contains the iterative procedure that checks when the solution meets the convergence criteria. During this loop the position of the turbine is rotated by a delta defined by the number of time-steps per revolution, shown in Equation (B.1). With the inclusion of the tip rotor, additional rotations are necessary to model the rotation of the tip rotors these are defined using the $\Delta\theta$ of the primary rotor and the ratio between the rotational velocities of the primary and secondary rotors (see Equation (B.2)). The implementation of this in CACTUS uses the RPMs of the primary and secondary rotors and is shown in line 297 in Listing B.4.

$$\Delta\theta = \frac{2\pi}{N_t} \tag{B.1}$$

$$\Delta\theta_{tip} = \Delta\theta \frac{\omega_{tip}}{\omega} \tag{B.2}$$

```
293     ! Normalization parameters for geometry and performance outputs
294     romega=2.0*pi*Rmax*rpm/60.0
295     uinf=romega/ut
296     DT=DelT/ut                                    ! normalized simulation timestep (dt*Uinf/Rmax)
```

```
297     tipdelt=delt*rpmtip/rpm                    ! change in theta of secondary rotor.
```

Listing B.4: Definition of $\Delta\theta_{tip}$ in CACTUS.f90

Rotation of the turbine is handled by the *RotateTurbine* subroutine which is called in CACTUS.f90. Within the *RotateTurbine* subroutine CACTUS calls upon the *RotateBlade* subroutine.

```
21      ! Rototate tip rotors
22      if (tiprotorflag > 0) then
23          write(*,*) 'Tip rotor ON'
24          nbprimary=nb-ntip*nbtip
25          do k=1, nbprimary
26              do i=1, nbtip ! Loop through tip blades per primary rotor blade
27                  itt=nbprimary + i + (k - 1) * nbtip * nbprimary
28                  itb=nbprimary + i + nbtip + (k - 1) * nbtip * nbprimary
29                  i_top = k*nedge
30                  i_bot = nedge*(k-1) + 1
31                  ! Top tip rotor
32                  Call RotateBlade(itt,tipdelt,txBE(i_top),tyBE(i_top),tzBE(i_top),xBE(i_top),yBE(i_top),
    zBE(i_top))
33                  ! Bottom tip rotor
34                  Call RotateBlade(itb,tipdelt,txBE(i_bot),tyBE(i_bot),tzBE(i_bot),xBE(i_bot),yBE(i_bot),
    zBE(i_bot))
35
36              end do
37          end do
38      end if
```

Listing B.5: Implementation of the secondary rotor rotation in CACTUS

The blade element loads on the tip rotors are defined by the local inflow conditions. These inflow conditions are augmented by the rotation of the tip rotor, thus the tip rotor rotation must be accounted for when determining the local blade velocity. This is shown in Listing B.6 where the rotational component of the tip rotor velocity is determined using the tip-speed ratio of the tip rotor.

```
95      if (tiprotorflag > 0) then
96          nbprimary=nb-ntip*nbtip
97          tipidx0 = nbprimary*(nbe)
98          if (nElem>tipidx0+2) then
99              wRotX_tip = tsrtip * ut
100             wRotY_tip = tsrtip * ut * ttny
101             WRotZ_tip = tsrtip * ut * ttnz
102             CALL CalcBladeVel(wRotX_tip,wRotY_tip,wRotZ_tip,xe,ye,ze,uBlade_tip,vBlade_tip,wBlade_tip)
103             uBlade_tip = wRotY_tip*ttaz-wRotZ_tip*ttay
104             vBlade_tip = wRotZ_tip*ttax-wRotX_tip*ttaz
105             wBlade_tip = wRotX_tip*ttay-wRotY_tip*ttax
106             uBlade = uBlade + uBlade_tip
107             vBlade = vBlade + vBlade_tip
108             wBlade = wBlade + wBlade_tip
109         end if
110     end if
111
112     ! Calc element normal and tangential velocity components. Calc element pitch rate.
113     urdn = (nxe*(uAve+uFSAve-uBlade)+nye*(vAve+vFSAve-vBlade)+nze*(wAve+wFSAve-wBlade))      ! Normal
114     urdc = (txe*(uAve+uFSAve-uBlade)+tye*(vAve+vFSAve-vBlade)+tze*(wAve+wFSAve-wBlade))+wRotX_tip    !
     Tangential
115     wP = sxe*wRotX+sye*wRotY+sze*wRotZ
```

Listing B.6: The calculation of the local blade velocity for the tip rotors

The contribution of the tip rotors to the torque of the full turbine system is also handled by bsload.f90. The second if statement identifies only the tip rotor blade indices using the geometric format earlier where the primary rotor blades are defined before the tip rotor blades.

```
177     if (tiprotorflag > 0) then
178         if (nElem>tipidx0+2) then
179             te=-(ur**2/ut**2)*(ElemAreaR/nbtip)/(AreaT)*CN
180         end if
```

```
181     end if
```

Listing B.7: Torque coefficient contribution by tip rotor blade elements